AD-A140 233   SURFACE CHEMISTRY OF NIO (100)(U) AIR FORCE INST OF   1/2
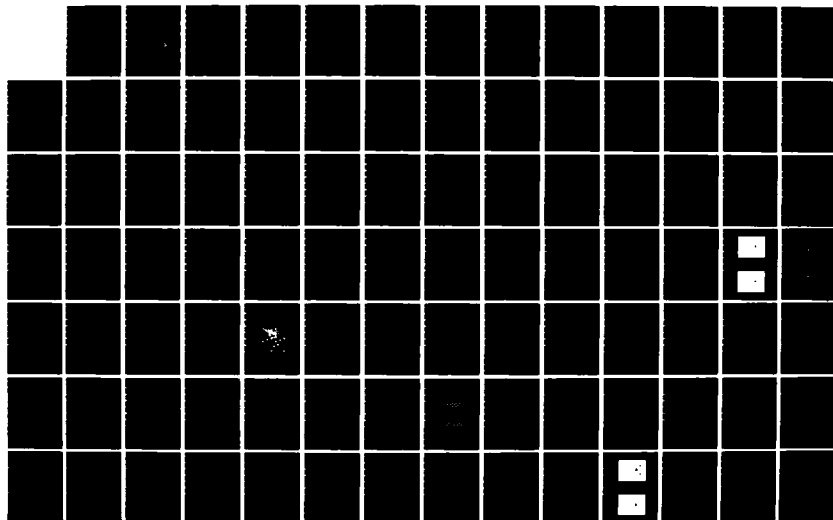   TECH WRIGHT-PATTERSON AFB OH   R P FURSTENAU 1984
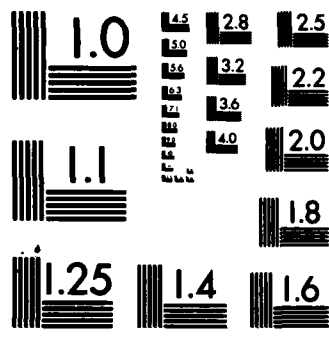   AFIT/CI/NR-84-2T
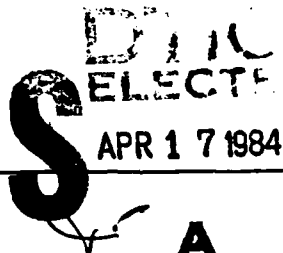
MICROCOPY RESOLUTION TEST CHART

NATIONAL BUREAU OF STANDARDS-1963-A

REPORT DOCUMENTATION PAGE	READ INSTRUCTIONS BEFORE COMPLETING FORM
1. REPORT NUMBER AFIT/CI/NR 84-2T	2. GOVT ACCESSION NO. *AD-A140233* 3. RECIPIENT'S CATALOG NUMBER
4. TITLE (and Subtitle) Surface Chemistry Of Nio (100)	5. TYPE OF REPORT & PERIOD COVERED THESIS/DISSERTATION
	6. PERFORMING ORG. REPORT NUMBER
7. AUTHOR(s) Ronald P. Furstenau	8. CONTRACT OR GRANT NUMBER(s)
9. PERFORMING ORGANIZATION NAME AND ADDRESS AFIT STUDENT AT: University of Nebraska	10. PROGRAM ELEMENT, PROJECT, TASK AREA & WORK UNIT NUMBERS
11. CONTROLLING OFFICE NAME AND ADDRESS AFIT/NR WPAFB OH 45433	12. REPORT DATE 1984
	13. NUMBER OF PAGES 127
14. MONITORING AGENCY NAME & ADDRESS(If different from Controlling Office)	15. SECURITY CLASS. (of this report) UNCLASS
	15a. DECLASSIFICATION/DOWNGRADING SCHEDULE

16. DISTRIBUTION STATEMENT (of this Report)

APPROVED FOR PUBLIC RELEASE; DISTRIBUTION UNLIMITED

17. DISTRIBUTION STATEMENT (of the abstract entered in Block 20, if different from Report)

18. SUPPLEMENTARY NOTES

APPROVED FOR PUBLIC RELEASE: IAW AFR 190-1

LYNN E. WOLAVER
Dean for Research and
Professional Development
AFIT, Wright-Patterson AFB OH

19. KEY WORDS (Continue on reverse side if necessary and identify by block number)

20. ABSTRACT (Continue on reverse side if necessary and identify by block number)

ATTACHED

DD FORM 1473 1 JAN 73 EDITION OF 1 NOV 65 IS OBSOLETE

SURFACE CHEMISTRY OF NiO (100)

by

Ronald P. Furstenau

A THESIS

Presented to the Faculty of

The Graduate College in the University of Nebraska

In Partial Fulfillment of Requirements

For the Degree of Master of Science

Major: Chemistry

Under the Supervision of Professor Marjorie A. Langell

Lincoln, Nebraska

January, 1984

ACKNOWLEDGEMENTS

TABLE OF CONTENTS

LIST OF FIGURES

FIGURES   page

FIGURES page

FIGURES

LIST OF TABLES

LIST OF ACRONYMS AND ABBREVIATIONS

Acronyms and abbreviations flourish with reckless abandon in surface chemistry. Encounters with them are unavoidable in the literature. The following is a partial list of acronyms and abbreviations frequently encountered in the literature and which the reader of this thesis will unfortunately encounter as well.

AES - Auger Electron Spectroscopy

AMU - Atomic Mass Units

CMA - Cylindrical Mirror Analyzer

ESCA - Electron Spectroscopy for Chemical Analysis

KeV - Kiloelectron Volts

L - Langmuir (1 X 10^{-6} Torr-sec)

LEED - Low Energy Electron Diffraction

ML - Monolayers

PHI - Physical Electronics Division of Perkin-Elmer Corporation

RHEED - Reflection High Energy Electron Diffraction

UHV - Ultra High Vacuum ($<10^{-9}$ Torr)

UPS - Ultraviolet Photoelectron Spectroscopy

XPS - X-ray Photoelectron Spectroscopy (same as ESCA)

FOLD DOWN ON OUTSIDE - SEAL WITH TAPE

AFIT/NR
WRIGHT-PATTERSON AFB OH 45433

OFFICIAL BUSINESS
PENALTY FOR PRIVATE USE. $300

BUSINESS REPLY MAIL
FIRST CLASS   PERMIT NO. 73236   WASHINGTON D.C.

POSTAGE WILL BE PAID BY ADDRESSEE

AFIT/ DAA
Wright-Patterson AFB OH 45433

NO POSTAGE
NECESSARY
IF MAILED
IN THE
UNITED STATES

FOLD IN

AFIT RESEARCH ASSESSMENT

The purpose of this questionnaire is to ascertain the value and/or contribution of research accomplished by students or faculty of the Air Force Institute of Technology (ATC). It would be greatly appreciated if you would complete the following questionnaire and return it to:

AFIT/NR
Wright-Patterson AFB OH 45433

RESEARCH TITLE: ___Surface Chemistry Of Nio (100)___

AUTHOR: ___Ronald P. Furstenau___

RESEARCH ASSESSMENT QUESTIONS:

1. Did this research contribute to a current Air Force project?

( ) a. YES   ( ) b. NO

2. Do you believe this research topic is significant enough that it would have been researched (or contracted) by your organization or another agency if AFIT had not?

( ) a. YES   ( ) b. NO

3. The benefits of AFIT research can often be expressed by the equivalent value that your agency achieved/received by virtue of AFIT performing the research. Can you estimate what this research would have cost if it had been accomplished under contract or if it had been done in-house in terms of manpower and/or dollars?

( ) a. MAN-YEARS _____   ( ) b. $_____

4. Often it is not possible to attach equivalent dollar values to research, although the results of the research may, in fact, be important. Whether or not you were able to establish an equivalent value for this research (3. above), what is your estimate of its significance?

( ) a. HIGHLY   ( ) b. SIGNIFICANT   ( ) c. SLIGHTLY   ( ) d. OF NO
       SIGNIFICANT   SIGNIFICANT   SIGNIFICANCE

5. AFIT welcomes any further comments you may have on the above questions, or any additional details concerning the current application, future potential, or other value of this research. Please use the bottom part of this questionnaire for your statement(s).

NAME	GRADE	POSITION
ORGANIZATION	LOCATION	

STATEMENT(s):

ABSTRACT

The hydrogen reduction process of NiO (100) was studied in detail using Auger Electron Spectroscopy (AES), X-ray Photoelectron Spectroscopy (XPS), and Low Energy Electron Diffraction (LEED). The data indicate that the reduction process is strongly temperature dependent. Although the surface lattice loses oxygen in the reduction process, the basic structure of the lattice remains the same. A model is proposed which describes the stoichiometric and reduced NiO (100) surface layers which gives good correlation with the observed data.

In addition, the adsorption properties of ethylene on stoich- iometric and reduced NiO (100) were also studied. The results show that the stoichiometric NiO (100) only adsorbs ethylene at low temperatures (200K) with low coverage (0.07 monolayers of carbon). The reduced NiO proved more reactive, with adsorption occurring between 200K and 500K. The data indicate that although the surface of the reduced sample is mostly nickel, it does not adopt the adsorption properties of pure nickel metal. At higher temperatures (500K), adsorption on the reduced sample reaches 0.28 monolayers of carbon while further reduction of the surface occurs, indicating the dissociation of the ethylene molecule. A model is also proposed which describes how the reduced NiO (100) surface accommodates the adsorption of ethylene molecules.

ABSTRACT

The hydrogen reduction process of NiO (100) was studied in detail using Auger Electron Spectroscopy (AES), X-ray Photoelectron Spectroscopy (XPS), and Low Energy Electron Diffraction (LEED). The data indicate that the reduction process is strongly temperature dependent. Although the surface lattice loses oxygen in the reduction process, the basic structure of the lattice remains the same. A model is proposed which describes the stoichiometric and reduced NiO (100) surface layers which gives good correlation with the observed data.

In addition, the adsorption properties of ethylene on stoichiometric and reduced NiO (100) were also studied. The results show that the stoichiometric NiO (100) only adsorbs ethylene at low temperatures (200K) with low coverage (0.07 monolayers of carbon). The reduced NiO proved more reactive, with adsorption occurring between 200K and 500K. The data indicate that although the surface of the reduced sample is mostly nickel, it does not adopt the adsorption properties of pure nickel metal. At higher temperatures (500K), adsorption on the reduced sample reaches 0.28 monolayers of carbon while further reduction of the surface occurs, indicating the dissociation of the ethylene.molecule. A model is also proposed which describes how the reduced NiO (100) surface accommodates the adsorption of ethylene molecules.

CONCLUSIONS

The surface chemistry of NiO (100) has been studied using AES, XPS, and LEED. The stoichiometric surface has been characterized and is bulk-terminated with a completely oxidized layer. A study of the reduction process of NiO (100) in H_2 indicates a strong temperature dependence on the rate of reduction due to oxygen migration through the lattice. The study also showed that the reduction process has an initial induction period, followed by a near-linear acceleration period of reduction with increased hydrogen exposure. As shown with AES and XPS during depth profiling, the reduction process occurs three-dimensionally into the crystal. As reduction progresses, LEED measurements indicate that the surface lattice structure remains basically the same as for the stoichiometric NiO (100). AES and XPS results indicate that the surface of the NiO (100) becomes more and more nickel-like as the reduction proceeds. The reduced surface consists of nickel atoms in the same arrangement as the stoichiometric surface, with random oxygen vacancies. The reduction process occurs through the dissociation of the hydrogen on nickel sites and subsequent combination with oxygen to form H_2O, which is desorbed.

The stoichiometric NiO appears unreactive toward ethylene, except at low temperatures. At low temperatures, a simple physisorption or non-dissociative chemisorption is occurring.

If a reduced NiO surface, where oxygen lattice vacancies are present, is used to study the adsorption of ethylene, different processes occur at different temperatures. At low temperatures

the reduced NiO behaves similarly to stoichiometric NiO except for
an additional condensed layer. At room temperature, however,
it is apparent that the presence of more nickel atoms relative to
oxygen atoms promotes the adsorption of ethylene at nickel sites,
although not as greatly as would be expected from the increasing Ni
character seen in AES and LEED. At 500K, further reduction of the
NiO is taking place with increasing ethylene exposure. In addition,
the coverage of carbon increases more rapidly with exposure due
to more Ni adsorption sites forming. The results at 500K indicate
that the ethylene is losing some of its hydrogens, with subsequent
products staying adsorbed. Dissociation of the C-C bond is also
likely, although it could not be proved unequivocally. Some of
the results of ethylene adsorption on reduced NiO are analogous
to those occurring on nickel metal. A model for the formation
of adsorption sites on the reduced NiO explains the ethylene
adsorption coverage seen experimentally for the reduced sample.

REFERENCES

1. P. Auger, J. Phys. Radium, 6 (1925) 205.

2. C.D. Wagner, W.M. Riggs, L.E. Davis, J.F. Moulder, and G.E. Muilenberg (ed.), "Handbook of X-ray Photoelectron Spectroscopy," Perkin-Elmer Corporation (1979).

3. A.W. Czanderna, ed., "Methods of Surface Analysis," Elsevier Scientific Publishing Co., Amsterdam (1975).

4. G. Ertl and J. Kuppers, "Low Energy Electrons and Surface Chemistry," Verlag Chemie, Weinheim, Germany (1974).

5. L.E. Davis, N.C. MacDonald, P.W. Palmberg, G.E. Riach, and R.E. Weber, "Handbook of Auger Electron Spectroscopy," 2nd ed., Physical Electronics Industries, Inc. (1976).

6. S.R. Morrison, "The Chemical Physics of Surfaces," Plenum Press, New York (1977).

7. C.C. Chang, Surface Sci., 25 (1971) 53.

8. Perkin-Elmer Corporation--Physical Electronics Division Users' Manuals for ultra high vacuum system components. Various publishing dates.

9. A. Joshi, L.E. Davis, and P.W. Palmberg, Auger Electron Spectroscopy in: "Methods of Surface Analysis," Elsevier Scientific Publishing Co., Amsterdam (1975).

10. S. Mroczkowski and D. Luhtman, Surface Sci., 131 (1983) 159.

11. W.M. Riggs and M.J. Parker, Surface Analysis by X-ray Photo-electron Spectroscopy in: "Methods of Surface Analysis," Elsevier Scientific Publishing Co., Amsterdam (1975).

12. W.F. Stickle and R.G. Hayes, J. Chem. Phys., 79, 9 (1983) 4106.

13. K.S. Kim, J. Electron. Spectrosc. Relat. Phenom., 3 (1974) 217.

14. L.J. Matienzo, L.O. Yin, S.O. Grim, and W.E. Swartz, Inorg. Chem., 12 (1973) 2764.

15. K.S. Kim and R.E. Davis, J. Electron. Spectrosc. Relat. Phenom., 1 (1972/73) 251.

16. A. Rosencwaig, G.K. Wertheim, and H.J. Guggenheim, Phys. Rev. Lett., 27 (1971) 479.

17. Personal conversation with Professor M.A. Langell (8 Nov 83).

18. D.C. Frost, A. Ishitani, and C.A. McDowell, Mol. Phys., 24 (1972) 861.

19. L.H. Germer and A.U. MacRae, J. Appl. Phys., 33, 10 (1962) 2923.

20. L.H. Germer and C.D. Hartman, J. Appl. Phys., 31 (1960) 2085.

21. J.W. May and L.H. Germer, Hydrogen and Oxygen on a (110) Nickel Surface in: "The Structure and Chemistry of Surfaces," ed. G.A. Somorjai, John Wiley and Sons, Inc., New York (1969).

22. M.R. Welton-Cook and M. Prutton, J. Phys. C., 13, 20 (1980) 3993.

23. J.B. Pendry, "Low Energy Electron Diffraction," Academic Press, London (1974).

24. M.A. Van Hove and S.Y. Tong, "Surface Crystallography by LEED," Springer-Verlag, Heidelberg (1979).

25. G.V. Samsonov, ed., "The Oxide Handbook," IFI/Plenum, New York (1973).

26. Personal conversation with Professor M.A. Langell (9 Jan 84).

27. The nickel oxide disk was kindly supplied by Norman Peterson, Materials Science Division, Argonne National Laboratory.

28. N. Floquet and L.-C. Dufour, Surface Sci., 126 (1983) 543.

29. J.M. Rickard, M. Perdereau, and L.C. Dufour, J. Microsc. Spectrosc. Electron., 4 (1979) 95.

30. N. Floquet, P. Dufour, and L.-C. Dufour, J. Microsc. Spectrosc. Electron., 6 (1981) 473.

31. Y.K. Rao, Met. Trans. B., 10B (1979) 243.

32. K.S. Kim and N. Winograd, Surface Sci., 43 (1974) 625.

33. M.W. Roberts and R. St.C. Smart, Surface Sci., 100 (1980) 590.

34. J.A. Little, J.W. Evans, and K.H. Westmacott, Met. Trans. B., 11B (1980) 225.

35. G. Wedler and M. Brenk, Z. Phys. Chem. (Wiesbaden), 119 (1980) 225.

36. W. Krasser, A. Fadini, E. Rozenmuller and A.J. Renouprez, J. Mol. Struct., 66 (1980) 135.

37. J.E. Demuth and D.E. Eastman, Phys. Rev. Lett., 32 (1974) 1123.

INTRODUCTION

The large arena of surface chemistry has many applications. The understanding of catalysis, corrosion, and semiconductor properties all rely on understanding the chemical reactions taking place on a gas/solid or liquid/solid interface; that is, a surface. Relatively few studies have been presented documenting the surface properties on nickel oxide. Therefore, the purpose of this thesis work was to study the surface chemistry of NiO. More, specifically, this work focused on studying the reduction process of NiO and studying the adsorption of ethylene on stoichiometric NiO and reduced NiO.

The reduction of NiO and adsorption of gases (specifically, ethylene) on NiO can be studied with a variety of in situ techniques. Auger electron spectroscopy (AES), x-ray photoelectron spectroscopy (XPS), and low energy electron diffraction (LEED) were the techniques used in this study. All three of these techniques require high or ultra-high vacuum conditions. The combination of these techniques allows one to monitor atomic concentrations of elements on the surface, changes in the chemical environment of these elements, and structural changes on the surface of the NiO crystal.

The remainder of this thesis consists of four main sections. The first section discusses the theoretical aspects of AES, XPS, and LEED. The next section supplies a complete description of the experimental aspects of the study, including procedures. The third section discusses the results of the study of the reduction process of NiO (100) and the adsorption of ethylene on NiO (100). The final

section compares the data from this study with data available from the literature.

THEORY

This section presents a brief discussion of the processes behind Auger Electron Spectroscopy (AES), X-ray Photoelectron Spectroscopy (XPS or ESCA), and Low Energy Electron Diffraction (LEED). Each subsection refers to numerous books and articles where a more detailed discussion of the theory can be found. Also included is a description of the experimental method required for AES, XPS, and LEED. Finally, a brief description of how to interpret the data resulting from each technique is included.

AUGER ELECTRON SPECTROSCOPY (AES)

The Auger Process. P. Auger discovered the Auger effect in 1925 while studying processes of x-ray absorption (1). The Auger process can occur when an electron of sufficient energy ionizes a core electron. As shown in Figure 1, this core level vacancy (K) is immediately filled by another electron $(L_{2,3})$. The energy from the $L_{2,3}$ to K transition can be transferred to another electron $(L_{2,3})$. This electron is then ejected from the atom as an Auger electron. The measured energy of this electron is as follows (3):

$$KE = E_K(Z) - E_{L_{2,3}}(Z) - E_{L_{2,3}}(Z + d) - \phi_A \quad ,$$

where Z = atomic number of the atom involved

ϕ_A = work function of the analyzer material

d = energy correction term for the final doubly ionized state $(\frac{1}{2} < d < 3/4)$.

The Auger electron energies cause only small changes in the total electron energy distribution function $N(E)$ and thus small

4
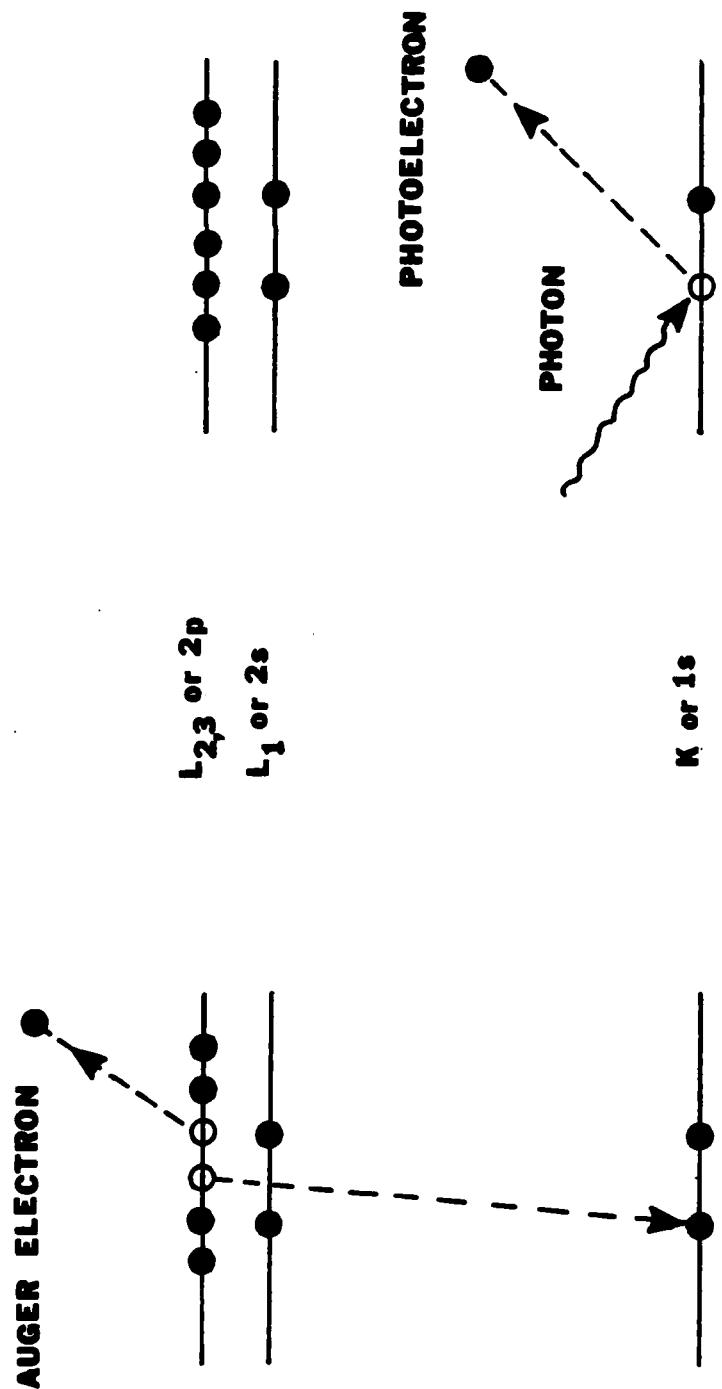
FIGURE 1. Schematic of the Auger process and photoelectric process. From reference 2.

peaks in N(E) versus electron kinetic energy. However, the Auger
peaks are very evident when the N(E) function is electronically
differentiated. Figure 2 illustrates the difference between N(E)
and dN(E)/dE Auger spectra and shows the advantage gained in
differentiation (4). Nearly all analytical Auger data presented in
the literature are in the differentiated form. The energy positions
of the resultant peaks are indicative of the elements present on the
sample surface. In addition, AES is sensitive enough that
0.005 monolayers (ML) of carbon on a surface can be detected.

References 3, 4, 5, and 6 have good, general discussions
regarding the Auger process and Auger theory. One of the first
overview articles to appear in the literature on AES was written
by Chang in 1971 (7).

Experimental Method. An AES system has two essential components:
an electron source and an electron energy analyzer. These two
components, plus the supporting electronics, as shown in Figure 3.
On the present apparatus, the source of electrons to initiate the
Auger process is located within the Auger/ESCA analyzer. Often,
however, the electron source is mounted outside of the analyzer.
The electron gun provides a directed beam of electrons normal to the
sample at energies up to 5 KV. Normally, the beam energy used in
these experiments was 2 KV.

On the present system, the same electron energy analyzer is
used for Auger and ESCA studies, but operated in different modes.
To provide a meaningful comparison between the modes of operation,
both modes will be discussed at this time. The reader may wish to

FIGURE 2. Energy distribution N(E) and dN/dE for a silver target. From ref. 4.
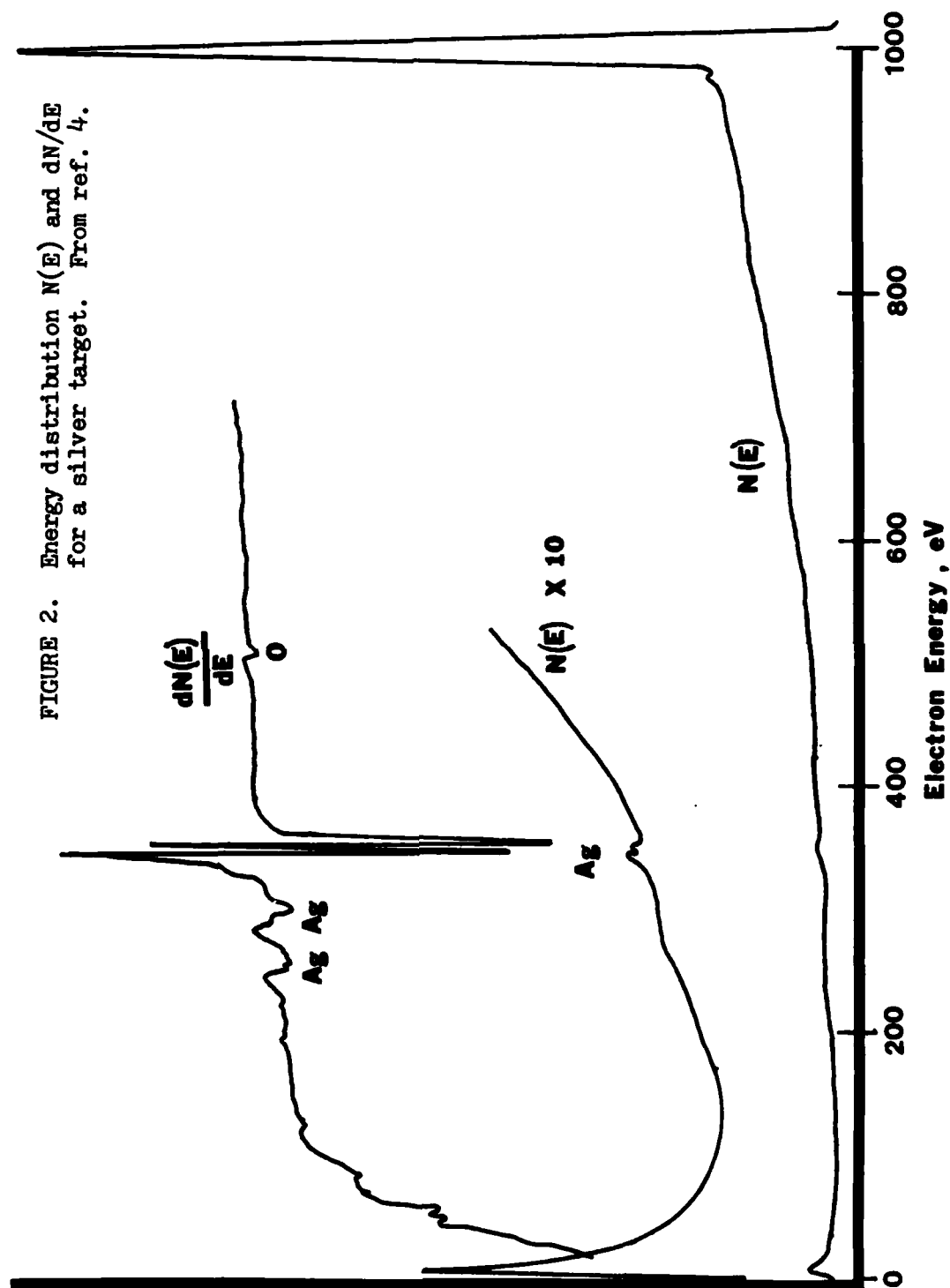
AUGER / ESCA SCHEMATIC
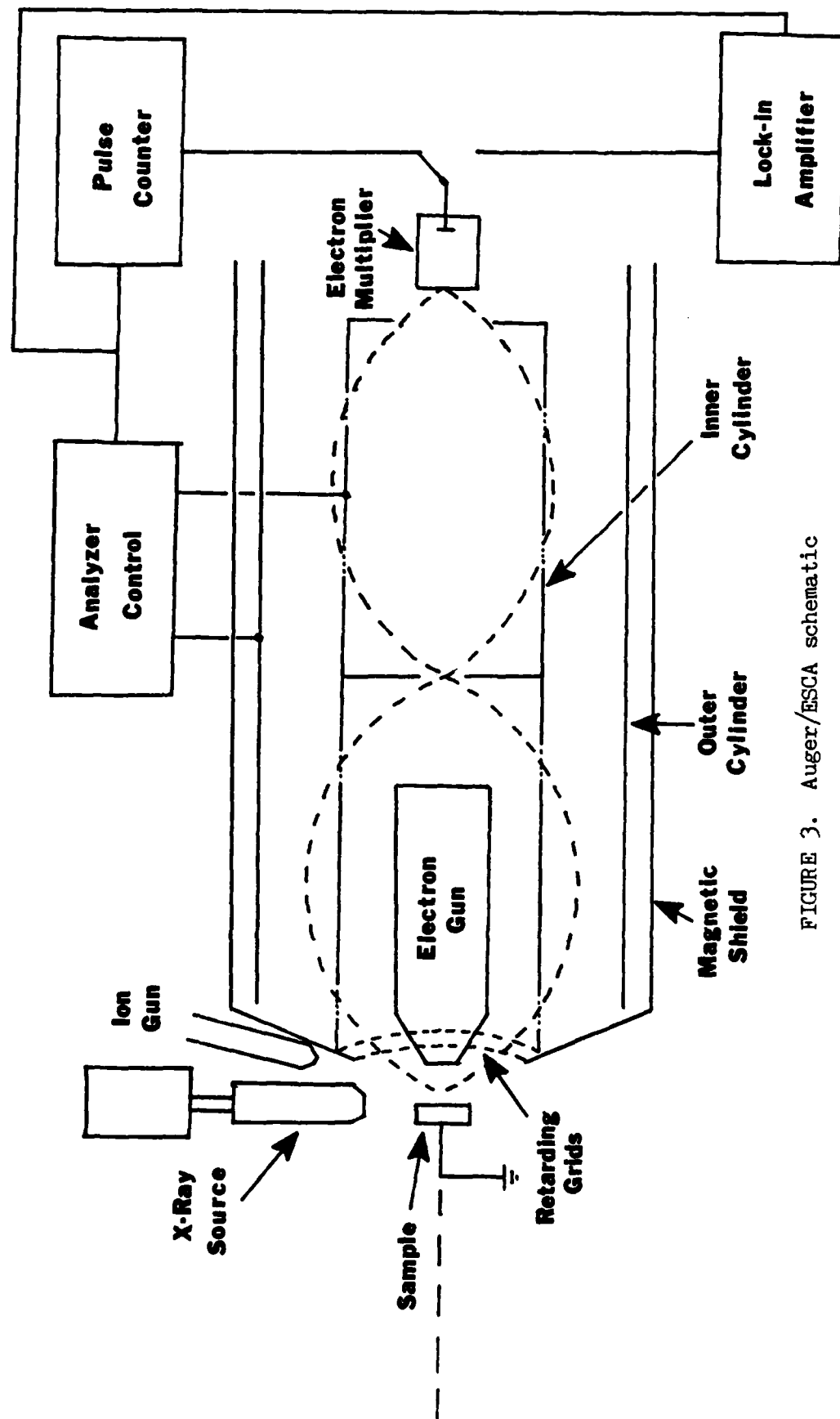
FIGURE 3. Auger/ESCA schematic

refer to this section when reading the section on XPS theory.
The analyzer is a double-pass cylindrical mirror analyzer (CMA),
which is equipped with three energy filters: one hemispherical
retarding grid system and two cylindrical mirror analyzers, all
arranged in series. In the Auger mode of operation, the retarding
grid is not used. Thus, the electrons enter the double-pass CMA with
their initial kinetic energy. As shown in Figure 3 by the dashed
arches, incoming Auger electrons of a given energy are focused onto
openings in the side of the inner cylinder by negative voltages
applied to the outer cylinder. This process is repeated in a
double-pass CMA, and the electrons are focused before entering an
electron multiplier. The deflection of the incoming electrons
depends on their kinetic energy and the repulsing voltage applied
to the outer cylinder. Thus, the kinetic energy of the electrons
passing through the analyzer can be controlled by the voltage
applied to the outer cylinder. The pass energy of the analyzer
(or, the energy range of the electrons accepted by the analyzer),
then, is proportional to the voltage V applied to the outer
cylinder by the following relationship:

$$E_{pass} = 1.70 \times V$$

where E_{pass} is in eV and V is in volts. To obtain the derivative of
the energy distribution, a small AC component is added to V on the
outer cylinder. The resulting electron current passing through the
final exit aperture enters a spiraltron (electron multiplier) and
is high enough (10^{-10} amps) to be amplified to a level that can be

detected by a lock-in amplifier. The lock-in amplifier is a phase-sensitive detector which mixes the signal voltage with a reference voltage, producing sum and difference frequencies. A filter discards the sum frequencies and passes the difference frequencies. Difference frequencies which result from the signal and which differ from the reference by a certain amount are then attenuated, resulting in the output spectrum (8).

In the nonretarding (Auger) mode of operation, the energy resolution is normally expressed as $\Delta E/E$, where ΔE is the absolute energy resolution and E is the kinetic energy of the electrons being emitted from the sample. For the present system, $\Delta E/E$ is 0.6% for the small internal aperture used for AES and is constant for the CMA (8).

When in the XPS mode, however, the absolute energy resolution of the double-pass CMA is not sufficient. Therefore, the spherical retarding grids, shown in Figure 3, are used to improve the resolution. In the retarding mode, the kinetic energy of the incoming electrons is reduced by the retarding grid and then measured by the CMA. Since $\Delta E/E$ of the CMA is constant, the absolute energy resolution ΔE can be improved by reducing the electron energy with the retarding grids. For example, if 2 KeV electrons are reduced to 100 eV using the retarding grids, the absolute energy resolution is improved from 12 eV to 1.2 eV (8).

The signal levels are usually very low in the high-resolution retarding analyzer mode because x-ray yields are lower than those for Auger electron guns. Therefore, the signal is detected in a

photon (pulse) counting mode for XPS rather than the analog lock-in detection used in AES. The photon counting mode uses a low noise pulse amplifier to amplify each individual electron pulse so it can be counted by electronic means. The amplitude of this electron pulse signal is then displayed in relation to the kinetic energy of the incoming electrons (in terms of their binding energy) as the XPS spectrum.

The model numbers and descriptions of all of the components of the Auger system used for this work appear in the DESCRIPTION OF APPARATUS section of this thesis. Czanderna (3), Ertl and Kuppers (4), Morrison (6), and Chang (7) all give excellent discussions of the variety of instrumentation used in AES, as well as extensive bibliographies on the subject.

Analysis of data. Once a differentiated Auger spectrum is obtained, the peaks present and their positions can be compared with reference spectra to identify the elements present on the surface. Figure 4 shows a typical AES for the clean NiO (100) surface. Note that the peaks associated with nickel and oxygen are quite distinguishable.

For semi-quantitative analysis, the peak heights on the spectrum can be related to elemental concentration, assuming that the peak shape does not change with changing concentration. The method of Davis et.al. (5,9) was used to calculate the atomic concentrations of the elements on the surface. This method employs the peak heights from the spectrum, relative sensitivities of the elements to the Auger process, and scale factors based on the conditions of the apparatus to determine relative concentrations of the elements on

12
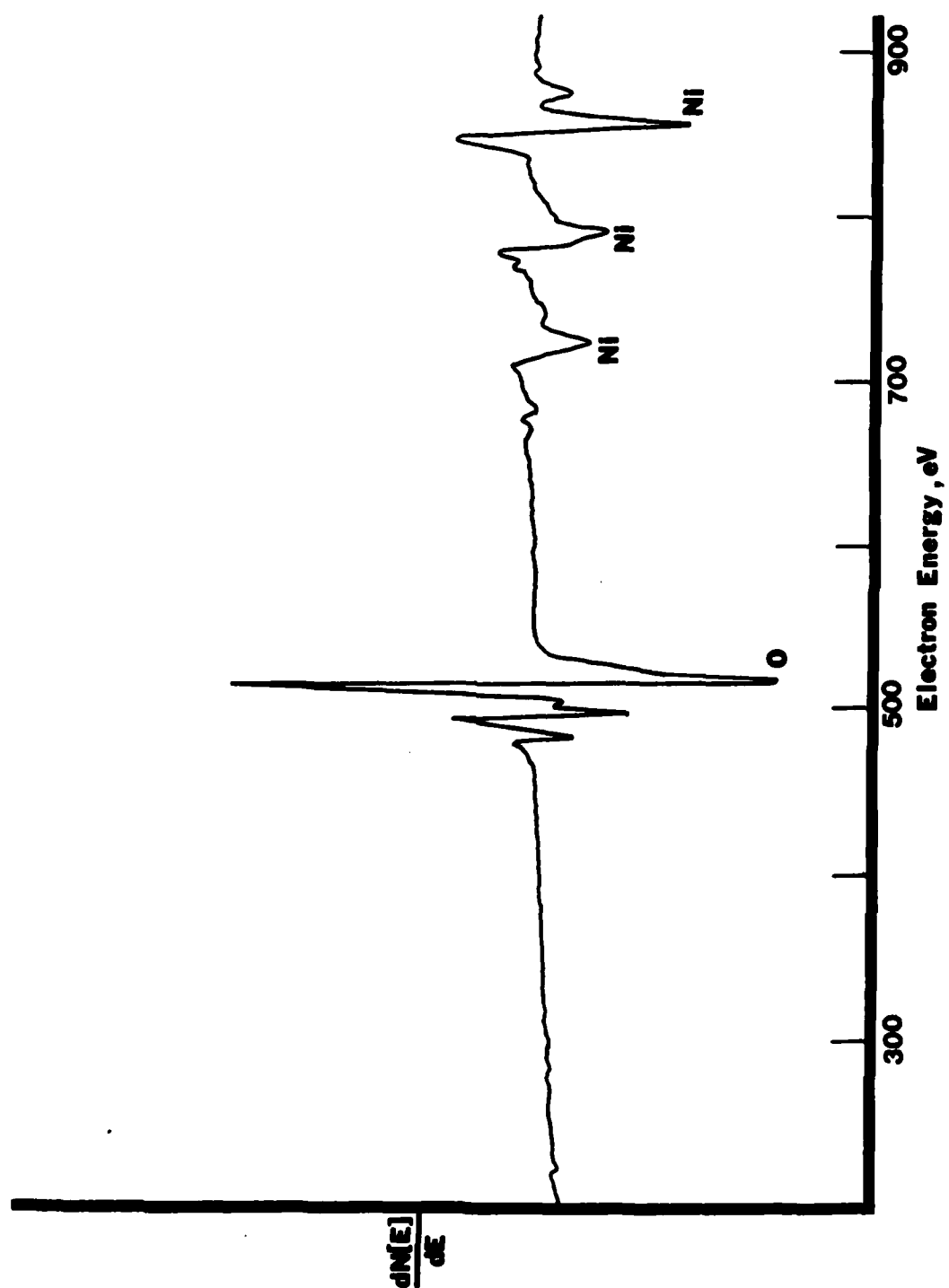
FIGURE 4. Auger spectrum for NiO (100)

the surface. Recently, Mroczkowski and Luhtman (10) performed
"first principle" calculations for Auger sensitivities which compare
quite well with experimentally obtained sensitivities where pure
elemental standards are available.

There are inherently several errors in this semi-quantitative
method. First, the Auger electron escape depth is dependent on the
electronic structure of the material, which may alter the depth
of the measurement relative to the standard. Secondly, chemical effects
can change Auger peak shapes, which can lead to error when using
peak-to-peak heights in differentiated spectra. The surface
topography, or roughness, will also affect the Auger signal.
Finally, there is also error due to electron backscattering factors (5).
The error due to the electronic structure of the NiO relative to
elemental standards is minimized since the same substrate was used
in all of the experiments and the error associated with escape
depths is the same relative to all of the measurements. Therefore,
when changes in relative concentrations are examined, this error
effectively cancels out. The effect of surface roughness is also
minimized, since all of the Auger peaks will be affected nearly
the same on the same sample. However, chemical effects cannot
be eliminated, since the chemical environment of the elements on
the surface can be expected to change as the sample is reduced or
as gases are adsorbed. Even so, since relative changes in elemental
concentrations were of primary interest in this study, this
calculational technique was deemed adequate.

Using the method of Davis et.al., atomic concentrations are expressed in the following manner:

$$C_x = \frac{I_x}{S_x d_x} \bigg/ \sum_a \frac{I_a}{S_a d_a}$$

where I_x = peak-to-peak amplitude of element x from the test specimen

S_x = relative sensitivity between any element x and silver $(S_{Ag} = 1.0)$

d_x = scale factor for any amplification

a = each element present, including x.

I_x is obtained directly from the Auger spectrum as peak-to-peak intensities in arbitrary units. S_x was obtained from charts of relative Auger sensitivities formulated from Auger spectra of standard compounds whose concentrations are well known. S_x is dependent on the primary electron beam voltage, E_p. All data presented in this thesis was taken at E_p = 2 KeV. Since S_x data was only available at 3, 5, and 10 KeV (also from reference 5), a linear regression analysis on this data was performed to yield S_x values at 2 KeV. Figure 5 illustrates the linearity of the data and justifies the use of a linear regression analysis to obtain S_x values at 2 KeV.

The scale factor d_x is defined by the following:

$$d_x = L_x E_{m,x} I_{p,x}$$

where L_x = the lock-in amplifier sensitivity

$E_{m,x}$ = the modulation energy

$I_{p,x}$ = the primary beam current.
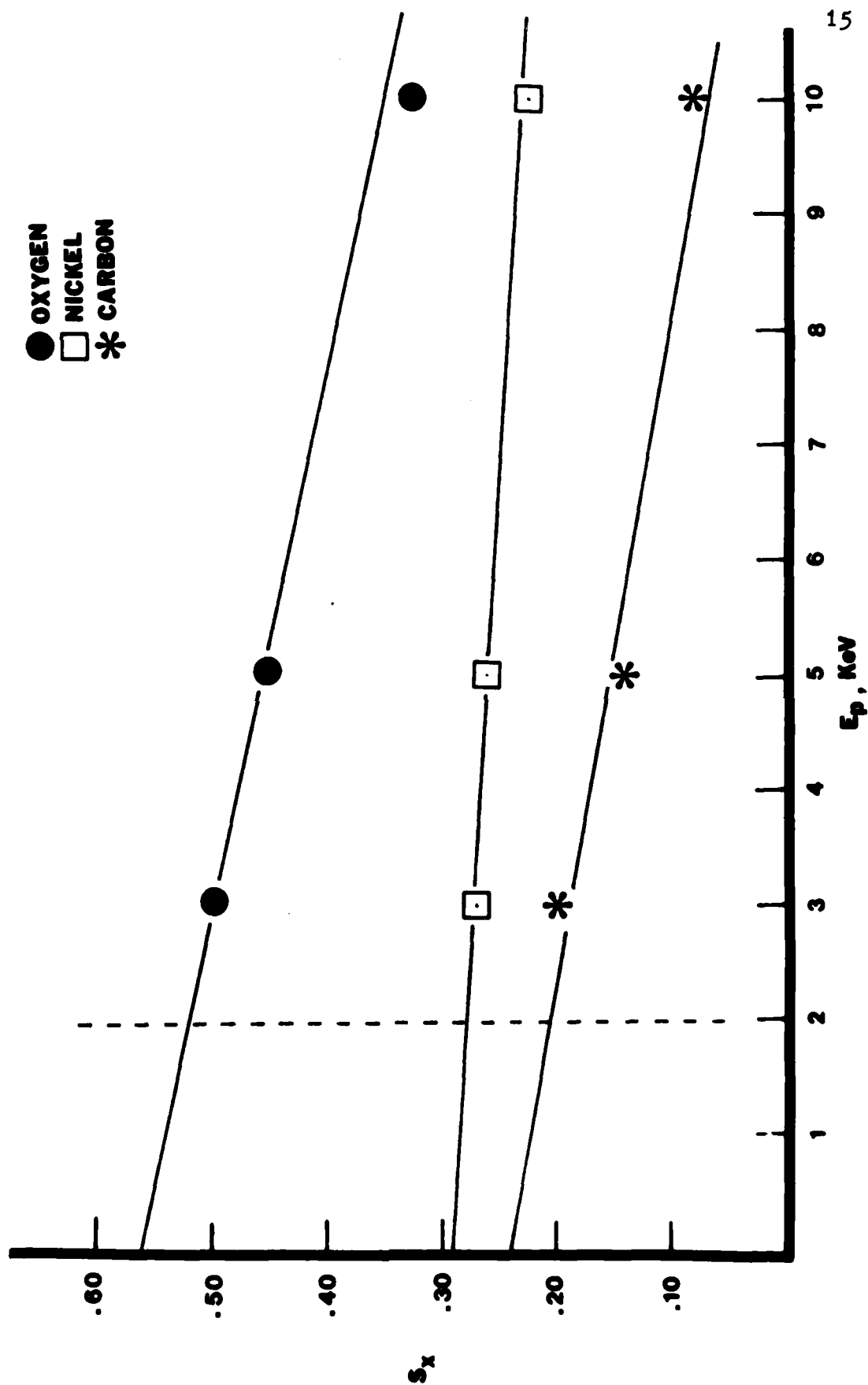
FIGURE 5. Determination of S_x for Ni, O, and C at $E_p = 2$ KeV

OXYGEN
NICKEL
CARBON

E_p, KeV

S_x

15

In these experiments, $E_{m,x}$ and $I_{p,x}$ are constant within each spectrum (and nearly equal between spectra, but this is not important for the calculation), so d_x only becomes a factor of L_x. L_x is precisely controlled and known by the equipment operator. Thus, this semi-quantitative method links the important instrumental variables with the Auger output signal and Auger sensitivity of the elements to determine elemental concentrations.

The Auger electrons can originate not only from the top layer of atoms, but from several subsequent layers into the sample as well. The probability of an Auger electron of a given energy originating a given number of layers into the sample is related to the electron's mean free path in the sample. A simple model which relates the observed Auger intensity to layers in which the electrons originated is as follows:

$$KI_0 = S_x \sum_n C_n \exp(-na/\lambda),$$

where   K = a constant dependent on equipment parameters

I_0 = the observed Auger peak intensity

S_x = relative Auger sensitivity of element x
(same as the S_x defined earlier)

n = 0,1,2,3 . . . n layers

C_n = concentration of element x at layer n

a = unit cell dimension into the crystal

λ = mean free path of the Auger electron at the particular Auger energy associated with the observed peak.

From the above equation, structures for the layering of atoms on the

surface can be proposed by relating the concentration of atoms expected at various layers to the intensity of the observed Auger signal.

X-RAY PHOTOELECTRON SPECTROSCOPY (XPS)

The basis for XPS (or Electron Spectroscopy for Chemical Analysis, ESCA) is the photoelectric process, illustrated in Figure 1. Incoming photons from the x-ray source are absorbed by the sample, resulting in the loss of an electron (photoelectron). By measuring the kinetic energy of the photoelectron, one can obtain the binding energy of the electron in its atomic orbital by the following equation:

$$BE = hv - KE - \phi_A$$

where BE = the binding energy of the electron

hv = the energy of the x-ray photons

KE = the kinetic energy of the photoelectrons

ϕ_A = the work function of the spectrometer analyzer.

One can see from Figure 1 that the Auger process can accompany the photoelectric process, since a hole is created in the photoelectric process. Indeed, Auger peaks are observed in an XPS spectrum and are identified in Figure 6 as an example.

The typical sampling depths are in the range of 5-25 $\mathring{A}$ for metals and metal oxides and 40-100 $\mathring{A}$ for organic and polymeric materials (11). Although XPS is somewhat less surface sensitive than AES, its greatest advantage lies in its ability to give information about the chemical environment of the elements on the surface. As with AES, the energy positions of the peaks are characteristic of each element in the periodic table, but on their own are not as reliable as AES. However, the peak shapes and
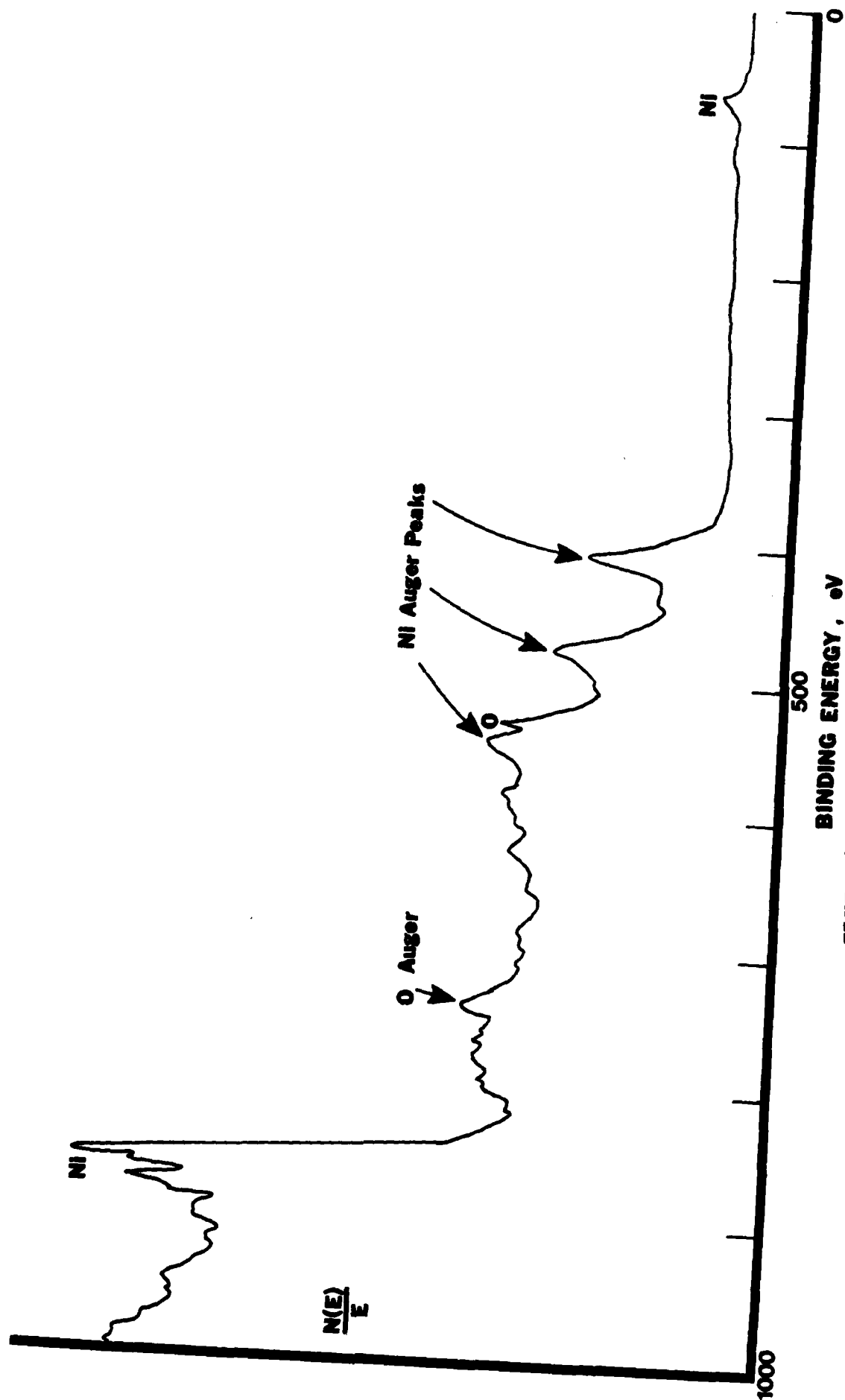
FIGURE 6. XPS spectrum for NiO (100), Mg anode

19

chemical shift information from XPS also provide valuable information about how the elements are affected by the presence of other elements. In addition, XPS does not bombard the surface with electrons as does AES, which can sometimes cause electron stimulated desorption of surface species. The x-ray beam is less destructive and thus provides a relatively non-destructive technique for surface analysis.

The discussion of XPS by Riggs and Parker (11) is a very good review. References 2 and 4 also have good XPS discussions. All three of these references provide excellent bibliographies for specific areas of interest in XPS.

Experimental Method. Like the AES system, the XPS or ESCA system has two essential components: an ionizing source and an electron energy analyzer. Instead of an electron gun, as is used to initiate the Auger process, the XPS system employs an x-ray source to generate photons which strike the sample surface to initiate the photoelectric effect. In the system used for these experiments, the user has a choice of an aluminum or magnesium anode as the x-ray photon source (Al Kα x-rays = 1486.6 eV, Mg Kα x-rays = 1253.6 eV). Figure 3 shows the position of the x-ray source relative to the sample and analyzer. In this case, the double-pass CMA which is used for AES (Figure 3) is also used for XPS. The electron energy analyzer determines the kinetic energy of the emitted photoelectrons which leads to the determination of binding energy. The pulse count mode (discussed in the AES section) for XPS uses the retarding filter (band pass). The output, displayed on an x-y recorder, is a spectrum of the energy distribution function (non-differentiated) versus binding energy.

Figure 7 shows a simplified schematic of the XPS system used in this study. Specific model numbers and descriptions of the components used appear in the DESCRIPTION OF APPARATUS section of this thesis. A good, general discussion of XPS system components appears in reference 11.

Analysis of data. Figure 6 is a broad-scan (1000 to 0 ev binding energy) XPS spectrum of NiO (100). The instrumentation settings for all of the spectra in the figures are listed in the EXPERIMENTAL section. As with AES, the location of the major peaks can be use to identify elements by comparing the spectrum with reference spectra (5). It is much more useful, however, to make detailed scans of narrow regions of the spectrum. Figures 8 and 9 show detailed scans for the O 1s and Ni 2p spectral regions. The detailed scans can lead to molecular structure information from chemical shifts ranging up to 5 eV, with the ability to distinguish ±0.15 eV differences.

Chemical shifts, or variations in the binding energies of elements, can yield important information on chemical states. The use of chemical shift information requires the experimenter to use a narrow scan range and that an accurate correction for surface charging can be made, since chemical shifts are often only a few tenths of an electron volt (see EXPERIMENTAL section). The chemical shifts result from changes in the chemical structure and oxidation state of chemical compounds. For example, a carbon compound containing several types of oxygen bonds will exhibit chemical shifts in the O 1s and C 1s regions, resulting in multiple peaks. Carbon in the
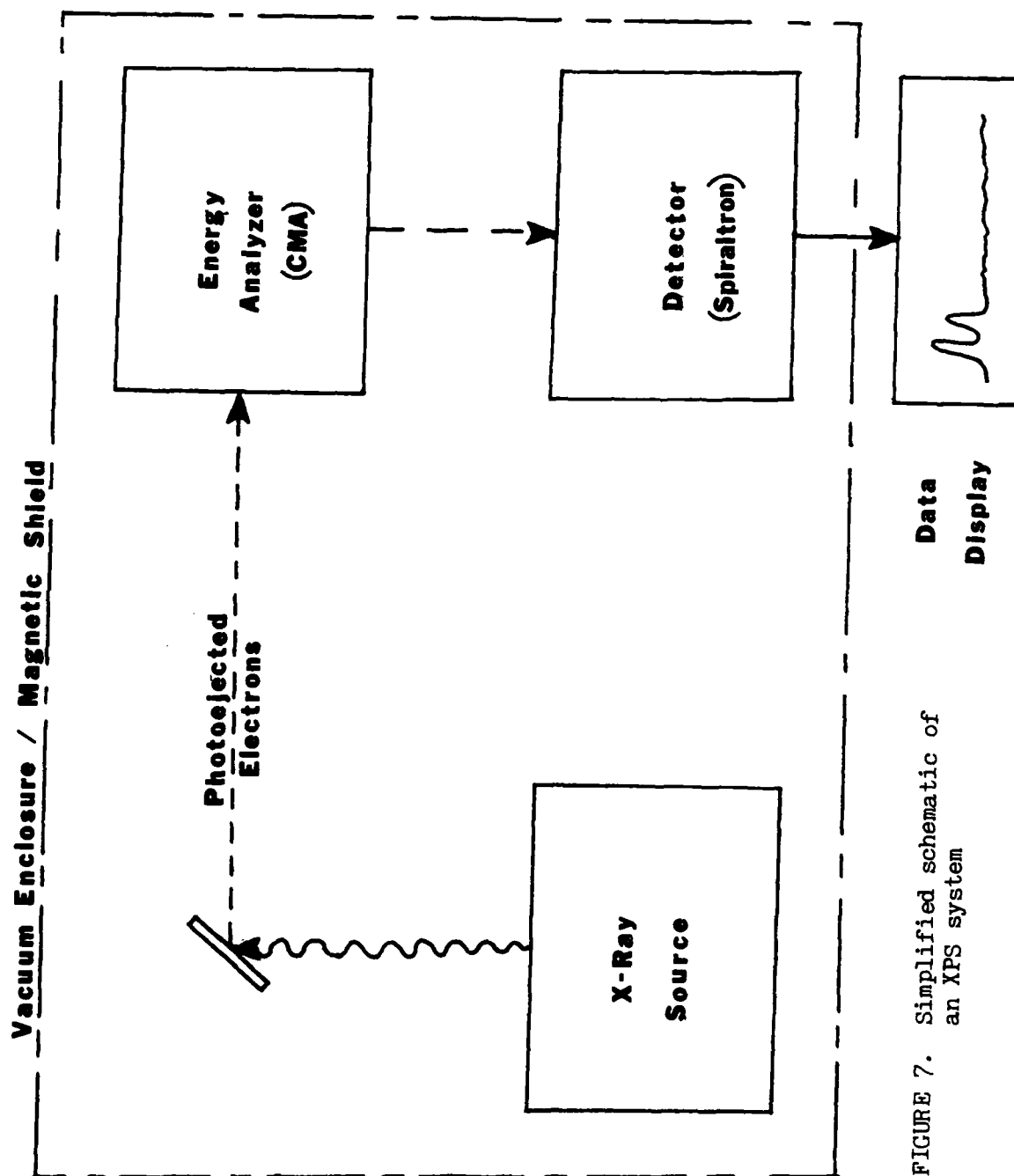
FIGURE 7. Simplified schematic of an XPS system

FIGURE 8. O 1s spectral region for stoichiometric NiO (100), Mg anode

"Shake-up" satellites
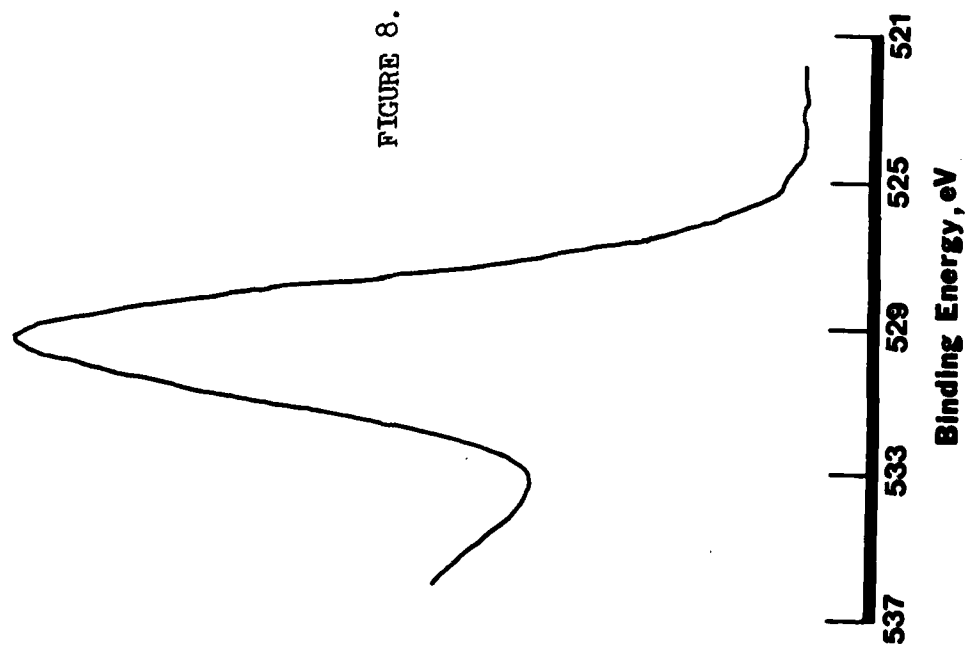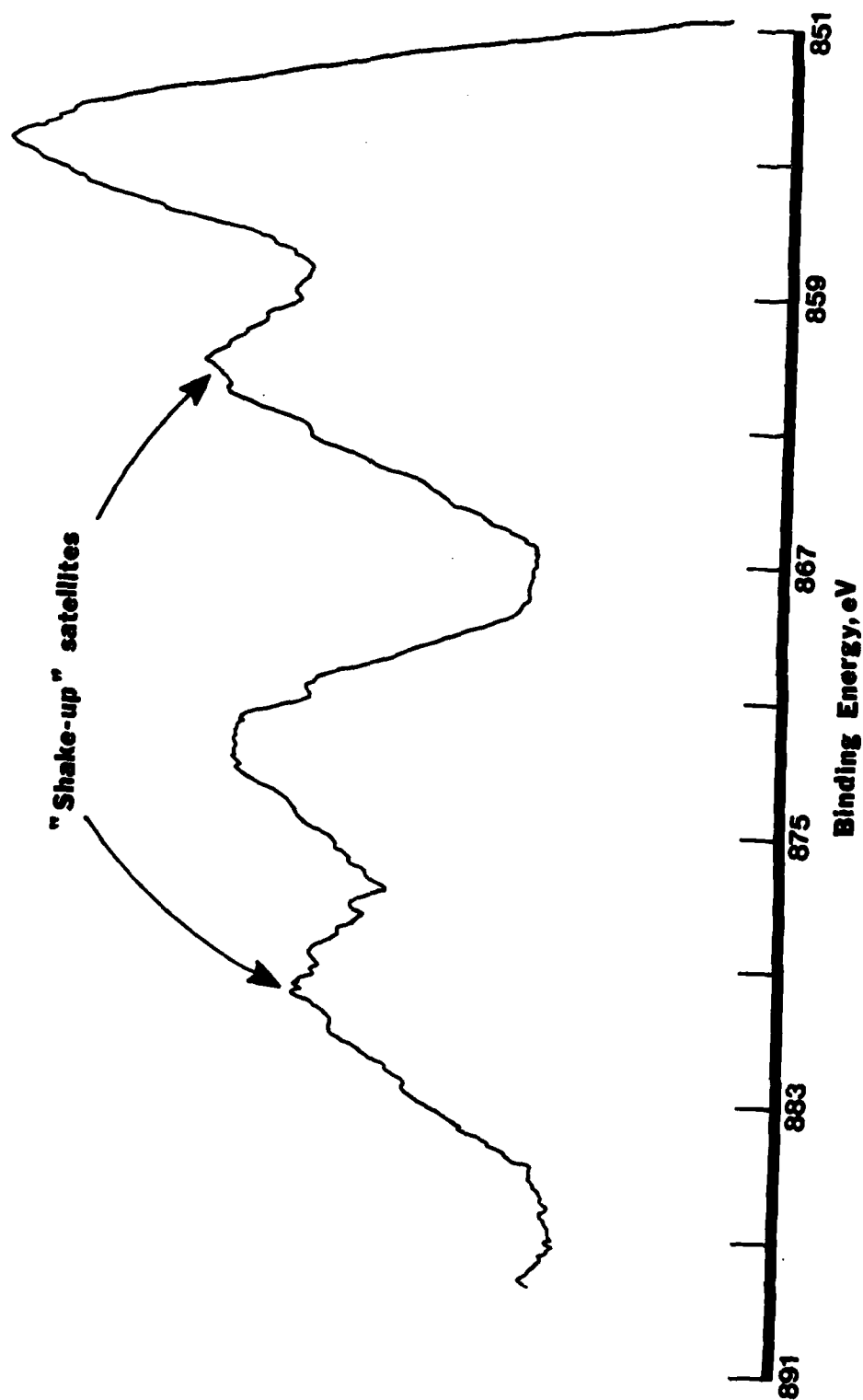
Binding Energy, eV

FIGURE 9. Ni 2p spectral region for stoichiometric NiO (100), Mg anode

most electronegative environment will appear at the highest binding
energy. The reason for this is because the electronegative oxygen
atoms withdraw electron density from the valence and bonding orbitals
of the carbon atom, reducing the screening of the core electrons
and increasing their binding energy (11).

For nickel oxide, the presence of two different oxygen-containing
nickel structures, such as Ni-O and Ni-OH, will lead to shifts in the
binding energy position of the O 1s peak. Reference 2, for example,
has compiled chemical shift information on the Ni $2p_{3/2}$ binding energies
from fundamental research in the literature. Values for the Ni $2p_{3/2}$
peak in Ni-O compounds range from 853.3 eV for NiO up to 856.9
reported for Ni_2O_3. Thus, chemical shift data can yield much
information regarding what type of compounds are present on a surface.
In addition to chemical shift information, a different effect can
be seen in the Ni 2p region known as satellite lines.

In Figure 9, one can see what are called "shake-up" satellite
peaks immediately to the left of each Ni 2p peak. The experimental
and theoretical aspects of these satellite peaks, specifically for
NiO, are described in several references (12-16). Basically, the
"shake-up" satellites can occur when the primary photoelectron, upon
leaving the atom, transfers some of its energy to a valence electron
which excites the valence electron to an unfilled higher energy level.
The photoelectron now has a lower kinetic energy and appears at a
higher binding energy in the spectrum. The "shake-up" satellite
peaks appear significantly in paramagnetic compounds and not in
diamagnetic compounds (11, 14, 17, 18).

The selection rules for shake-up transitions are $\Delta J = \Delta L = \Delta S = 0$, where J, L, and S represent the total, orbital, and spin angular momenta of the ion. In solids, there is a strong interaction among valence electrons. Since the shake-up transitions depend on the wave function overlap of the valence orbitals for solids, these orbitals must have the same symmetry. Therefore, one expects the additional selection rules of $\Delta L_v = 0$ and $\Delta S_v = 0$ in Russell-Saunders coupling, where L_v and S_v are the combined orbital and spin momenta, respectively, of the valence configuration involved in the shake-up transition. Applying these selection rules to transition metal ions with the initial state $(2p)^5(3d)^n$ and final state $(2p)^5(3d)^{n-1}4s$, it is found that shake-up transitions of the $3d-4s$ type can occur for either n odd or n even but L_v not zero. Because paramagnetic ions belong to this class, shake-up transitions of the $3d-4s$ type are possible for them. However, in diamagnetic ions all electrons are paired to give an initial state of $L_v = 0$. The final state would always have the analogous $(3d)(4s)$ configuration for diamagnetic ions, which cannot couple to give a final state $L_v = 0$. Therefore, $\Delta L_v \neq 0$ for diamagnetic ions and shake-up transitions are forbidden by the selection rules (14).

Thus, as the paramagnetic NiO compound is reduced to Ni, the satellite peaks decrease in intensity. Figure 11 illustrates the disappearance of the satellite peaks for a reduced NiO sample. Notice also that the O 1s peak in Figure 10 is severely diminished.

FIGURE 10. O1s spectral region for reduced NiO, Mg anode
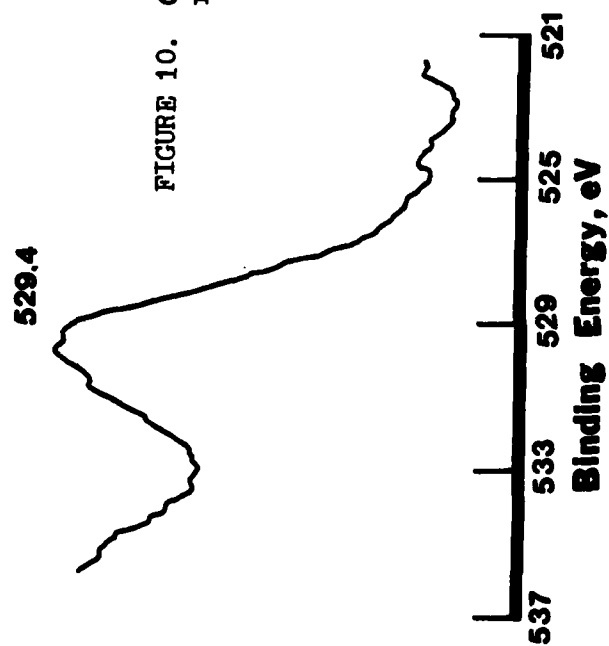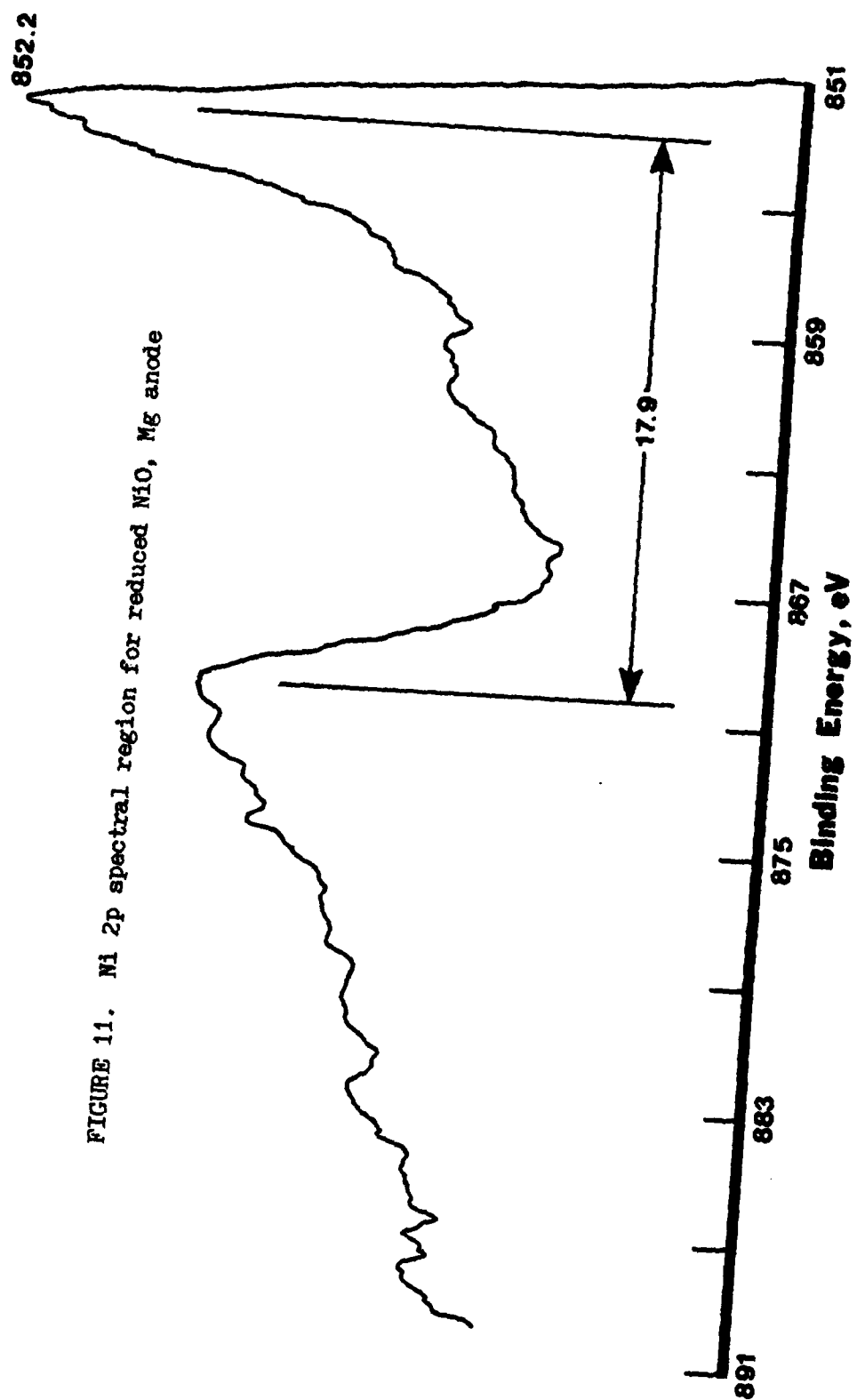
FIGURE 11. Ni 2p spectral region for reduced NiO, Mg anode

LOW ENERGY ELECTRON DIFFRACTION (LEED)

Low energy electron diffraction (LEED) is an incredibly useful tool for studying surface structures and has been used extensively in studying oxide structures on nickel and NiO (19-22). Throughout the oxide experiments, there were often problems due to surface charging and stray magnetic fields which made obtaining good LEED data difficult. The vacuum deposition of gold on a corner of the sample helpedalleviate the surface charging problem. A Mu metal shield around the outside of the LEED optics also reduced the stray magnetic field effects. Some good LEED data were obtained, and monitoring the status of the NiO crystal with LEED did yield much qualitative data regarding the general order/disorder of the crystal surface.

The remainder of this section will discuss the diffraction theory associated with LEED, the equipment used to obtain LEED data, and how to interpret LEED data.

<u>Surface structure and diffraction patterns</u>. LEED can certainly be considered the two-dimensional analog to x-ray crystallography. The definition and classification of surface structure follows much the same rules as that for x-ray diffraction. The reader is referred to several good references (4, 23, 24) for understanding the methodology of surface structures.

The de Broglie equation can be used to convert electron energy into a wavelength:

$$\lambda = \frac{h}{mv} \quad ,$$

where λ is the wavelength of electrons associated with a mass m and

velocity v, and h is Planck's constant. It follows from this equation
that the wavelength of 66 eV electrons (used in this study) is 1.51 $\mathring{A}$.
Therefore, one would expect interference with crystal lattices and
subsequently a diffraction pattern. Applying the Bragg equation to
the nomenclature of Ertl and Kuppers (4), an incoming wave striking
a surface at an incident angle of φ_0 will cause interference of the
backscattered waves in directions φ by the following relationship:

$$a (\sin \varphi - \sin \varphi_0) = n\lambda.$$

In the above equation, a is the distance between scatterers and n is
an integer representing the order of diffraction. This scattering
is represented in one dimension in Figure 12a. If the incoming beam
is normal to the surface, as is the case in the LEED experiments,
φ_0 becomes 0° and the previous equation becomes

$$a (\sin \varphi) = n\lambda.$$

This situation is depicted in Figure 12b.

These diffracted beams create a series of diffraction maxima
which appears as dots on a fluorescent screen during LEED experiments
and represent the reciprocal lattice of the surface. This reciprocal
lattice can easily be converted into a real lattice, thus yielding
the geometry of the unit cell. The analysis of an actual LEED
diffraction pattern appears in the upcoming Analysis of data portion
of this section.

The LEED diffraction pattern is determined by elastically
scattered electrons. However, the intensities of elastically
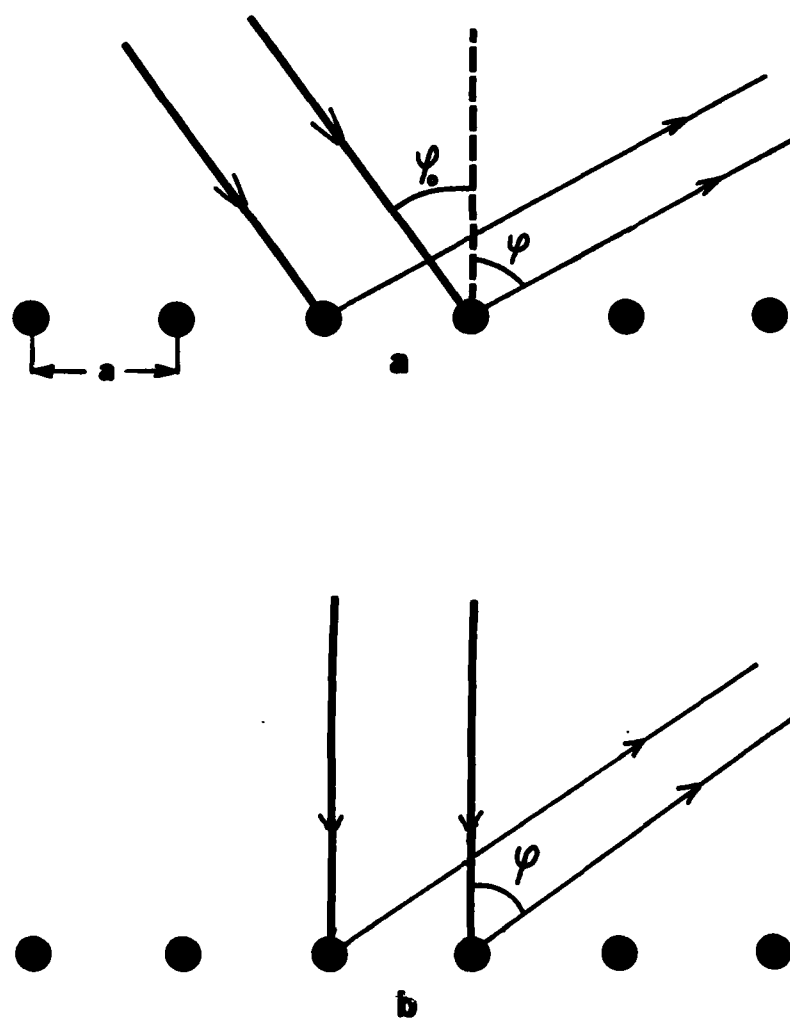
FIGURE 12.   Schematic of electron beam diffraction for LEED

scattered electrons are typically only about 2% of the incident

current. The creation of plasmons, or charge density waves, is one

of the primary energy loss mechanisms, along with a mixture of

plasmon-single particle losses. Secondary electrons electrons also

contribute to energy losses, when energies comparable with those

of inelastically scattered electrons are transferred to electrons

in the crystal. Auger electrons contribute to the secondary

electron process. Although small in magnitude, incident electrons

can also lose energy to the crystal by scattering off a phonon.

All of these loss mechanisms affect the intensity of the elastically

scattered beams. In addition, the inelastically scattered electrons

produce a more or less uniform background intensity upon the discrete

beams from the elastically scattered electrons, which gets nulled out.

Electrons can also be deflected from their straight flight by stray

magnetic fields (23).

Experimental Method. The LEED system used in these studies has

two basic components: An electron gun and a retarding field analyzer

detector system. A schematic of the system is shown in Figure 13.

The electron gun provides a beam of focused (less than 1 mm in

diameter at the sample), monoenergetic electrons whose energy can

be varied from 0 to 1600 eV. The electron source is a heated thorium-

iridium cathode. At beam energies of less than 50 eV, it may be

advantageous to operate the electron gun in the retarding mode. This

is accomplished by inserting a fixed bias between V_3 (see Figure 13)

and ground (sample potential). This bias is V_g in Figure 13. The

retarding mode allows the gun to be operated without internal space
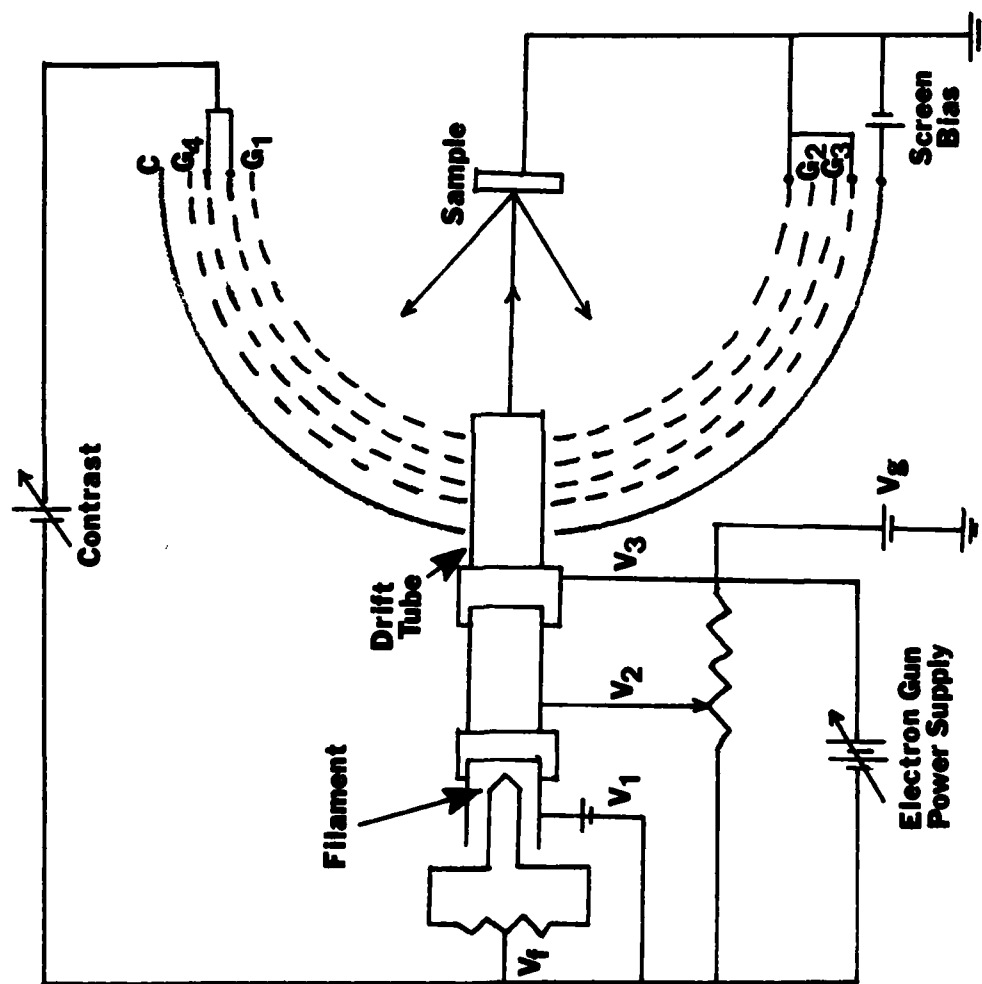
FIGURE 13. LEED system schematic

charge problems and allows the beam voltage (now equal to $V_3 - V_f - V_g$) to be swept through zero (8).

As shown in Figure 13, the detector system is four concentric, hemispherical grids and a concentric phosphor-coated collector. The first grid (G_1), drift tube, and sample are grounded so that the electrons scattered from the sample are not deflected electrostatically in the region between the sample and the first grid. The two middle grids (G_2 and G_3) are operated at the same voltage; a voltage slightly less than the filament potential. Since this voltage is slightly less than the primary beam energy, G_2 and G_3 will repel the inelastically scattered electrons. After passing through G_2 and G_3, the electrons pass through G_4 which is operated at the sample potential to help shield the electron trajectories, thus improving resolution. Finally, the electrons impinge on the phosphor collector (C), which is typically operated at +4 KV with respect to ground to provide enough energy to excite the phosphor. The impinging electrons create a spot on the phosphor screen collector (4,8). Both Ertl and Kuppers (4) and Pendry (23) give good discussions about the experimental requirements for LEED studies.

Analysis of data. As mentioned previously, the geometry of the unit cell of the sample can be determined by analysis of the LEED pattern. Figure 14 shows actual LEED patterns for the stoichiometric NiO (100) surface with 66 eV and 91 eV electrons. These same patterns are reproduced by drawings in Figure 15, which also shows the numbering nomenclature typically used to identify LEED dots. The incoming electron beam diffracted with $\varphi = 0$ back to the screen
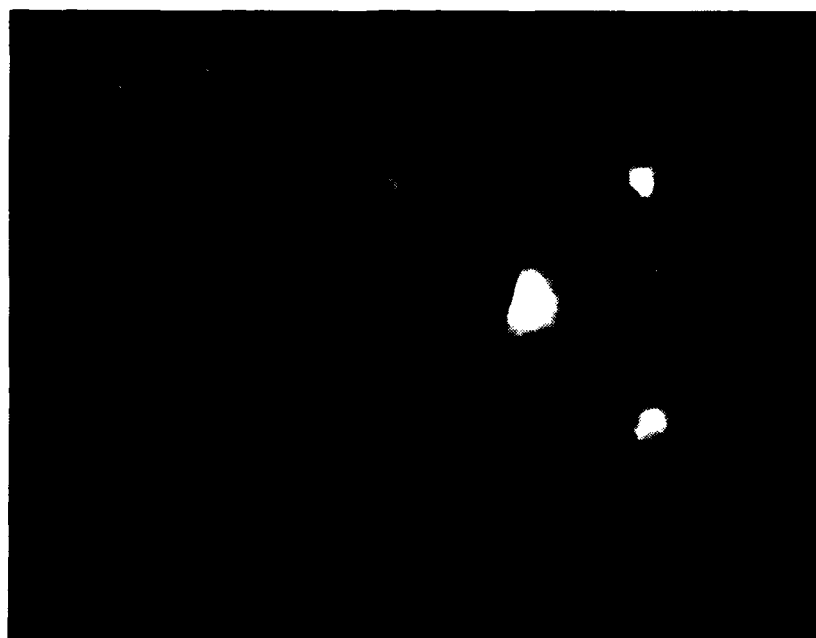
(a) 66 eV

FIGURE 14.   Photographs of LEED
pattern for
stoichiometric
NiO (100)
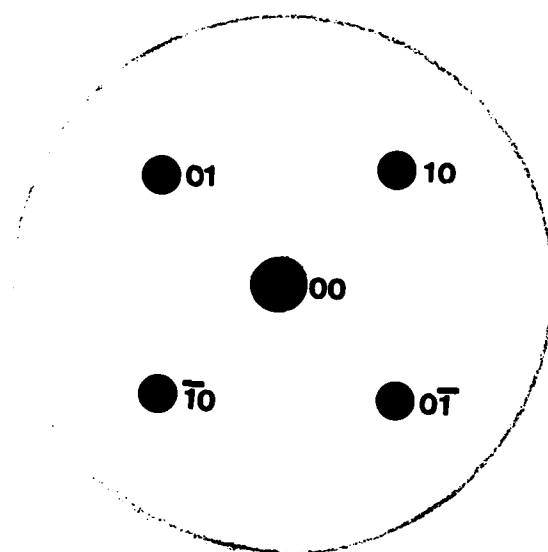
(b) 91 eV

a. 66 eV

FIGURE 15. Drawing of LEED pattern for
stoichiometric NiO (100)
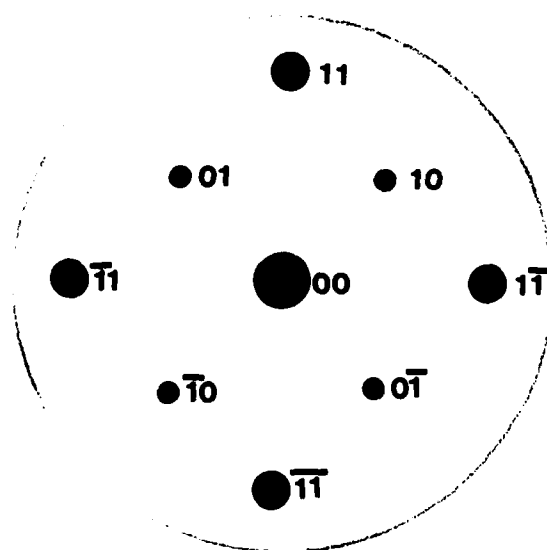
b. 91 eV

is assigned 00. The "$\bar{1}$" indicates a "-1" on an x-y coordinate scheme.

Both Figures 14 and 15 show the two dimensional symmetry of the

crystal surface; that is, the 10 and 01 spots are at 90° to each

other through the 00 spot and are the same distance from the 00 spot.

This "square symmetry" aids greatly in the interpretation of the

pattern, since a square transposes directly from reciprocal space

to real space, whereas other unit cell shapes do not. Figure 16

shows how real and reciprocal space correspond in several two-

dimensional unit cells. In Figure 15, the 10 beam is closer to the

00 beam at 91 eV than at 66 eV. This is expected, since λ at 66 eV

is 1.51 $\overset{\circ}{A}$ and λ at 91 eV is 1.29 $\overset{\circ}{A}$.

Since λ is known, the LEED pattern can be analyzed to find

the scatter angle φ, which allows the calculation of the distance

between scatterers a, yielding the dimensions of the unit cell of

the surface. Figure 17 is a full scale drawing of the LEED system

used in these experiments, based on the manufacturer's specifications.

The camera reduced the actual size of the image. All measurements

from the photographs must be multiplied by 1.35 to yield the actual

distance. The camera was focused on the dot-dashed line shown in

Figure 17. At 66 eV, the 10 beam appears from the photo in <u>actual</u>

dimensions as the open circle in Figure 17 in one-dimension. The

photo is flat, whereas the collector screen is curved; hence, the

beam on the picture actually appears as the closed circle on the

curved collector in Figure 17. The scatter angle φ is, then,

the angle between the incoming beam (dashed line perpendicular to the

sample) and the solid line drawn through the center of the closed
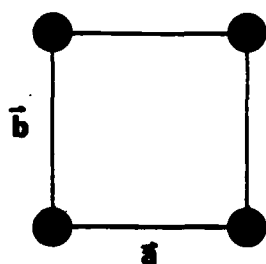
REAL   **RECIPROCAL**
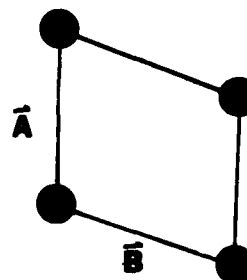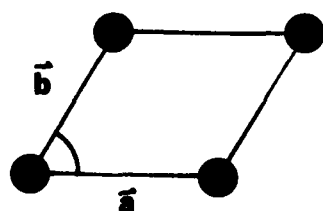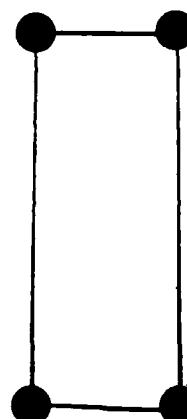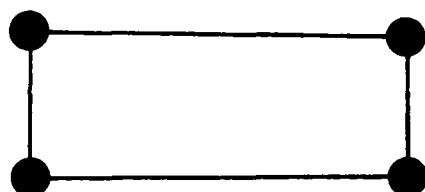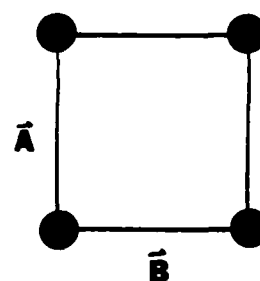
FIGURE 16. Real versus reciprocal space

39
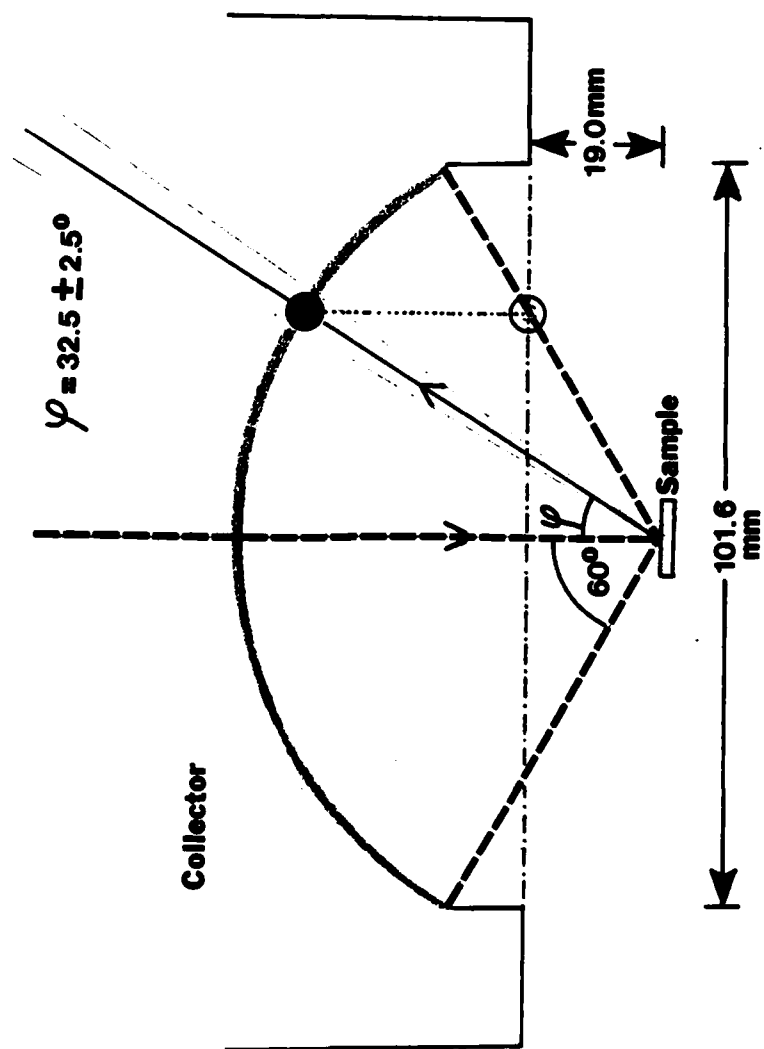
FIGURE 17. LEED system geometry

$\varphi = 32.5 \pm 2.5^{0}$

19.0mm

101.6 mm

Sample

60⁰

Collector

circle. In this example, $\varphi = 32.5 \pm 2.5°$. Substituting $\varphi = 32.5 \pm 2.5°$, $\lambda = 1.51$ Å and n = 1 into the equation $a(\sin\varphi) = n\lambda$, one obtains a value for a of $2.81 \pm .21$ Å. Since the LEED pattern is a square, the 01 beam will have the same value for a.

A drawing of the bulk crystal structure of NiO is shown in Figure 18, as well as of the (100) face. The unit cell dimension (with two Ni's and two O's in the unit cell) is $a = 4.1769$ Å (25). This distance a is the distance between two nickel scatterers in the (100) plane. It is known that the surface lattice dimensions for nickel oxide do not vary from the bulk parameters (26). This allows for a convenient calibration of the LEED system. The corresponding unit cell value calculated from the LEED photo is $5.62 \pm .42$ Å. Since it is known that the unit cell value is actually 4.18 Å, a correction factor of 0.74 is obtained which accounts for the distortion of distances by the photograph.

Changes in the positions, number, and intensity of the beams at constant electron energies can yield information about the changing structure of a surface as it is treated, as well as information about the structure of an adsorbed layer of molecules. Although not performed in this study, an analysis of the intensity of the diffraction beams must be made to determine how atoms are arranged within the unit cell. Pendry (23) gives a very good discussion about pattern intensity interpretation, including computer programs to calculate LEED intensities. Van Hove and Tong (24) also give a detailed LEED computer program.

41
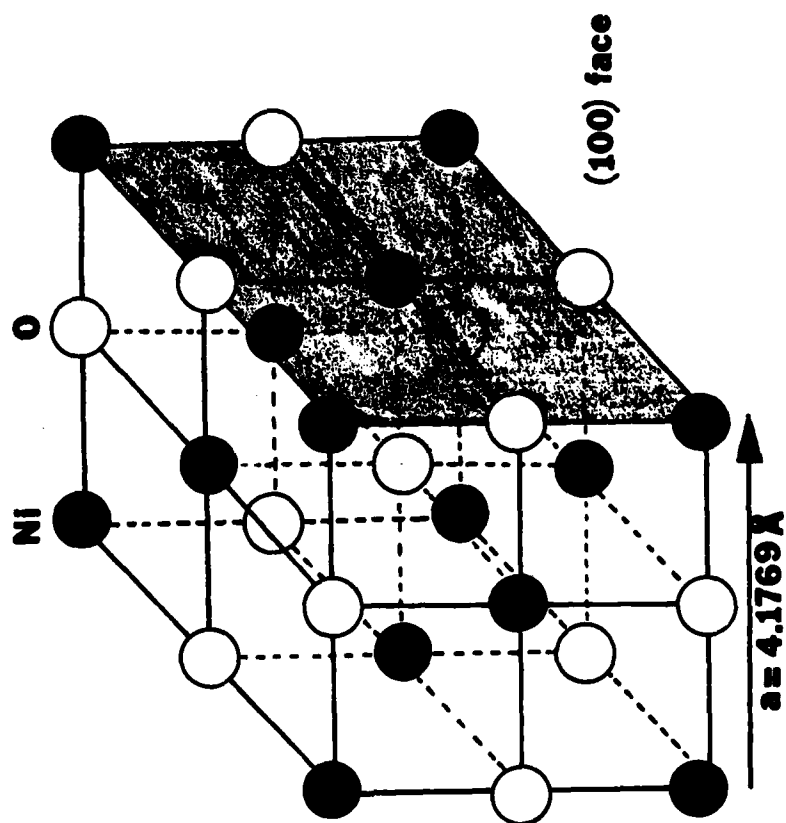
FIGURE 18. Drawing of NiO crystal structure and (100) face

EXPERIMENTAL

DESCRIPTION OF APPARATUS

All of the experiments on the NiO crystal were performed under ultra-high vacuum (UHV, base pressure of 2.0 X 10^{-10} Torr) in a stainless steel chamber designed and built by Perkin-Elmer Physical Electronics Division (PHI). Figure 19 shows a cross-section of the 40 liter chamber, or bell jar, assembly. The bell jar is equipped with various equipment ports and viewports. The remainder of this section will briefly describe the apparatus used in these experiments. The descriptions were written with the aid of the Perkin-Elmer users' manuals (8). The intent of this section is to provide the reader with specific knowledge of the type of equipment used, not to provide details about the equipment design and operation. Equipment design and operation, along with circuit and block diagrams, are included in detail in the users' manuals.

1. The Auger/ESCA System.

a. The <u>PHI Model 11-055 ESCA/Auger System Control</u> accepts an external ramp voltage to digitally generate a ramp voltage using signals from internal circuitry. The 11-055 controls the sweep range and sweep rate of the cylindrical analyzer. The 11-010 Electron Gun Control and 20-075 Electron Multiplier Supply (both discussed later) are interlocked with the ESCA/Auger System Control to prevent use of the electron gun when not in the Auger mode and to prevent damage to the electron multiplier when switching modes of operation.
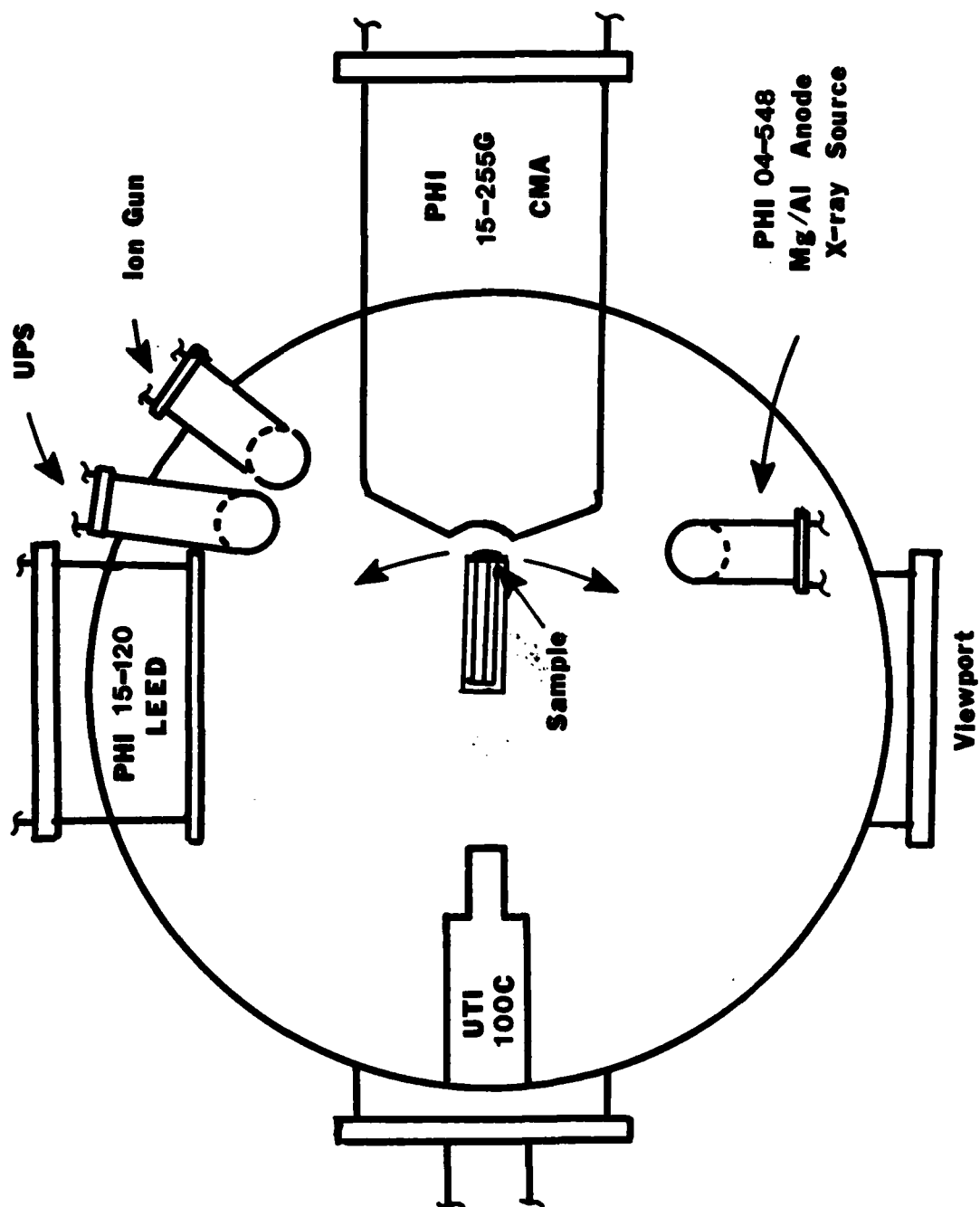
FIGURE 19. Cross-section of bell jar assembly

b. The <u>PHI Model 20-805 Analyzer Control</u> allows the user to select the electron energy analyzer's mode of operation (ESCA, Auger, or UPS). In addition, the user can select the pass energy for the retarding mode of operation when in pulse count and the amplitude of the output voltage modulation when in the lock-in mode of detection.

c. The <u>PHI Model 32-010 Lock-in Amplifier</u> provides analog signals for the System Control when in the Auger mode and provides y-axis inputs to the x-y recorder. A more detailed discussion of the function of the lock-in amplifier can be found in the AES THEORY section of this thesis.

d. The <u>Princeton Applied Research Model 1105 Photon Counter/Data Converter</u> is used to process digital pulse count signals from the electron analyzer in the ESCA mode of operation.

e. The <u>PHI Model 15-255G Precision Electron Energy Analyzer</u> filters and detects signals from samples excited by an electron beam, an x-ray source, or an ultraviolet source. The energy analysis is accomplished with three energy filters-- one hemispherical retarding grid system (used only in the pulse count mode) and two cylindrical mirror analyzers (used in all modes)-- arranged in a series. The detection of the signal is accomplished by a spiraltron (electron multiplier). The 15-255G is equipped with a variable internal aperture within the energy analyzer with an external control to provide a maximum of flexibility for using the analyzer in an AES or XPS mode. An electron gun is mounted within the analyzer which provides an electron beam normal to the sample when operating in the Auger mode.

f. The <u>PHI Model 20-075 Electron Multiplier Power Supply</u> provides DC voltages from 0 to 3000 Volts to the spiraltron in the 15-255G energy analyzer.

g. The <u>PHI Model 11-010 Electron Gun Control</u> provides the power supplies necessary to operate the electron gun in the energy analyzer, which generates the Auger signals. Beams as high as 5 kV can be generated.

h. The <u>PHI Model 04-548 Dual Anode X-ray Source</u> generates x-rays from an aluminum or magnesium anode for the ESCA system.

i. The <u>PHI Model 32-095 X-ray Source Control</u> and <u>14-040 DC Power Supply</u> control and supply the power necessary to energize the aluminum and magnesium anodes of the x-ray source.

j. The <u>PHI Model 16-020 Heat Exchanger/Deionizer</u> circulates, cools, and deionizes water which is used to cool the x-ray source.

2. The Low Energy Electron Diffraction (LEED) System.

a. The <u>PHI Model 15-120 LEED Optics</u> contains a low energy electron gun which produces a beam less than 1 mm in diameter at and normal to the sample surface. The diffracted electrons pass through four chrome-plated stainless steel mesh grids. The angle subtended by the inner-most gird is 120°. The display is a phosphor-coated stainless steel collector. The hemisphirical grid system allows only electrons which have not lost energy upon interaction with the sample to be displayed on the phosphor screen.

b. The <u>PHI Model 11-020 LEED Electronics</u> provides power and focus control for the 15-120 LEED optics. The electron beam voltage is scanned manually to within 1 eV. The 11-020 can operate the system

in a retarding mode to achieve low incident electron energies while maintaining useful beam current levels.

3. The Mass Spectrometer System. The quadrupole mass spectrometer is a <u>UTI Model 100C Precision Gas Analyzer</u> with a 1-300 AMU mass range. The mass spectrometer was used to monitor the background gases in the chamber and the purity of gases used in adsorption studies and sample treatment. Although not used for such in this study, the Model 100C is capable of use in thermal desorption analysis (see Appendix).

4. Sputter Gun System. The <u>PHI Model 04-161 Sputter Ion Gun</u> and the <u>PHI Model 20-045 Sputter Gun Control</u> provides a system to sputter etch the sample using argon ions. Beams up to 2 kV can be generated.

5. Sample Positioner. The <u>PHI Model 10-504 X-Y Manipulator</u> is used to rotate the sample to the correct position for Auger, ESCA, or LEED work. The manipulator can move the sample up and down (z direction), in the x and y directions, as well as rotate the sample 360°. The manipulator can also tilt the sample about two axes.

6. Leak Valve. The <u>Varian Model 951-5106 Variable Leak Valve</u> was used to admit gases into the chamber for sample treatment and adsorption studies.

7. Vacuum Pumping System.

   a. The bell jar is equipped with two <u>Perkin-Elmer Ultek Model 236-1510 Sorption Pumps</u>. The sorption pumps serve as the system roughing pumps. The pumps contain molecular sieve, a processed mixture of aluminum and silicon oxides with an extremely high surface

to volume ratio, which acts as an effective getter when cooled with liquid nitrogen. The sorption pumps rough the chamber from atmosphere to the millitorr range in less than 10 minutes.

b. The ultra-high vacuum is obtained with the Ultek Boostivac High Vacuum Ion Pump and Control Unit. The Model 210-8033 has a 220 l/s differential ion pump and a titanium sublimation pump capable of vacuums in the 10^{-4} to 10^{-11} Torr range.

c. The pressure in the chamber is measured by a Perkin-Elmer Digital Gauge Control III. The system controls a nude Bayard-Alpert gauge tube which has two tungsten filaments and operates in the range of 10^{-4} to 10^{-11} Torr. When water or hydrogen was used, the controller was set to compensate the gauge for these molecular weights. For all other gases, the controller was set for nitrogen.

The sample was mounted on a stainless steel support and insulated from direct contact with the stainless steel by aluminum oxide spacers. The sample was attached to the stainless steel support by three stainless steel screws, also insulated from the actual support. The temperature of the sample was measured using a chromel-alumel thermocouple attached to one of the mounting screws, which was in thermal contact with the sample. The sample was heated radiatively by a tungsten filament located directly behind the sample. The sample was cooled to 150K by flowing liquid nitrogen through a bellows assembly below and in thermal contact with the base of the sample mount.

PROCEDURES FOR CLEANING/ANNEALING THE SAMPLE

The nickel oxide sample used in these experiments was grown by the arc image method which produced a 1-cm diameter single crystal approximately 2-mm in thickness (27). The crystal was oriented to within $0.5°$ of the (100) face with Laue x-ray diffraction and polished using successively finer grades of alumina paste down to 0.03 micron particle sizes. The structure of the NiO crystal and the (100) face are shown in Figure 18.

Even at 2.0 X 10^{-10} Torr, assuming a sticking coefficient of unity, the sample can become contaminated with a monolayer of adsorbate in one hour according to the kinetic gas theory (4). Therefore, it is essential to have the capability to clean the sample being studied in situ. The remainder of this subsection describes the four step procedure used for perparing the NiO sample for an experiment.

First, the sample was sputter-etched by argon ion bombardment. This step removes the top layers of atoms from the surface yielding a fresh, but uneven, NiO surface. The ion bombardment technique is probably the most common method for cleaning a sample in situ and is used by nearly all of the investigators cited in this thesis. The UHV chamber is filled with argon gas to a pressure of 5 X 10^{-5} Torr. Before admitting the argon with the leak control valve from the gas inlet manifold system, the manifold was flushed with argon three times to insure the purity of the argon in the manifold. The Varian Model 951-5106 variable leak valve was then used to admit gases into the UHV chamber, with the pressure of the

chamber being read with the Bayard-Alpert gauge. Once the pressure gauge read 5×10^{-5} Torr, the ion sputter gun was turned on. The gun was operated with a filament current between 25 and 30 milliamps and a beam voltage of 2 KV, yielding a surface beam current of about 14 micoramps/cm^2. The gun ionizes the argon atoms, which in turn are accelerated toward the NiO sample. The bombardment of the sample by the argon ions serves to sputter-clean the surface. The argon ion bombardment procedure was continued for 20 minutes, which removed up to 100 monolayers from the surface.

Next, the sample was annealed in oxygen. This was accomplished by first heating the sample radiatively to 250-300°C with a tungsten heating filament. Once this temperature was reached, oxygen was admitted to the system at a pressure of 5×10^{-7} Torr. This was continued for 15 minutes.

Thirdly, the sample was cooled in oxygen. This was done simply by shutting off the heating filament and letting the sample cool in oxygen at 5×10^{-7} Torr for 10 minutes.

To complete the cleaning/annealing process, the oxygen to the system was shut off and the sample again heated to 250-300°C in UHV. The sample was allowed to anneal at this temperature under vacuum for 10 minutes and subsequently allowed to cool to room temperature.

The result of this four step procedure was a very stoichiometrically reproducible (to within 1%) nickel oxide surface, as determined by Auger electron spectroscopy. This surface became the stoichiometric, "clean" NiO surface used extensively throughout this research.

PROCEDURE FOR REDUCING THE SAMPLE

Throughout this research effort, the stoichiometric NiO (100) surface often proved to be very unreactive toward the adsorption of gas molecules at temperatures from 200-600K. In an effort to activate the surface, the surface was reduced in hydrogen to create oxygen defects in the NiO (100) which would make the surface more reactive. A considerable amount of effort of this thesis work was dedicated toward understanding the reduction process of NiO (100).

The RESULTS AND DISCUSSION portion of this thesis describes in detail the various conditions used to study the reduction of NiO (100). However, to create the surface referred to as "reduced NiO (100)" in subsequent adsorption experiments, the sample was normally heated to 300-350°C and exposed to hydrogen at a pressure of 1.0×10^{-6} Torr. The time for the reduction process was then varied to obtain the desired "degree of reduction" as measured by the relative concentrations of the nickel and oxygen from the AES. This time was usually between one and two hours. As presented in the RESULTS AND DISCUSSION section, the reduction could be accomplished to yield a continuous range of NiO_x, with x ranging from 1 to 0.

The same leak valve and manifold procedures were used for hydrogen except that the manifold was only flushed once. This is because the H_2 gas, due to its small molecular size, is not pumped very well by the system sorption pumps.

INSTRUMENT SETTINGS FOR AES AND XPS MEASUREMENTS

The following instrumentation settings/parameters for Auger electron spectroscopy were used for all Auger spectra taken in this study:

Sweep range: 1000 eV
Lower limit: 70 eV
Upper limit: 1070 eV
Sweep rate: 5 eV/sec
Modula ion energy: 2 eV
Electron beam energy: 2 kV
Emission filament current: 0.5 mA
Primary current: 3.4 microamps (measured with volt meter, this value changes and cannot be measured in all cases.)
Time constant: 0.1 sec
Sensitivity: 10X (40X for carbon peak expansions)
Electron multiplier: 1250 V

The following instrumentation settings/parameters for x-ray photoelectron spectroscopy were used for XPS spectra taken in this study:

Type of anode: indicated on each spectrum
Voltage of x-ray generator: 15 kV DC
Current to generator: 20 mA DC
Power to anode: 300 Watts
Response time: 20 msec
Pass energy: 100 eV
Electron multiplier: 2100 V
Sweep range: 50 eV

For Ni 2p

Sweep rate: 0.4 eV/sec
Time constant: 1 sec
Counting range: 30K

For O 1s

Sweep rate: 0.1 eV/sec
Time constant: 10 sec
Counting range: 3K

For Au 4f

Sweep rate: 0.1 eV/sec
Time constant: 10 sec
Counting range: 1K

For C 1s

Sweep rate: 0.1 eV/sec
Time constant: 10 sec
Counting range: 1K

Full range sweeps

Sweep rate: 1.0 eV/sec
Time constant: 1 sec
Counting range: 30K
Sweep range: 1000 eV

USE OF THE Au 4f PEAKS FOR XPS REFERENCE

To make XPS measurements consistent from system to system and to eliminate surface charging effects, investigators normally reference XPS spectra to a peak or line whose location is generally agreed upon by convention. For these experiments, the Au 4f lines are used as the reference peaks. More specifically, the Au $4f_{7/2}$ line is taken to be at 84.0 eV binding energy, though this value may vary slightly ($\pm$ 0.2 eV) from reference to reference. The gold was vacuum evaporated onto the NiO (100) crystal, depositing a thin, visible gold layer on about one-fourth of the crystal. Then, each time an XPS spectrum was taken, a spectrum of the Au 4f region was also taken and the value of all observed peaks were adjusted by the amount the Au $4f_{7/2}$ peak differred from 84.0 eV. The observed Au $4f_{7/2}$ peak was always between 82.8 and 83.6 eV. There were no changes in the XPS or AES of the NiO with or without the gold present.

Since the NiO sample charges, it was necessary to make sure all of the observed peaks were affected the same amount by charging so that the Au 4f peaks could be used a reference. A known, constant potential of 9.1 V was applied to the sample using a dry cell battery. The shifts in the Au 4f, Ni 2p, and O 1s peak positions were then observed. These spectra are shown in Figures 20, 21, and 22. Note in Figure 20 that the exact location of the Au $4f_{7/2}$ peak was difficult to pinpoint with the battery since the peak flattens out considerably. Therefore, it is better to observe the shift in the Au $4f_{5/2}$ (78.1 eV with the battery). Upon examining Figures 20, 21, and 22, the shifts in peak positions is 9.1 $\pm$ 0.2 eV, which
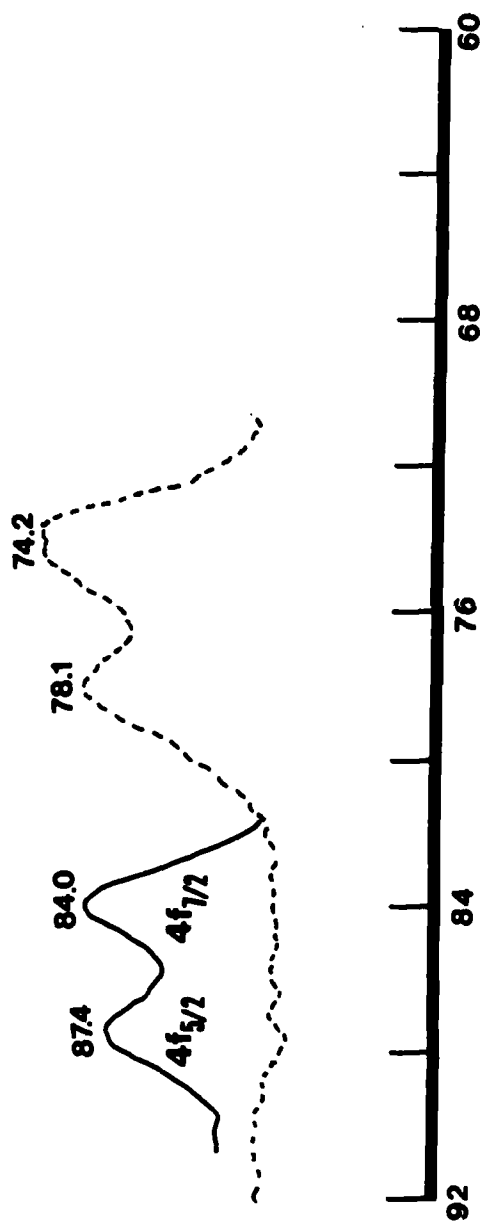
FIGURE 20. Au 4f spectral region for gold vacuum-deposited on NiO (100), Al anode

Ni 2p

— w/o battery
---- with battery

852.2

843.0

875   867   859   851   843
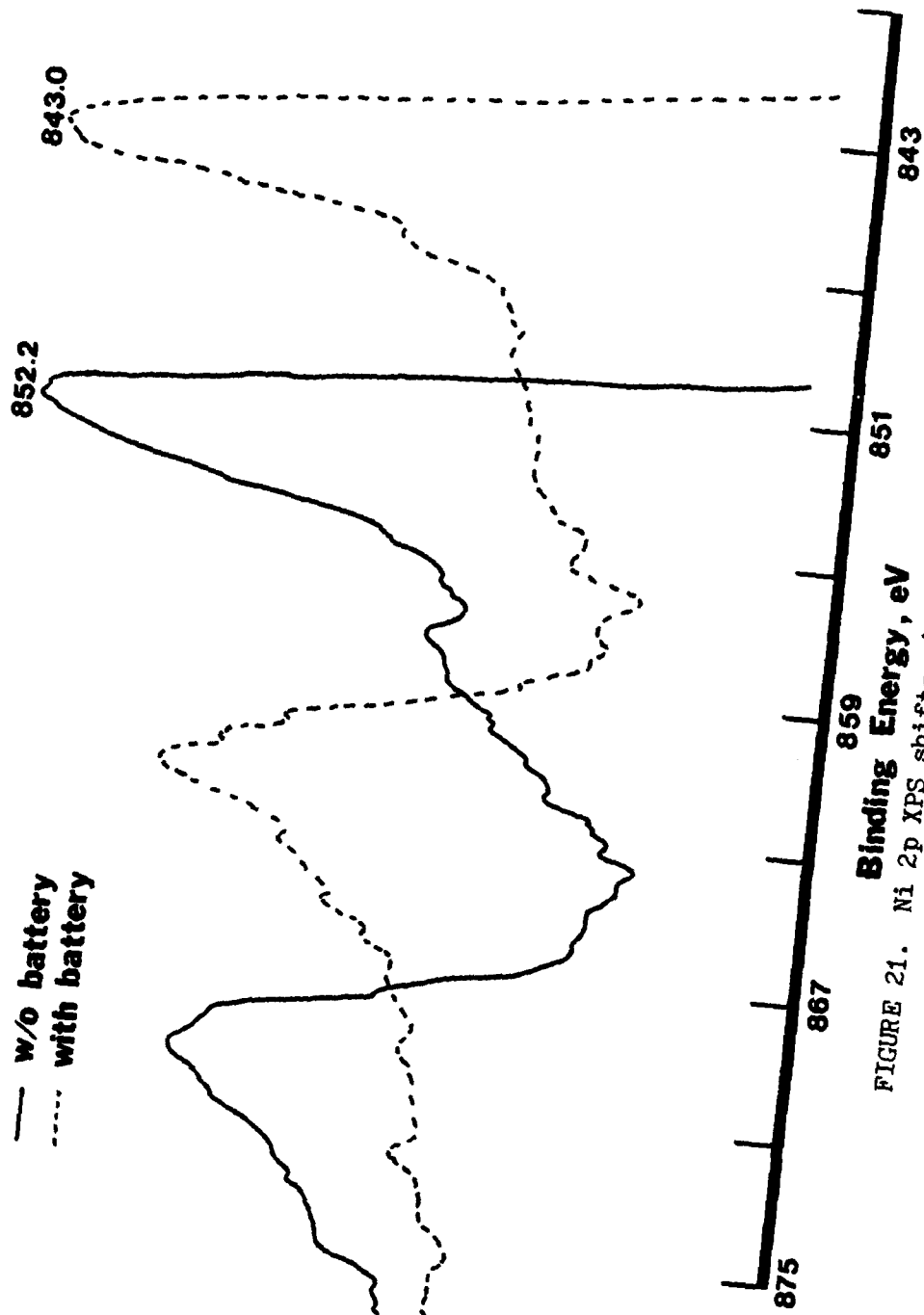
Binding Energy, eV

FIGURE 21. Ni 2p XPS shifts with applied voltage, Al anode

54

O 1s
—— w/o battery
----- with battery

520.4

529.4

513

521

529

537

Binding Energy, eV
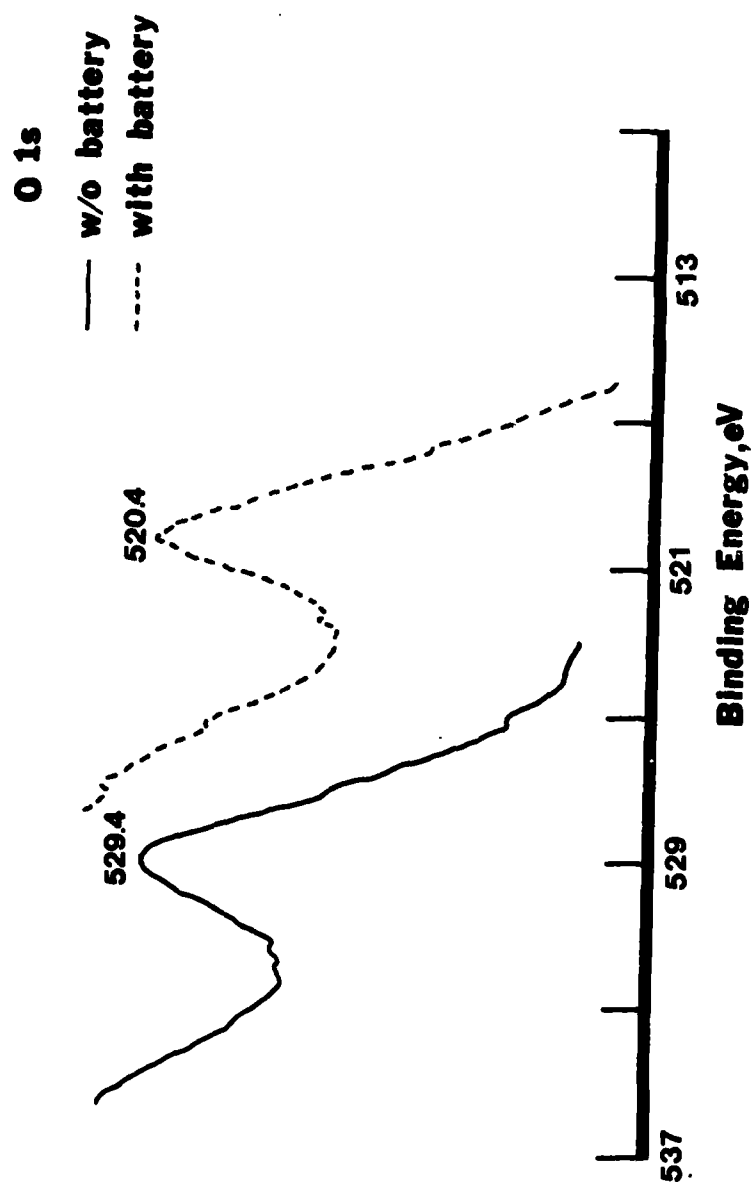
FIGURE 22. O 1s XPS shifts with applied voltage, Al anode

is within experimental error. Thus, it can be assumed that if the
NiO crystal charges, the observed peaks will all be affected the
same amount and can be referenced to the Au 4f peaks.

RESULTS AND DISCUSSION

REDUCTION OF NiO (100)

An important feature in gas adsorption by metal oxides is how oxygen lattice defects and vacancies affect the adsorption process. Thus, it was decided to study the effect of oxygen non-stoichiometry on the adsorption of gases used in this thesis work. Before this could be done, however, a procedure needed to be developed to create the oxygen vacancies or, effectively, reduce the NiO surface. It was also necessary to characterize the reduced surface to know what type of surface was being used for adsorption. This section will discuss the results of the hydrogen reduction process of NiO (100).

Stoichiometric NiO (100) surface structure. Before beginning the reduction process, it was necessary to characterize the surface of the starting material; that is, the surface of the stoichiometric NiO (100). Kinniburg and Walker (44) showed, using LEED, that the surface geometry of NiO (100) is within 5% of the bulk. Therefore, two structures are possible for the stoichiometric surface and are illustrated in Figure 23. In Structure #1, the surface has bulk termination with a complete oxide layer. In Structure #2, the surface terminates with bulk symmetry and spacing, so the top layer of oxygens is not present. The Auger layer model from the THEORY section can be applied to each proposed structure to distinguish between the two. Using the layer model for Structure #1, the calculated Ni/O peak intensity ratio is 0.52. The calculated Ni/O peak intensity ratio for Structure #2 is 0.70. Since the observed ratio for stoichiometric NiO (100) is 0.48, Structure #1 is the
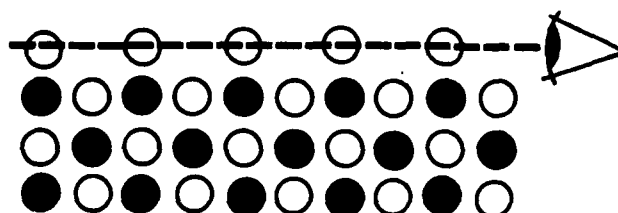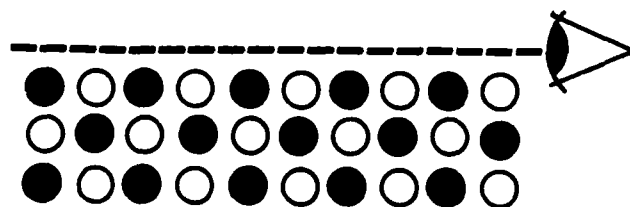
FIGURE 23. Proposed surface structures for stoichiometric NiO (100)

actual structure model. It is this surface structure which is the starting point for the reduction study.

Study of reduction kinetics using AES. The experimental process for reducing the sample is described in detail in the EXPERIMENTAL section of this thesis. Numerous workers have used similar processes (28-30). To develop a better understanding of the reduction process, an effort was initiated to study the time-dependence of the reduction at various crystal temperatures and hydrogen pressures. The temperatures and pressures used were $350^\circ C$ (623K), $250^\circ C$ (523K), $150^\circ C$ (423K) and 1.3×10^{-6} Torr, 7.0×10^{-7} Torr, and 1.0×10^{-7} Torr. Although monitored periodically with XPS and LEED, the reduction process with respect to time was monitored in detail with AES by examining the peak-to-peak intensity ratio of the nickel $L_3M_{4,5}M_{4,5}$ transition at 848 eV to the oxygen KL_2L_2 transition at 508 eV. These peaks are identified in Figure 24. The increase of the Ni-to-O peak ratio indicated that the relative atomic concentration of nickel on the surface was increasing with respect to that of oxygen. The increased intensity of the nickel 848 eV peak relative to the oxygen 508 eV peak upon reduction is very obvious in Figure 24. There are other apparent changes when comparing the stoichiometric and reduced NiO Auger spectra. Although there are no shifts in the Auger peak locations, there is a pronounced splitting of the first and second nickel peaks for the reduced sample; peaks occurring at 709 eV and 775 eV which are barely visible in stoichiometric NiO. The splitting is actually an increase in intensity for certain transitions. The nickel region

FIGURE 24. AES of stoichiometric and reduced NiO (100)
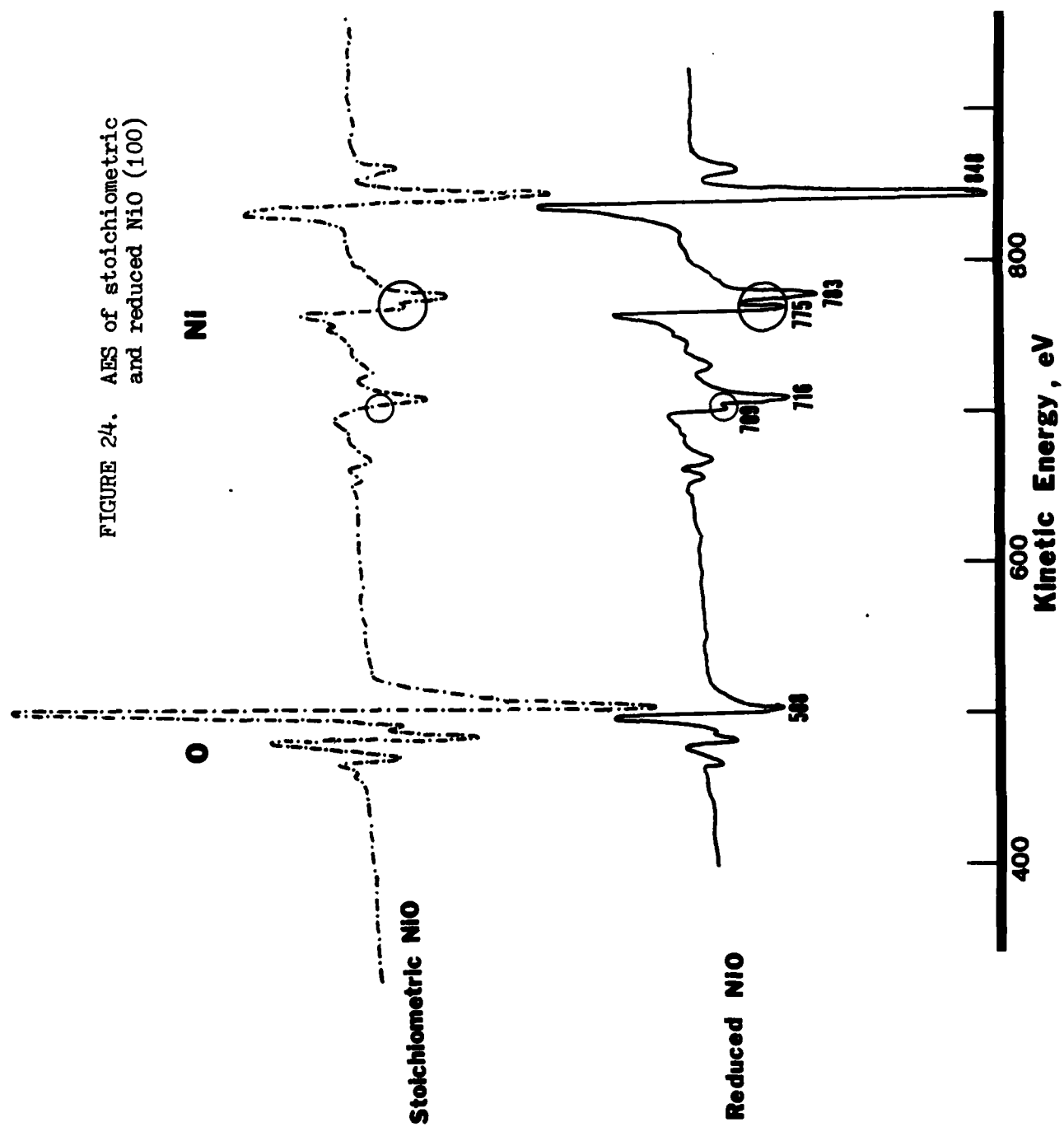
for the reduced sample in Figure 24 corresponds very closely to the
identical region for pure nickel as given by Davis et.al. (5) and
thus reduction produces a nickel-like surface.

Figures 25, 26, and 27 show how the Ni/O peak ratios vary with
temperature at a constant H_2 pressure, while Figures 28, 29, and 30
show constant temperature data with varying pressure. The data at
each pressure and temperature are a compilation of several experimental
runs. Although not done for Figures 25-30, the Ni/O peak ratios can
easily be converted to atomic concentration ratios by the method
of Davis et.al. (5) mentioned earlier in this thesis. Since it
is the trends of the data which are important and the trends are
unaffected by conversion to atomic concentration ratios, the
conversion was not made for these figures.

Upon examining Figures 25, 26, and 27, it is clear that there is
a strong dependence of the reduction process upon temperature.
The temperature dependence is due to oxygen migration. The reduction
of the NiO (100) does not occur at temperatures less than $150^\circ C$
and is greatly accelerated at $350^\circ C$. Although Figures 28, 29, and 30
show that the reduction process is more rapid at higher H_2 pressures,
Figure 31 shows that this pressure dependence can be directly related
to flux. Instead of the time of H_2 exposure on the abscissa, the
data from Figure 28 appears as shown in Figure 31 when exposure in
Langmuirs (1 L= 10^{-6} Torr-sec) is on the abscissa. All of the data
fall reasonably well within each other, indicating the variation with
pressure is accounted for by the variation in flux.

FIGURE 25 Reduction of NiO.
$P_{H_2} = 1.3 \times 10^{-6}$ Torr,
variable temperature

62

FIGURE 26. Reduction of NiO. $P_{H_2} = 7.0 \times 10^{-7}$ Torr variable temperature

$P_{H_2} = 7.0 \times 10^{-7}$ Torr

● 350°C
◐ 250°C
○ 150°C

$\dfrac{Ni}{O}$ Auger peak ratio

Exposure time to H_2, minutes

63

FIGURE 27. Reduction of NiO. $P_{H_2} = 1.0 \times 10^{-7}$ Torr, variable temperature

Legend:
- ◆ 350°C
- ◇ 250°C
- ◇ 150°C

$P_{H_2} = 1.0 \times 10^{-7}$ Torr

Y-axis: $\frac{Ni}{O}$ Auger peak ratio (1.10, .90, .70, .50)

X-axis: Exposure time to H_2, minutes (50, 100, 150)

FIGURE 28. Reduction of NiO.
T= 350°C,
variable pressure

FIGURE 29. Reduction of NiO.
T= 250°C, variable pressure

Legend:
☆ 1.3 X 10⁻⁶ TORR
◐ 7.0 X 10⁻⁷ TORR
◆ 1.0 X 10⁻⁷ TORR

T= 250°C

Y-axis: $\frac{Ni}{O}$ Auger peak ratio (1.10, .90, .70, .50)

X-axis: Exposure time to H_2, minutes (50, 100, 150)

FIGURE 30. Reduction of NiO.
T= 150°C, variable pressure

FIGURE 31. Reduction of NiO. T= 350°C, variable pressure, Ni/O peak ratios versus exposure (L)

One feature apparent in most of the Auger peak ratio data is that there is an induction period for the reduction process. This induction period is the time frame (or H_2 flux) during which the Ni/O ratio does not increase or increases at a much slower rate than the steady state value. This induction period is followed by varying degrees of acceleration of th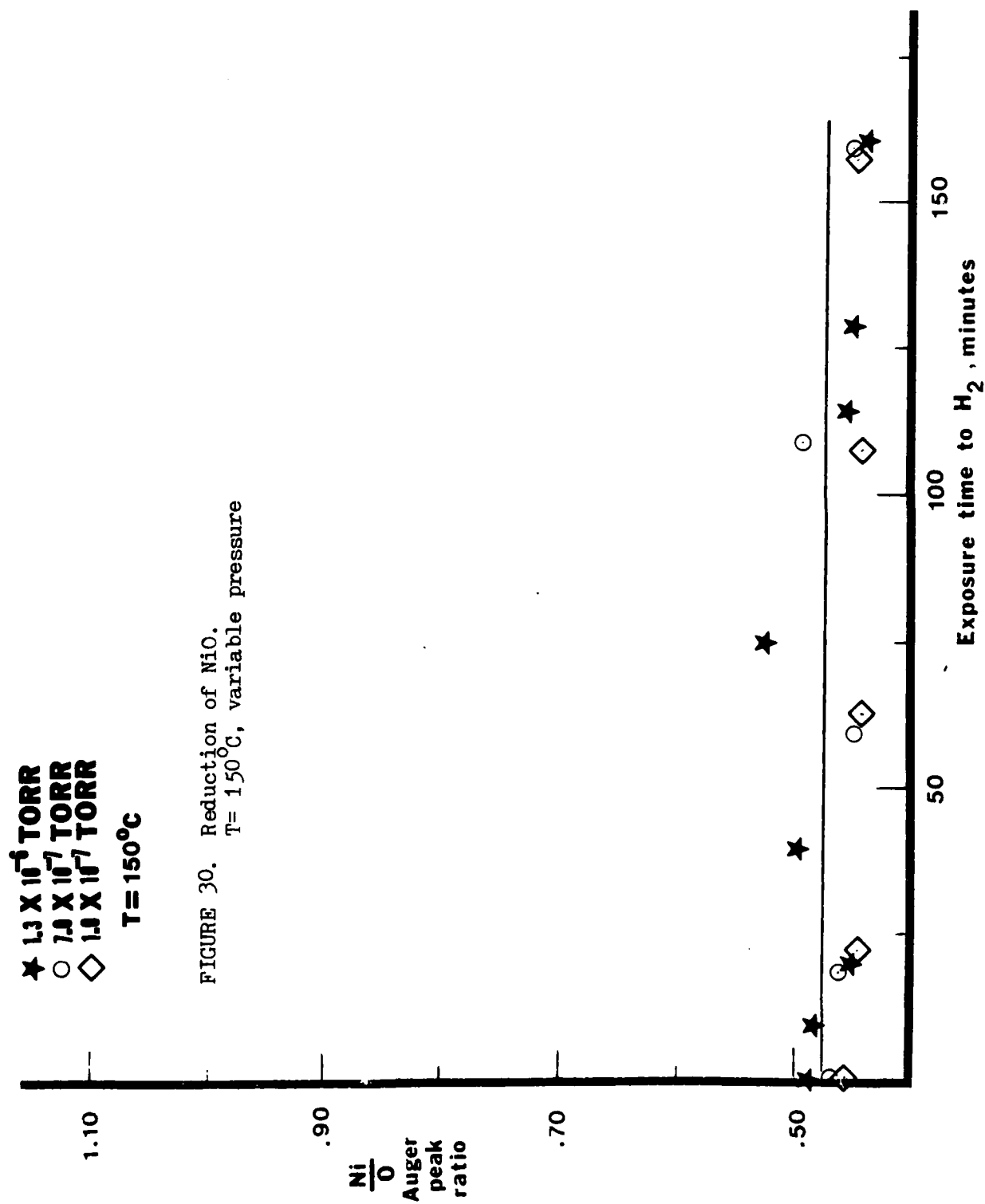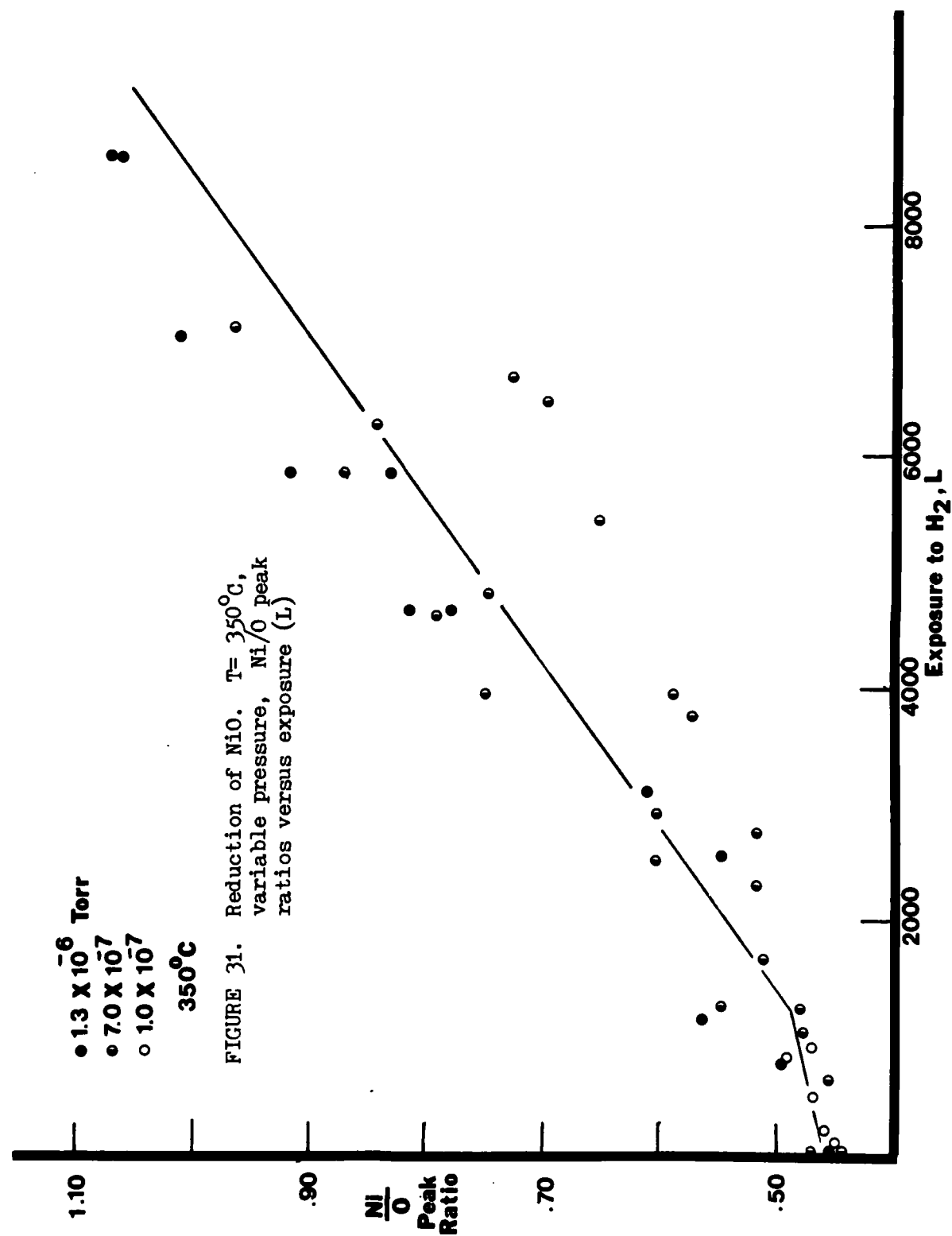e reduction process, depending on the pressure of H_2 and temperature of the sample. The induction periods for the various experimental conditions are displayed in Table I. Table I shows that at any given pressure, the induction time and flux decreases with increasing temperature. In addition, at any given temperature, the induction flux is nearly constant (flux independent).

XPS data. The XPS data also yield information regarding the nature of the reduction process. Figures 9 and 8 show the XPS spectra for stoichiometric NiO in the Ni 2p and O 1s spectral regions, respectively, while Figures 11 and 10 do the same for reduced NiO. Obvious intensity changes can be seen when the two sets of figures are compared. The O 1s peaks are compared directly in Figure 32. Figure 32 shows the symmetry in the O 1s peak for both the stoichiometric and reduced NiO surfaces. The highly symmetric O 1s peak suggests that there is only one type of oxygen pressent, with a binding energy of 529.4 eV. This type of oxygen is due to the lattice NiO oxygen. Figures 33 and 34 show that the heating of a reduced sample in vacuum for 35 minutes at 500K has no effect on the binding energy of the Ni 2p and O 1s peaks. As can be seen in Figure 34, the heating has no effect on the symmetry of the O 1s peak for the

TABLE I. Induction Time for H_2 Reduction Process

Induction Time (minutes)

Pressure of H_2	$350^{\circ}C$	$250^{\circ}C$	$150^{\circ}C$
1.3×10^{-6} Torr	$\lesssim 10$	50	no reduction
7.0×10^{-7} Torr	$\lesssim 25$	75	no reduction
1.0×10^{-7} Torr	$\lesssim 150$	--	no reduction

Induction Flux (L)

Pressure of H_2	$350^{\circ}C$	$250^{\circ}C$	$150^{\circ}C$
1.3×10^{-6} Torr	$\lesssim 780$	3900	no reduction
7.0×10^{-7} Torr	$\lesssim 1050$	3150	no reduction
1.0×10^{-7} Torr	$\lesssim 900$	--	no reduction

FIGURE 32. XPS peaks for stoichiometric NiO and reduced NiO, Mg anode

Reduced

Reduced, after heating
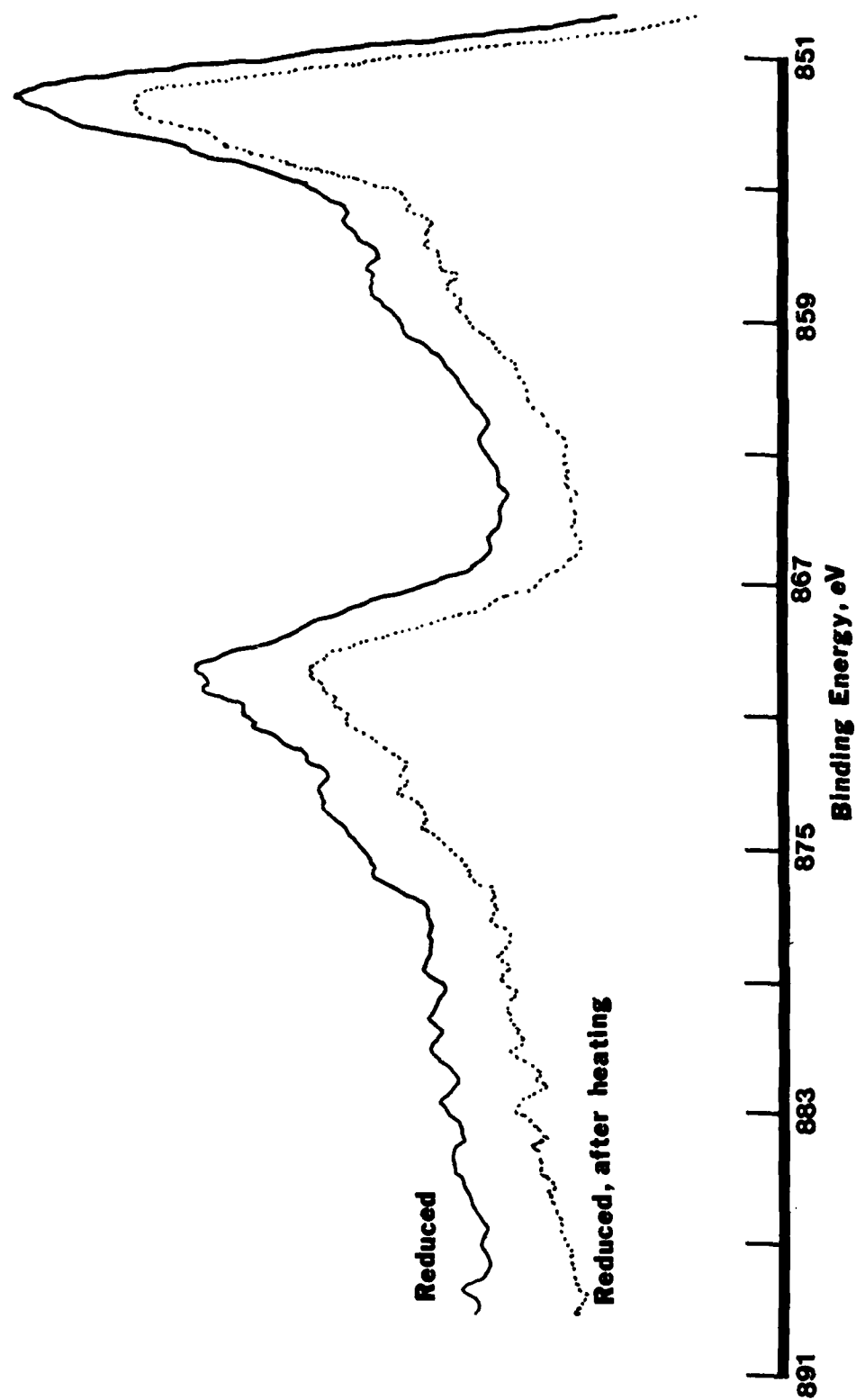
Binding Energy, eV

891 883 875 867 859 851
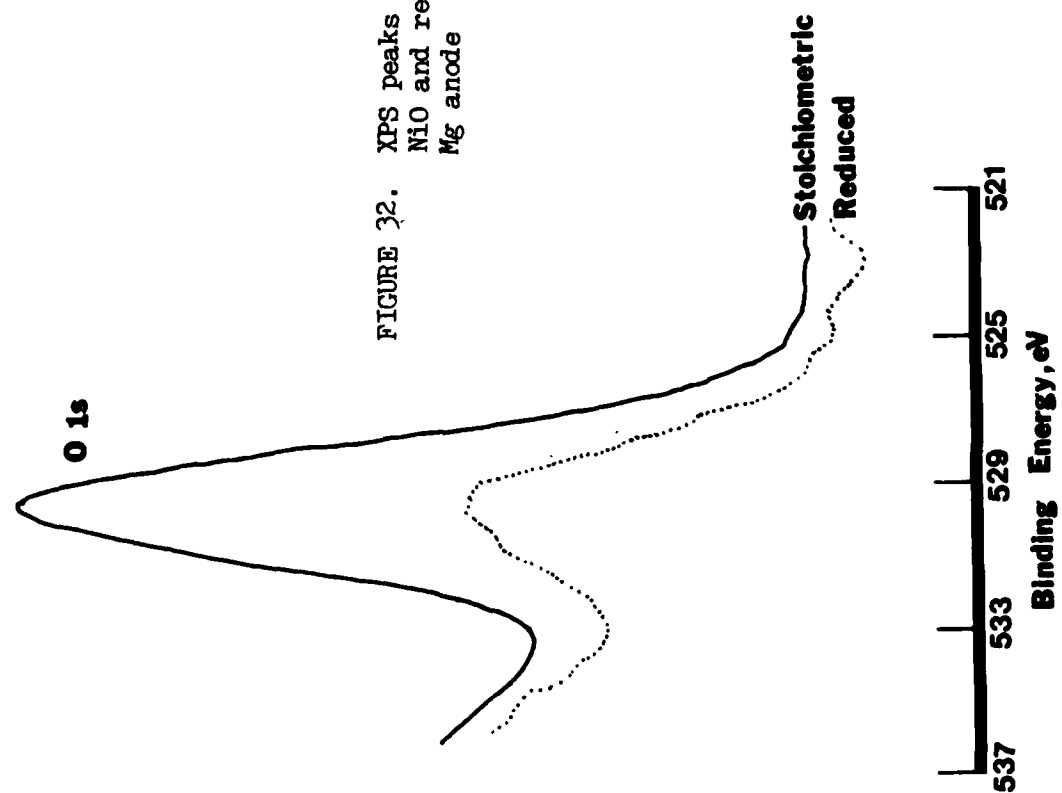
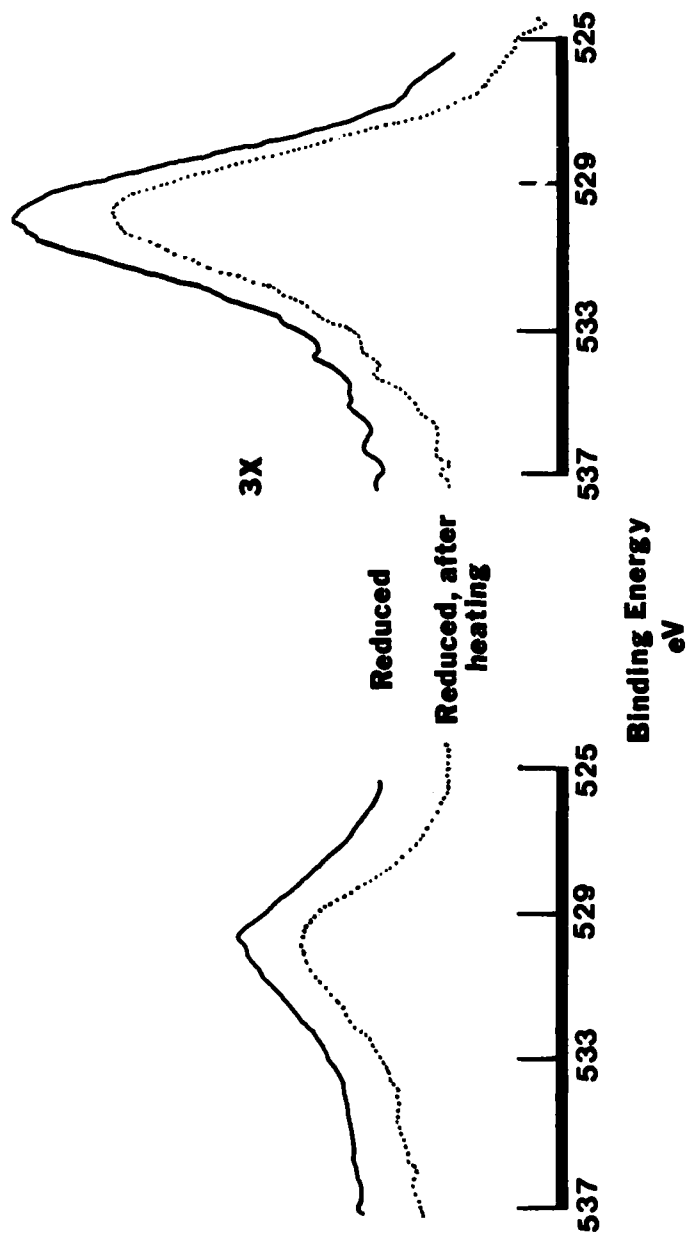FIGURE 33. Ni 2p spectral region for reduced NiO before and after heating, Al anode

FIGURE 34. O 1s spectral region for reduced NiO before and after
heating, Al anode

reduced sample, indicating that hydroxyls, if they form, are only present in low, undetectable levels. The Ni/O peak intensity ratios for AES are also the same.

The Ni 2p XPS spectral region gives additional information about what is happening during the reduction process. Upon comparing Figures 9 and 11, one notices the presence of "shake-up" satellite peaks immediately to the left (at a higher binding energy) of the Ni $2p_{1/2}$ and Ni $2p_{3/2}$ peaks for the stoichiometric NiO and the greatly reduced intensity of these satellite peaks for the reduced NiO. As discussed by Matienzo et.al. (14), these satellite peaks are indicative of paramagnetic species such as NiO, but are not present for diamagnetic species such as Ni. The theory behind satellite peaks is discussed in the XPS THEORY section of this thesis.

LEED data. Figure 35 shows the LEED patterns for reduced NiO (100) at 66 eV and 91 eV. The basic LEED pattern is unchanged in symmetry, lattice spacing, and background intensity from that seen for the stoichiometric NiO (100) surface shown in Figure 14. The key point from the LEED data is that the patterns are the same. This indicates that the arrangement of the reduced nickel atoms must be the same as in the stoichiometric lattice and that the location of the actual reduced atoms is random.

Depth profile of a reduced sample. A reduced sample was depth profiled by argon ion bombardment to determine the extent of the reduction into the sample. A depth profile of a sample is made by sputtering away layers of atoms and analyzing the surface at various times during the sputtering process. The argon ion sputtering was

(a) 66 eV

FIGURE 35. Photographs of LEED
pattern for reduced
NiO (100)

(b) 91 eV
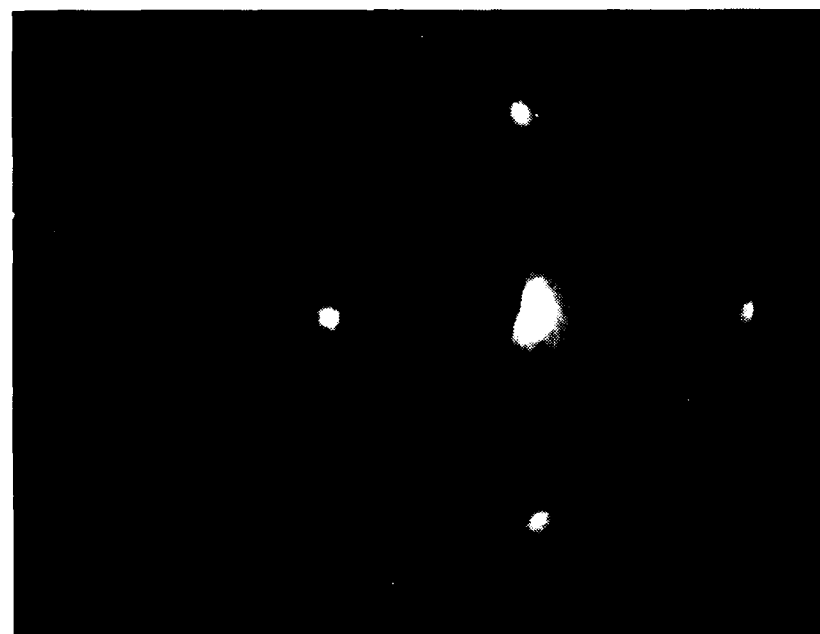
carried out at 5×10^{-5} Torr pressure of argon in the chamber, with an Ar^+ beam current of 14 microamps/cm^2 at the sample. Figure 36 illustrates how the surface concentration of oxygen changed as the surface was sputtered away. In Figure 36, it is shown that during reduction, vacancies in the Ni-O surface lattice occur at oxygen sites only. This was proven by LEED, which showed no background to indicate disorder and no new pattern, so the Ni must stay the same. Therefore, the C_{Ni} is always 0.50 and the sum of the oxygen sites and oxygen-vacant sites is also 0.50. With that definition, $C_O = 0.50$ for the stoichiometric NiO, as indicated by the dashed line in Figure 36. These data indicate that the reduction is three-dimensional; that is, not only the top layer of NiO molecules is being reduced, but subsequent layers as well. The oxygen concentration, as shown in Figure 36, is nearly constant through the first 16 $\overset{o}{A}$ of sputtering. Between 16 $\overset{o}{A}$ and 125 $\overset{o}{A}$, the concentration of oxygen varies linearly with the depth sputtered, then exponentially tails off. Stoichiometric NiO was reached between 375 and 450 $\overset{o}{A}$, after which no change was observed with further sputtering.

Figure 37 shows the AES for the reduced sample before ion bombardment began and after bombardment was completed. The Auger spectrum for the sputtered surface appears nearly the same as that for stoichiometric NiO. In Figure 37, the oxygen Auger peak increases greatly relative to the nickel peaks. In addition, the second nickel peak intensity has decreased.

Figures 38 and 39 show the Ni 2p and O 1s XPS spectral regions before and after sputtering. In Figure 33, the shake-up satellites
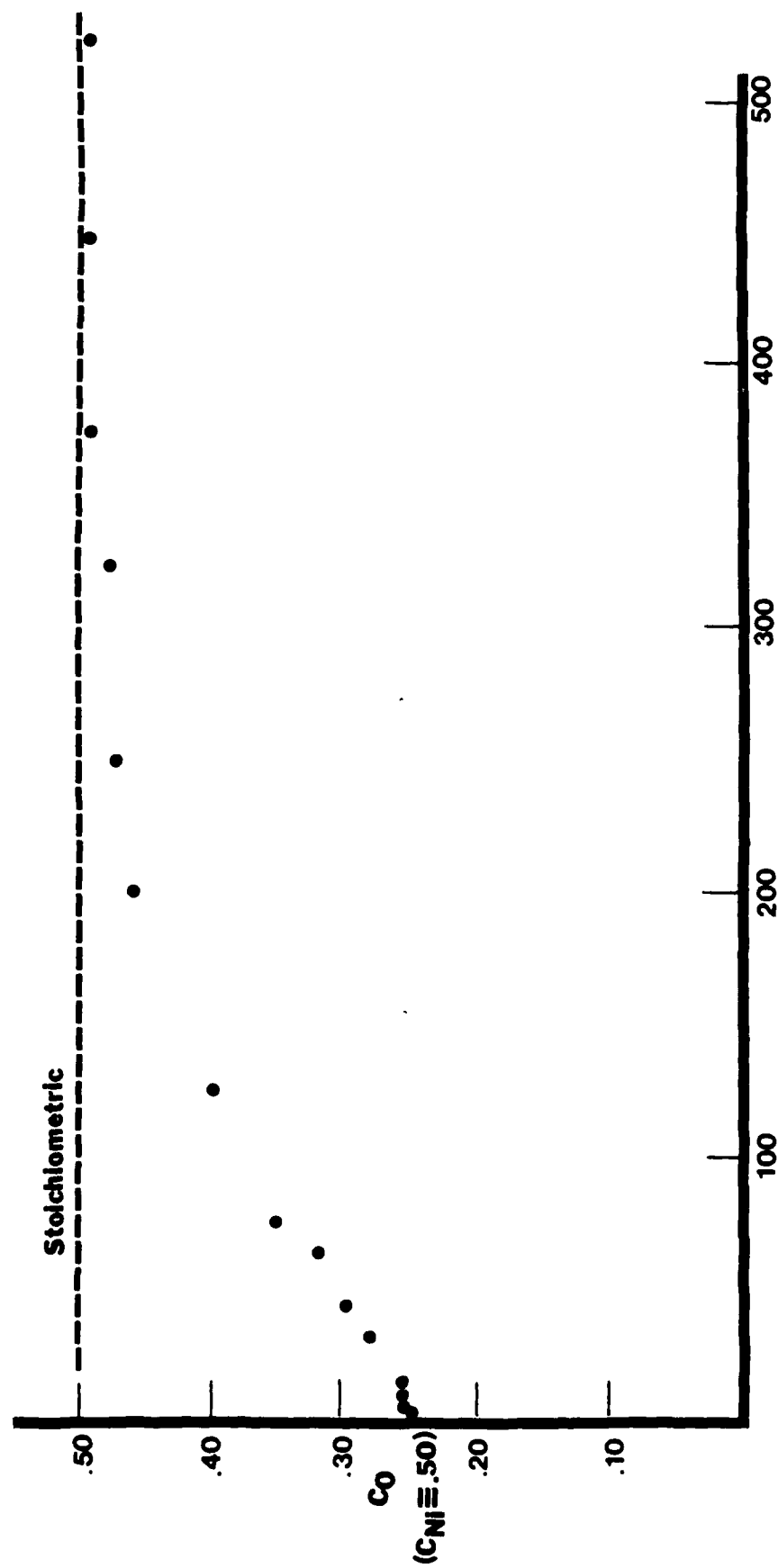
FIGURE 36. Depth profile of reduced NiO
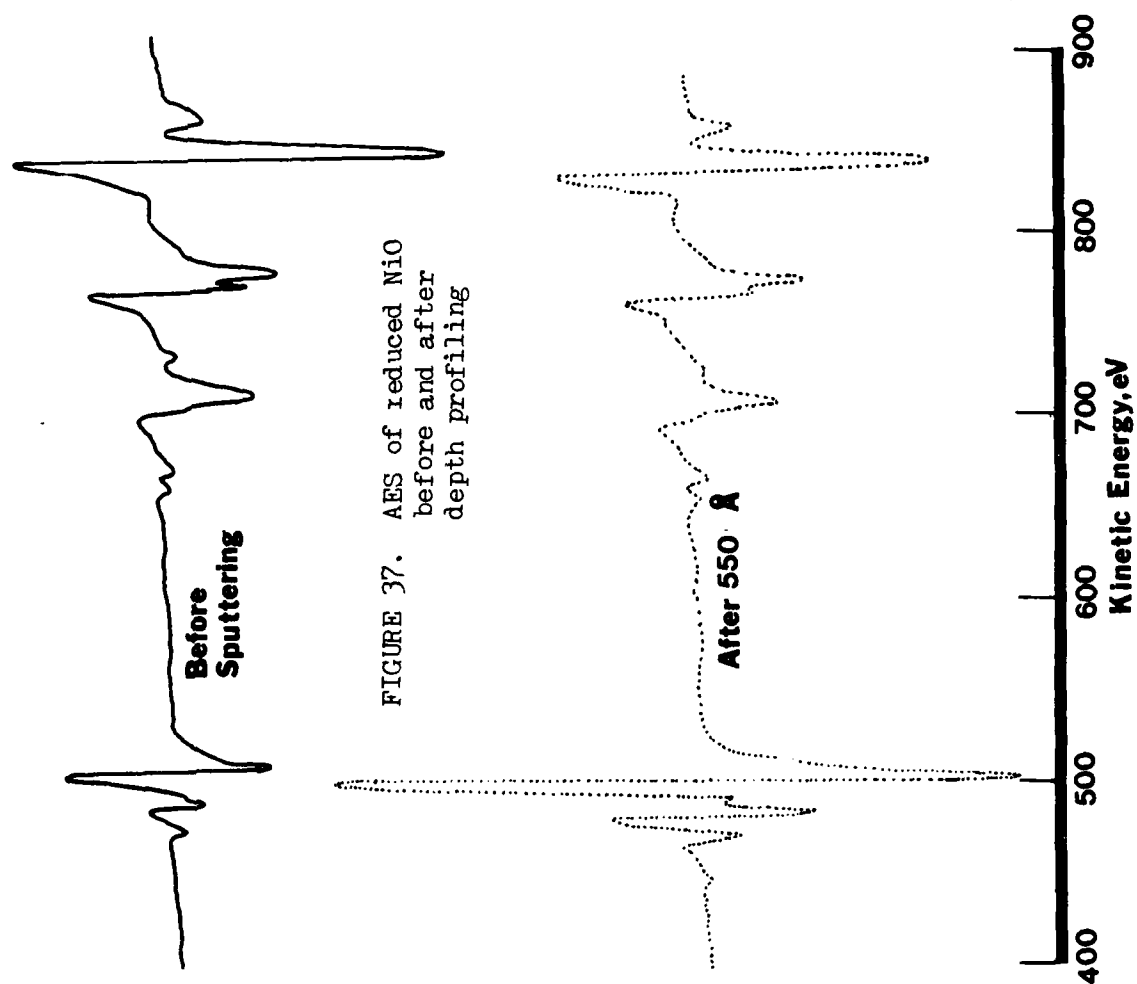
Before Sputtering

After 550 Å

Kinetic Energy, eV

FIGURE 37. AES of reduced NiO before and after depth profiling
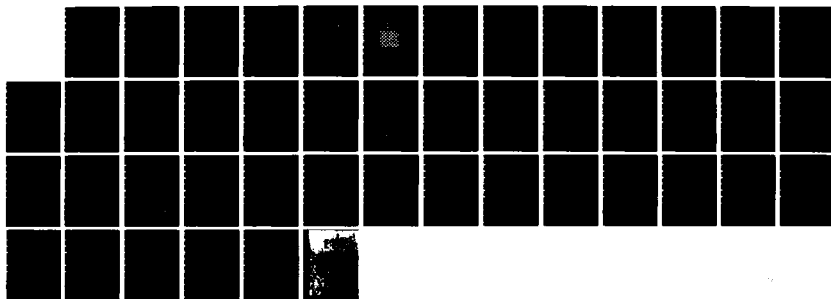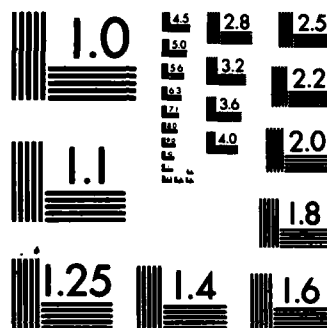
MICROCOPY RESOLUTION TEST CHART
NATIONAL BUREAU OF STANDARDS-1963 A
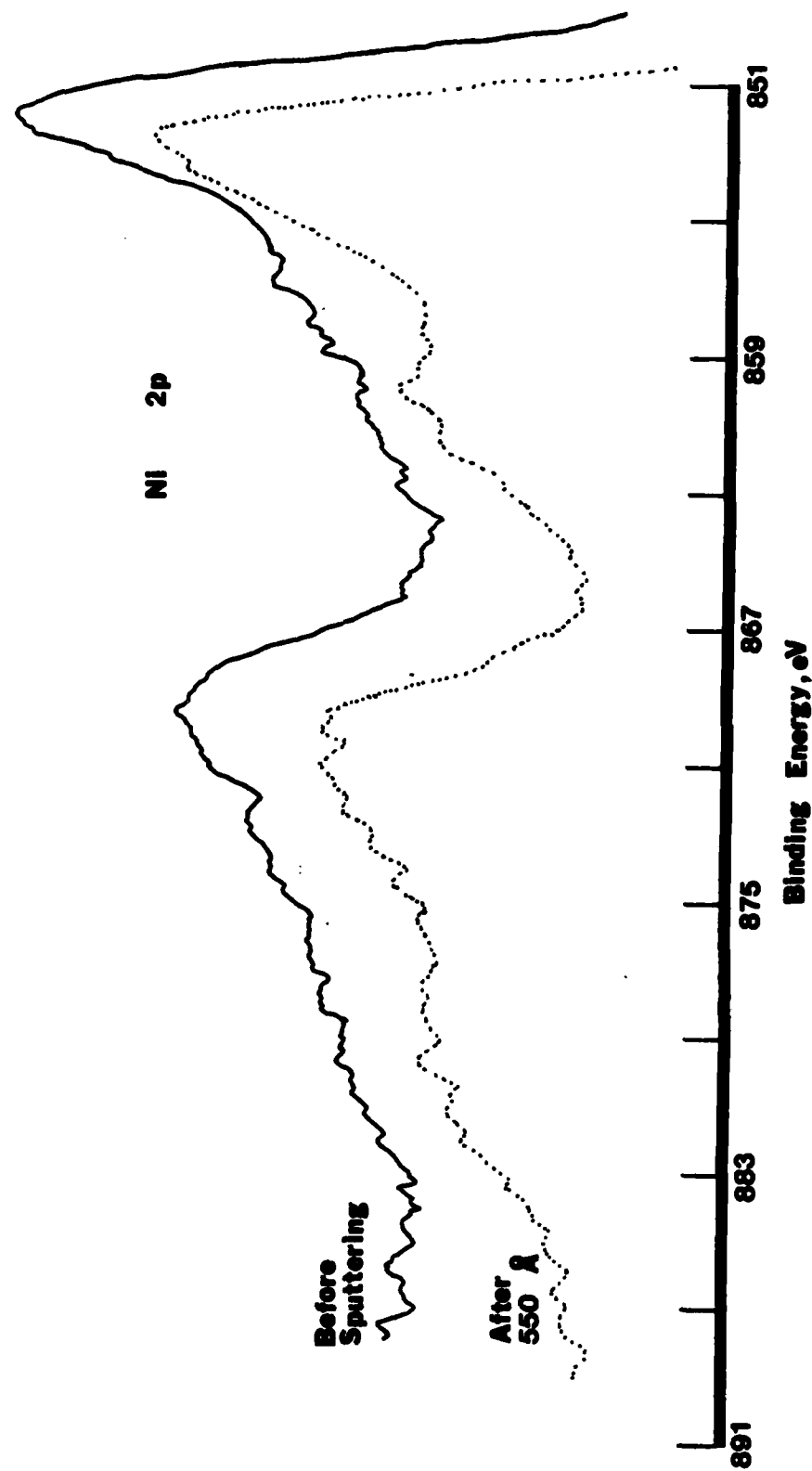
FIGURE 38. Ni 2p spectral region for reduced NiO before and after depth profiling, Al anode
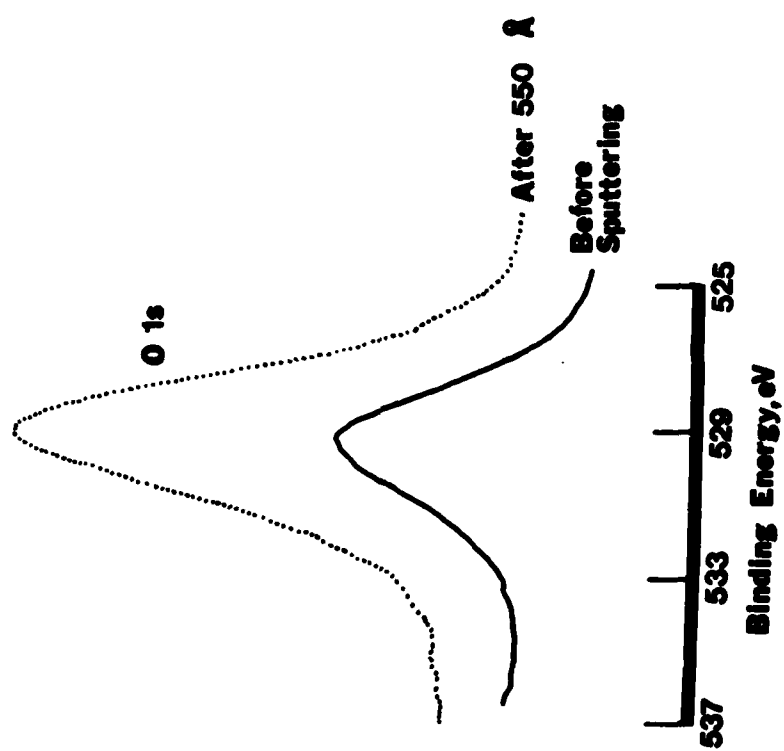
FIGURE 39. O 1s spectral region for reduced NiO before and
after depth profiling, Al anode

return to the Ni 2p region after a reduced sample is sputtered, though not with the intensity of a stoichiometric sample. It is not surprising that the intensity would be less, since when a stoichiometric sample is prepared, the sputter-cleaned crystal is annealed in oxygen, which would eliminate oxygen and nickel lattice defects. It is also known that Ar^+ causes preferential sputtering of oxygen (32). In addition, the distance between the Ni 2p peaks has increased slightly (see Table II). Upon examining Figure 39, only the single, symmetric O 1s peak is present after sputtering.

Reduced surface structure model. Similar to the stoichiometric calculations, the Auger layer model combined with the depth profile data of Figure 36 can be used to determine a structure for the surface of the reduced NiO. LEED measurements showed that $C_{Ni}= 0.50$ on all layers of a reduced surface, while C_O increases as shown in Figure 36. The oxygens must be randomly removed to explain the LEED. Since the stoichiometric NiO (100) has an oxygen overlayer at bulk termination, the reduced should have also, but with fewer oxygens. Using this model with the observed Ni/O peak ratio of 0.96, the top layer of the reduced surface has $C_{Ni}= 0.50$, $C_O= 0.33$, and $C_{vacancies}= 0.17$, with an overlayer of oxygens which covers 66% of the nickel sites. A top view of a section of this reduced surface is shown in Figure 40. The basic NiO lattice structure remains intact for this reduced surface, giving identical LEED patterns before and after reduction. The model for the reduced surface will prove useful in explaining the results of the adsorption of ethylene on reduced NiO (100).

TABLE II. XPS Data for the Reduction of NiO (100)

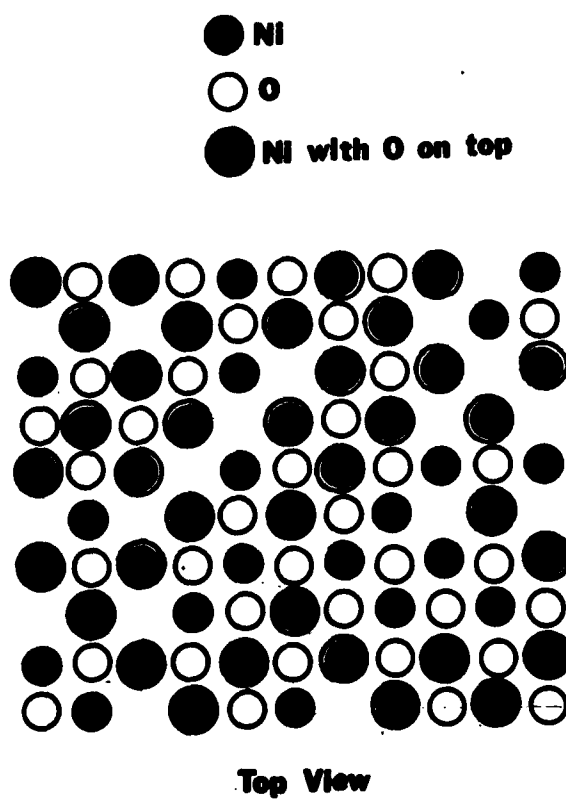| State of NiO	Ni $2p_{1/2}$	Ni $2p_{3/2}$	Δ	O 1s	$\frac{Ni}{O}$ Auger	Figure Number
Stoichiometric	872.4	854.5	17.9	529.4	0.48	8,9
Reduced	872.1	852.2	17.9	529.4	1.20	10,11
Reduced	869.5	852.1	17.4	529.4	3.20	32,33
Reduced, after heating at 500K for 35 minutes	869.7	852.3	17.4	529.4	3.04	32,33
Reduced	869.5	852.0	17.5	529.4	2.13	38,39
Reduced, after sputtering	870.5	852.7	17.8	529.4	0.55	38,39

● NI
○ O
● NI with O on top

Top View

FIGURE 40. Structure for the surface
of reduced NiO (100)

It could also be argued that the top layer oxygens are less stable due to having only one nickel bond and thus would be removed before any lattice oxygens during the reduction process. However, this top layer of oxygens is indistinguishable from the lattice oxygens with the experimental methods used. The oxygen atoms are very mobile during the reduction process. The model for stoichiometric NiO (100) also indicates that oxygens do exist on the top layer. Since a random removal of oxygens is evident in the LEED and the model for the stoichiometric NiO has a top layer of oxygens, this top layer is assumed to deplete randomly as do the other layers, with no consideration for the number of oxygen-to-nickel bonds the oxygen atom may have. Therefore, the previously proposed model for the reduced surface was adopted.

Mechanism for the reduction process. Two mechanisms seem likely based on the temperature and pressure behavior and can be proposed for the reduction process. The H_2 adsorption is flux limited and the limiting step of the reduction process. In one mechanism, a hydrogen molecule dissociates at a nickel atom site. On H atom migrates to a lattice oxygen while the other stays at the nickel site. The nickel hydrogen then combines with the formed OH and is desorbed as H_2O. This mechanism is shown below:

$$
\begin{array}{ccc}
\overset{\nearrow H_2}{\text{Ni-O-Ni-O-Ni}} & \xrightarrow{\text{slow}} & \overset{\nearrow H-H}{\text{Ni-O-Ni-O-Ni}} \\
& & \Big\downarrow \text{fast} \\
H_2O \text{ (g) + Ni-O-Ni-}\square\text{-Ni} & \xleftarrow{\text{fast}} & \overset{H\ H}{\text{Ni-O-Ni-O-Ni}}
\end{array}
$$
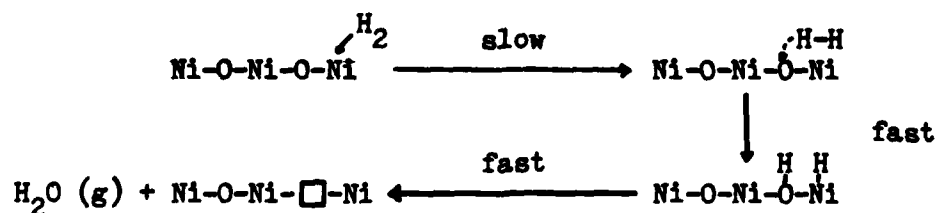
The reaction $H_2 \longrightarrow 2H_{ads}$ is known to occur for most metals and certainly for Ni, so it is expected that dissociation occurs upon adsorption.

In the second mechanism, the hydrogen is again adsorbed and dissociated at a nickel site. In this case, however, an H atom migrates to a top site lattice oxygen with the resulting OH combining with the other H atom from the nickel:
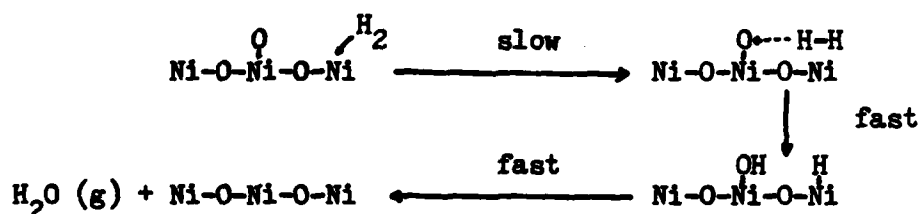
In both of the above mechanisms, a small steady state OH concentration develops which is too small to be observed by XPS. The mechanism has to have H very mobile or OH and H very closely situated. From the data of this thesis, it is impossible to say which mechanism is occurring sonce fast steps occur after the slow step of H_2 adsorption and steady state concentrations of OH cannot be observed by AES. If both types of oxygen are present, however, both mechanisms could occur.

If, during the reduction process of NiO (100), one oxygen atom is lost per adsorbed H_2, the H_2 has a very low sticking coefficient (0.0001 ± 0.00005) at $350^\circ C$ and 1.3×10^{-6} Torr pressure of H_2, and even lower at lower temperatures. At lower temperatures, the reduction reaction is slowing down, with Ni sites for adsorption not becoming available as quickly.

THE ADSORPTION OF ETHYLENE ON NiO AND REDUCED NiO

The purpose of this portion of this thesis work was to investigate the gas adsorption properties of NiO with ethylene and to determine methods of activating stoichiometric NiO to ethylene gas adsorption. Although references could be found documenting the study of ethylene adsorption on nickel metal (these will be discussed in the COMPARISONS WITH OTHER DATA section), no information could be found regarding the adsorption of ethylene on nickel oxide. The only surface sensitive gas adsorption studies involved CO and NO on powdered NiO (33). These too will be discussed later.

The adsorption of ethylene was studied on stoichiometric and reduced NiO (100) at 5×10^{-7} Torr and at 200K, 300K, and 500K. The adsorption processes were followed for 70 minutes. The atomic concentrations of nickel and oxygen, and the coverage of carbon were monitored using AES as a function of ethylene exposure. XPS was used to monitor the Ni 2p, O 1s and C 1s spectral regions. In addition, LEED was used to monitor changes in the surface diffraction patterns.

Adsorption of ethylene on stoichiometric NiO (100). No adsorption of ethylene on the stoichiometric NiO was observed at 300K or 500K within the detection limit (approximately 0.005 monolayers, ML, for carbon) of AES, even after 2100 L exposure to ethylene. As can be seen in Figure 41, there is no indication of any Auger carbon peak for the stoichiometric NiO at 300K or 500K. After the sample was cooled to 200K, however, ethylene was observed on
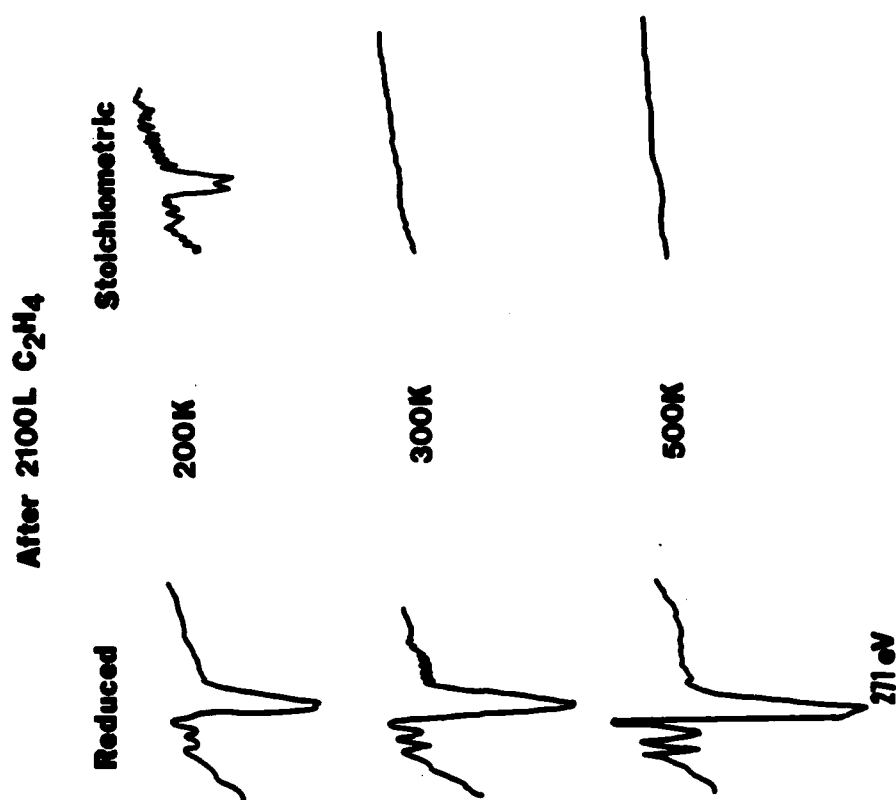
FIGURE 41. Carbon AES peaks for reduced and stoichiometric NiO after 2100 L ethylene exposure

the surface after exposure to ethylene by the appearance of a
carbon peak at 271 eV on the AES spectrum (see Figure 41). As
shown in Figure 42, the carbon coverage saturates at 0.07 ML while
the atomic concentrations of nickel and oxygen remain constant.
As expected, then, the concentration of nickel relative to oxygen
(c_{Ni}/c_O) also remains relatively constant, as illustrated in
Figure 43. After the sample is warmed, the Auger carbon peak is
lost at 270K without any change in the NiO (100).

When examining the XPS, no changes are seen in the O 1s
or Ni 2p peak locations or intensities (see Table III). After
2100 L exposure to ethylene, the O 1s peak at 529.4 eV retains its
symmetry, indicative of only the stoichiometric NiO oxygen being
present (see Figure 44a). The O 1s peak is still identical to
that of bare NiO (100). A small, broad peak in the C 1s region can
be seen after ethylene exposure in Figure 44b. The maximum of this
carbon peak appears to be at 282.6 eV, and the peak is very broad with
respect to its height. Like the O 1s peak, the Ni 2p peaks show no
changes upon ethylene exposure at 200K. The spectrum retains its
satellite peaks characteristic of the oxide, located at higher
binding energies than the Ni $2p_{1/2}$ and Ni $2p_{3/2}$ peaks. The peak
locations for these XPS spectra, as well as the remainder of those
discussed in this section, are summarized in Table III.

The LEED data show no additional diffraction spots from
those in stoichiometric NiO (see Figure 14) upon exposure to
ethylene at 200K. However, the background intensity does increase
slightly, wh'ch is i- icative of disorder at the surface.
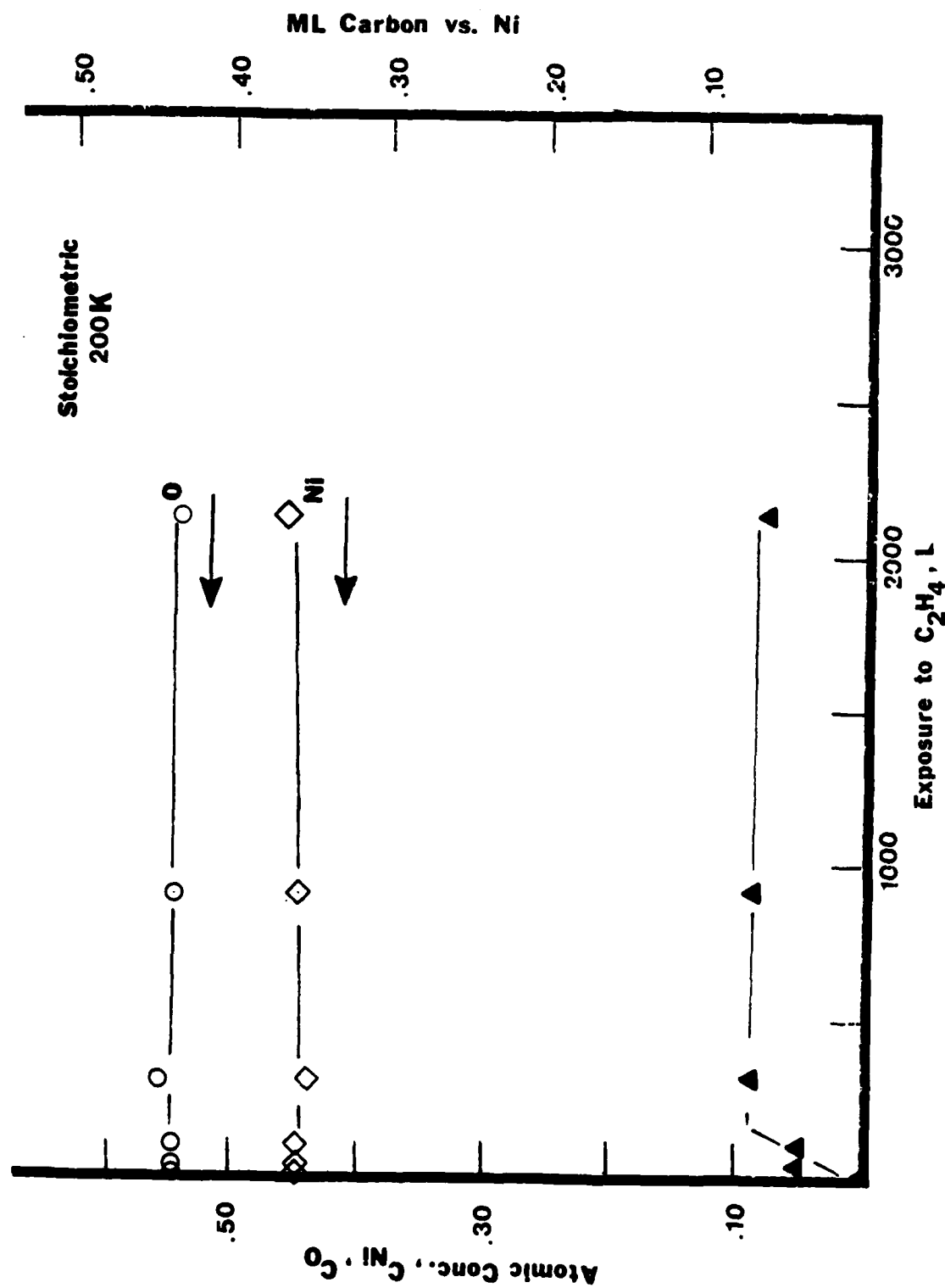
FIGURE 12. Ethylene chemisorption on stoichiometric NiO (100) at 200K
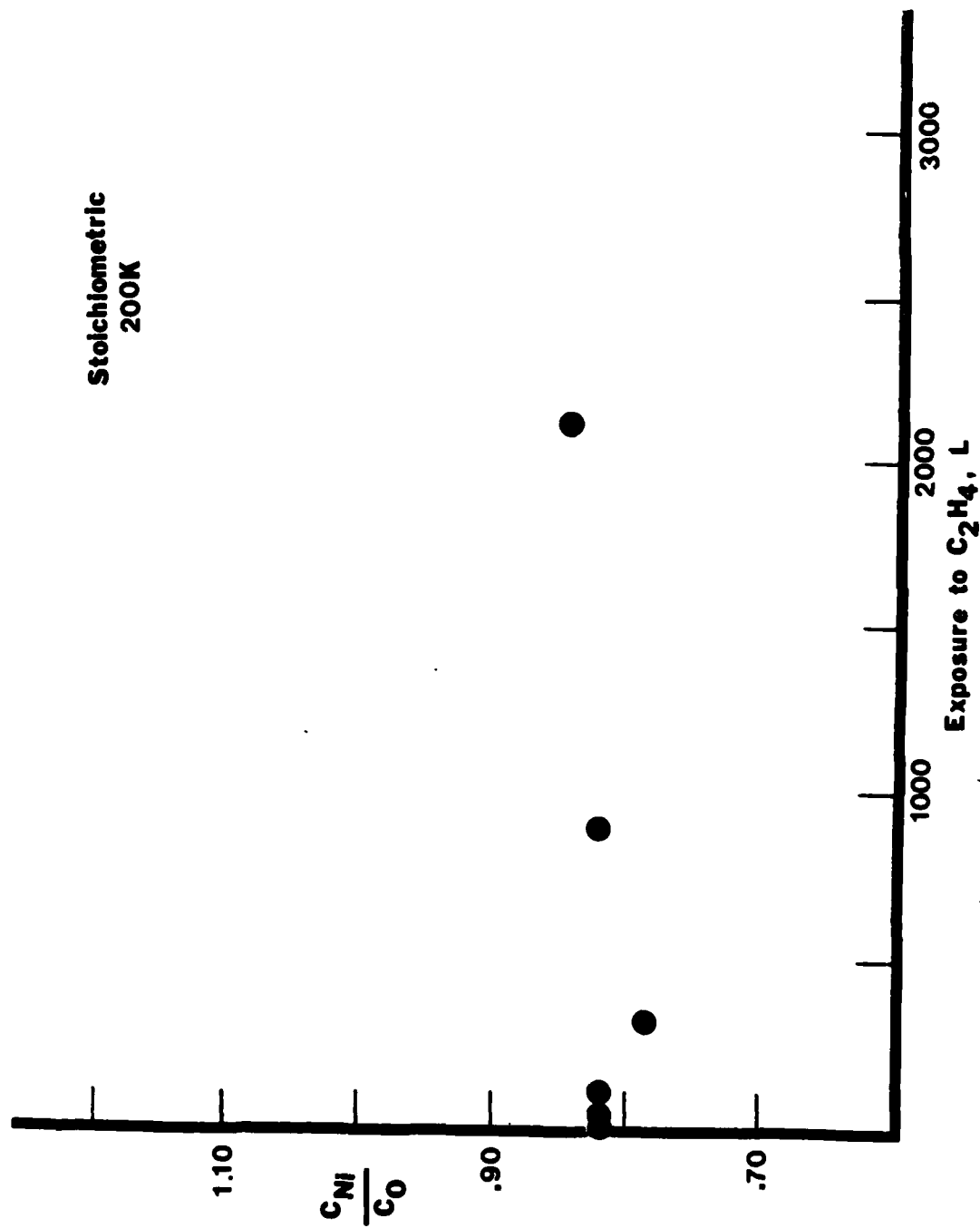
FIGURE 43. c_{Ni}/c_0 as a function of ethylene exposure for stoichiometric NiO (100) at 200K

TABLE III. XPS Data for the Adsorption of Ethylene on NiO (100)
(Binding Energies in eV)

State of NiO	Temp.	Ni $2p_{1/2}$	Ni $2p_{3/2}$	Δ	O 1s	C 1s
Stoichiometric	200K	871.8	854.2	17.6	529.4	
Stoichiometric with 2100 L ethylene	200K	871.9	854.3	17.6	529.4	282.6
Reduced	200K	869.6	852.0	17.6	529.4	
Reduced w/2100L ethylene	200K	869.5	852.0	17.5	529.4	284.1
Reduced	300K	869.9	852.2	17.7	529.4	
Reduced w/2100L ethylene	300K	869.8	852.4	17.4	529.5	283.5
Reduced	500K	869.6	852.0	17.6	529.4	
Reduced w/2100L ethylene	500K	869.0	851.8	17.2	529.4	282.6

FIGURE 44. O 1s and C 1s XPS spectral regions for stoichiometric
NiO (100) at 200K before and after 2100 L
ethylene, Al anode

FIGURE 45.   Ni 2p XPS spectral region for stoichiometric
NiO (100) at 200K before and after 2100 L ethylene,
Al anode

From the Auger, XPS, and LEED data, it is apparent that at 200K on the stoichiometric NiO (100) surface, the ethylene is randomly chemisorbed with no "preference" for adsorption on either nickel or oxygen atoms. As indicated by t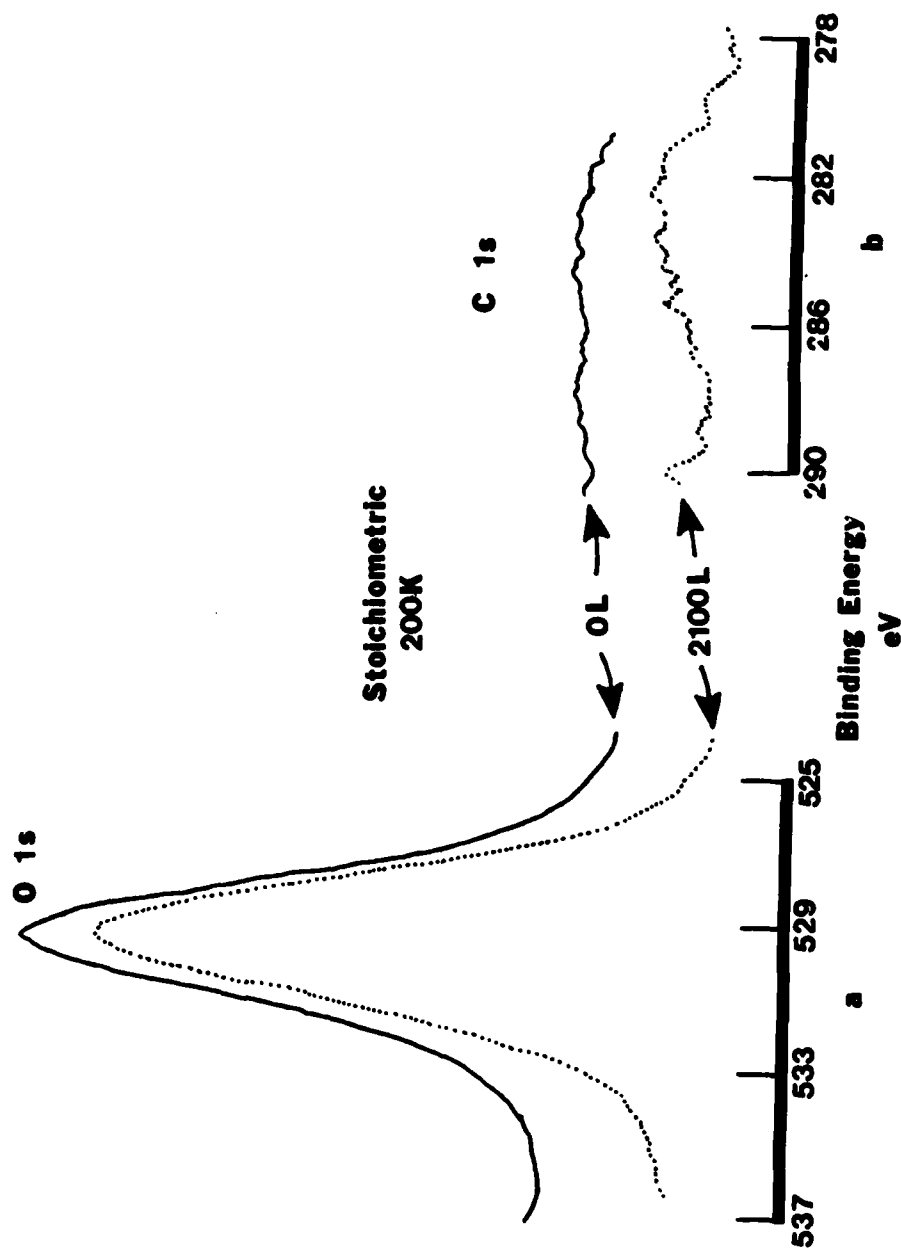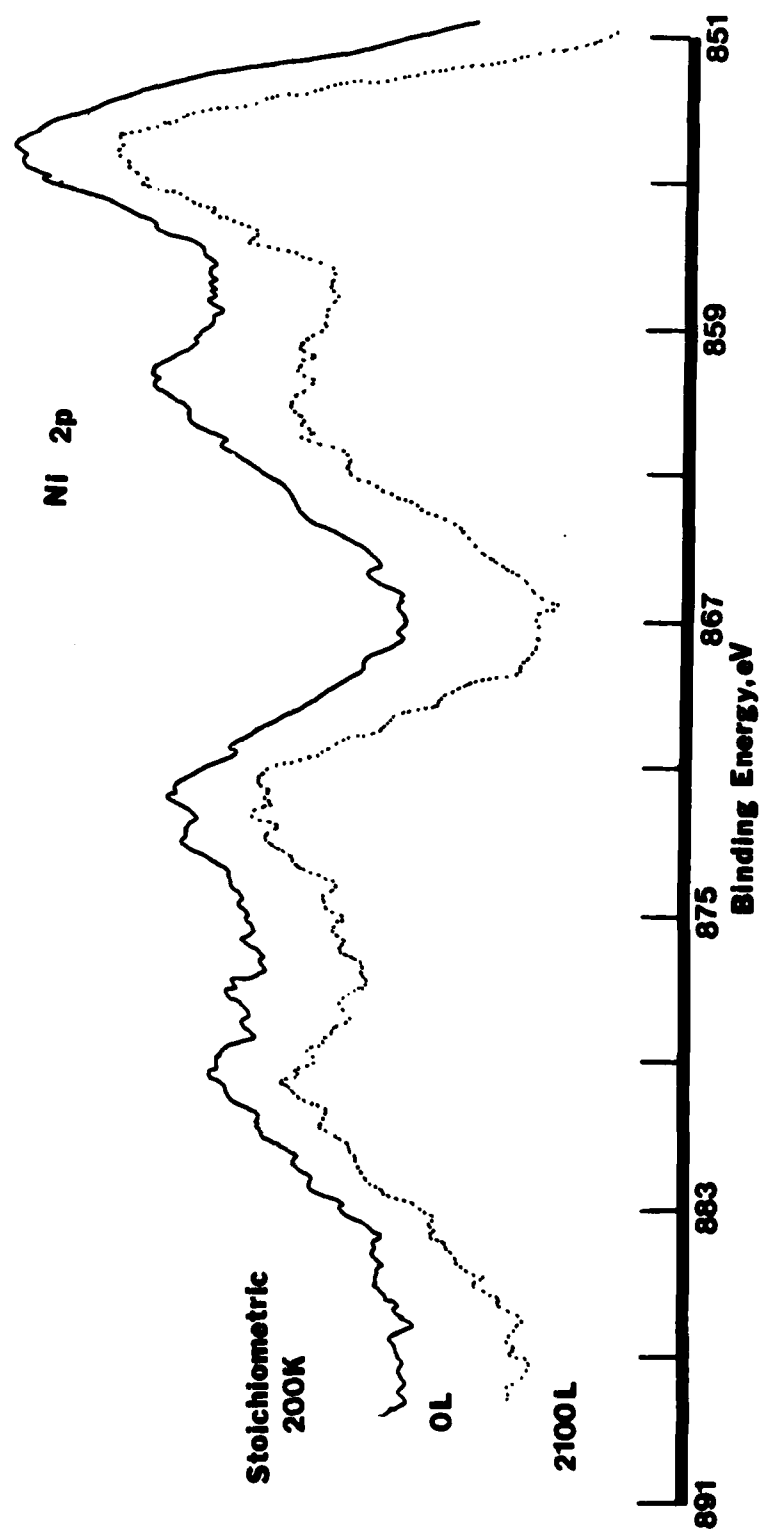he XPS data, there are no changes to the chemical environments of either the oxygen or nickel. The C_{Ni} and C_O remained constant. In combination with the constant C_{Ni}/C_O ratio with coverage, the XPS data indicate that there are no chemical reactions taking place between the NiO and ethylene which change the stoichiometric NiO. If the ethylene is dissociating upon adsorption, it is not deducible from this data.

Adsorption of ethylene on reduced NiO at 200K. At 200K, the behavior of the reduced surface is similar to that of the stoichiometric surface. The surface had previously been reduced to approximately 60% of the original oxygen stoichiometry. If the model of Davis et.al. is used, which assumes a homogeneous distribution of nickel and oxygen throughout the Auger sampling depth, the relative concentrations of nickel and oxygen are C_{Ni}= 0.66 and C_O = 0.34. If the Auger depth profile model is applied with the data of Figure 36, the relative surface concentrations are C_{Ni}= 0.60 and C_O= 0.40. As seen for the stoichiometric NiO at 200K, there ' - a rapid initial rise in carbon coverage on the reduced   + 200K (see Figure 46). This initial coverage saturates   oximately 45 L and is followed by a much slower adsorption rate through 2100 L exposure. After 2100 L exposure, the carbon coverage is 0.14 ML. The carbon Auger peak for the reduced NiO at 200K in Figure 41 has the structure of a
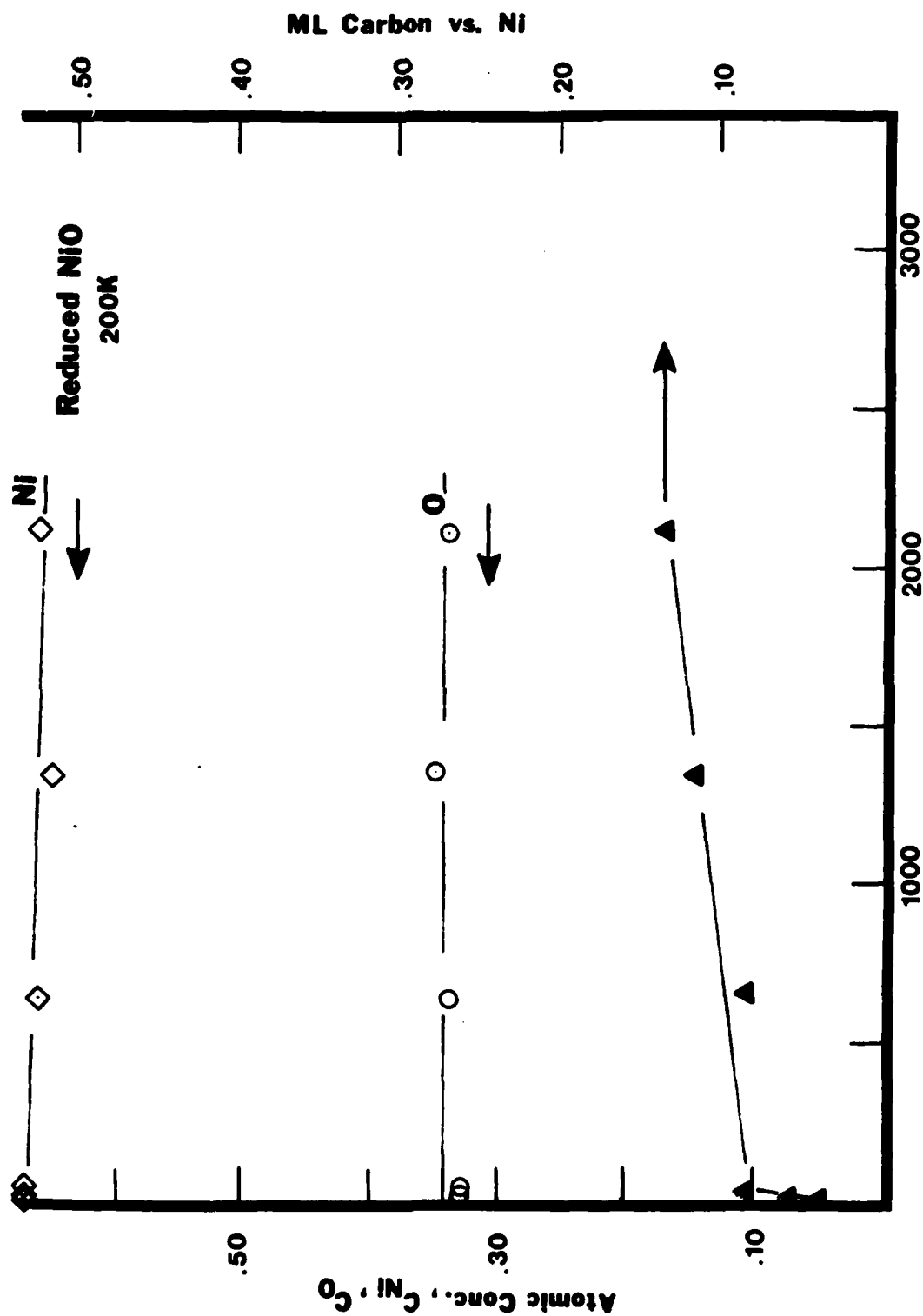
FIGURE 46. Ethylene chemisorption on reduced NiO (100) at 200K

carbidic, as opposed to a graphitic, carbon peak. There is a dip midway in the C_{Ni}/C_O ratio versus exposure plot of Figure 47. This indicates that the ethylene initially sits on nickel sites, while occupying oxygen sites later in the adsorption process.

In the XPS data of Figure 48a, no change from the reduced sample is visible in the O 1s peak after ethylene adsorption. A very small, broad carbon peak is seen in Figure 48b with maximum height at 284.1 eV after 2100 L exposure. No significant changes are noticable in the Ni 2p peaks in Figure 49 after ethylene exposure. Note, however, the decrease in intensity of the satellite peaks in both spectra as compared to Figure 45. Again, the Ni 2p XPS for the reduced surface more closely resembles spectra for nickel than for nickel oxide. The XPS peak locations are summarized in Table III.

The LEED data for the reduced sample at 200K show no diffraction pattern changes occurring. There were no apparent differences between the LEED patterns for the reduced sample before and after ethylene exposure.

The relatively constant C_{Ni} and C_O for the reduced surface with increasing ethylene exposure at 200K indicates that the surface is behaving similarly to the stoichiometric NiO at this temperature. However, the rapid rise followed by a gradual increase in carbon coverage indicates that a second adsorption stage is occurring which is not seen on the stoichiometric NiO. This second adsorption stage is most likely due to simple ethylene condensation on top of ethylene adsorbate already present on the surface. The second stage simply desorbs reversibly and does not saturate. It only occurs at low

FIGURE 47. C_{Ni}/C_O as a function of ethylene exposure for reduced NiO (100) at 200K
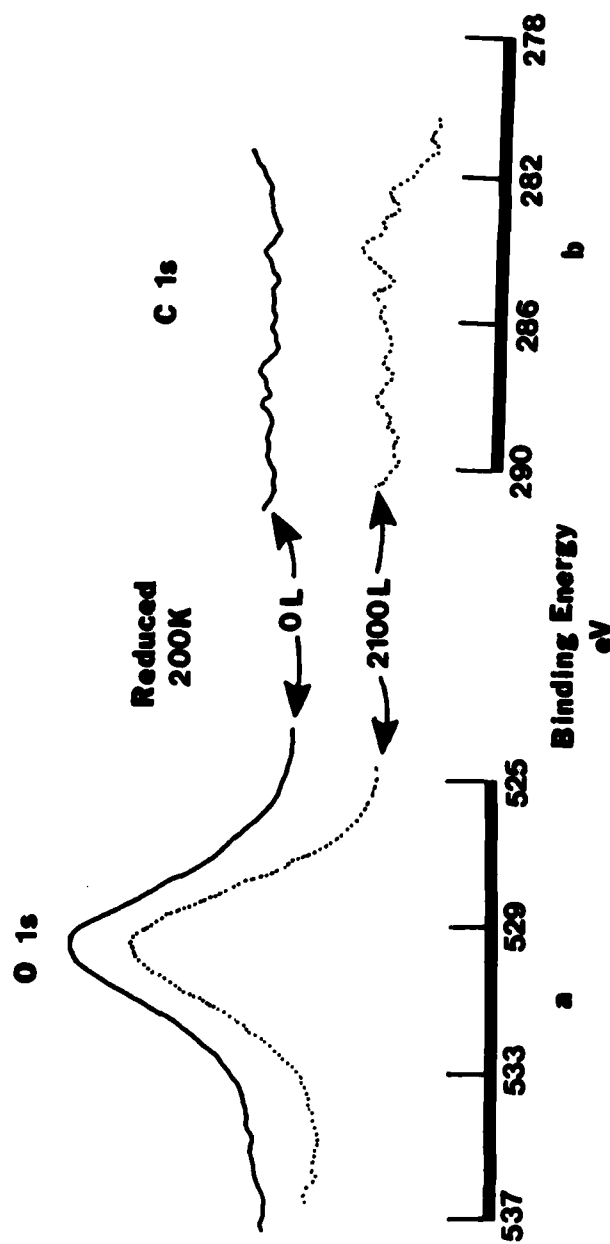
FIGURE 48. O 1s and C 1s XPS spectral regions for reduced NiO (100) at 200K before and after 2100 L ethylene, Al anode
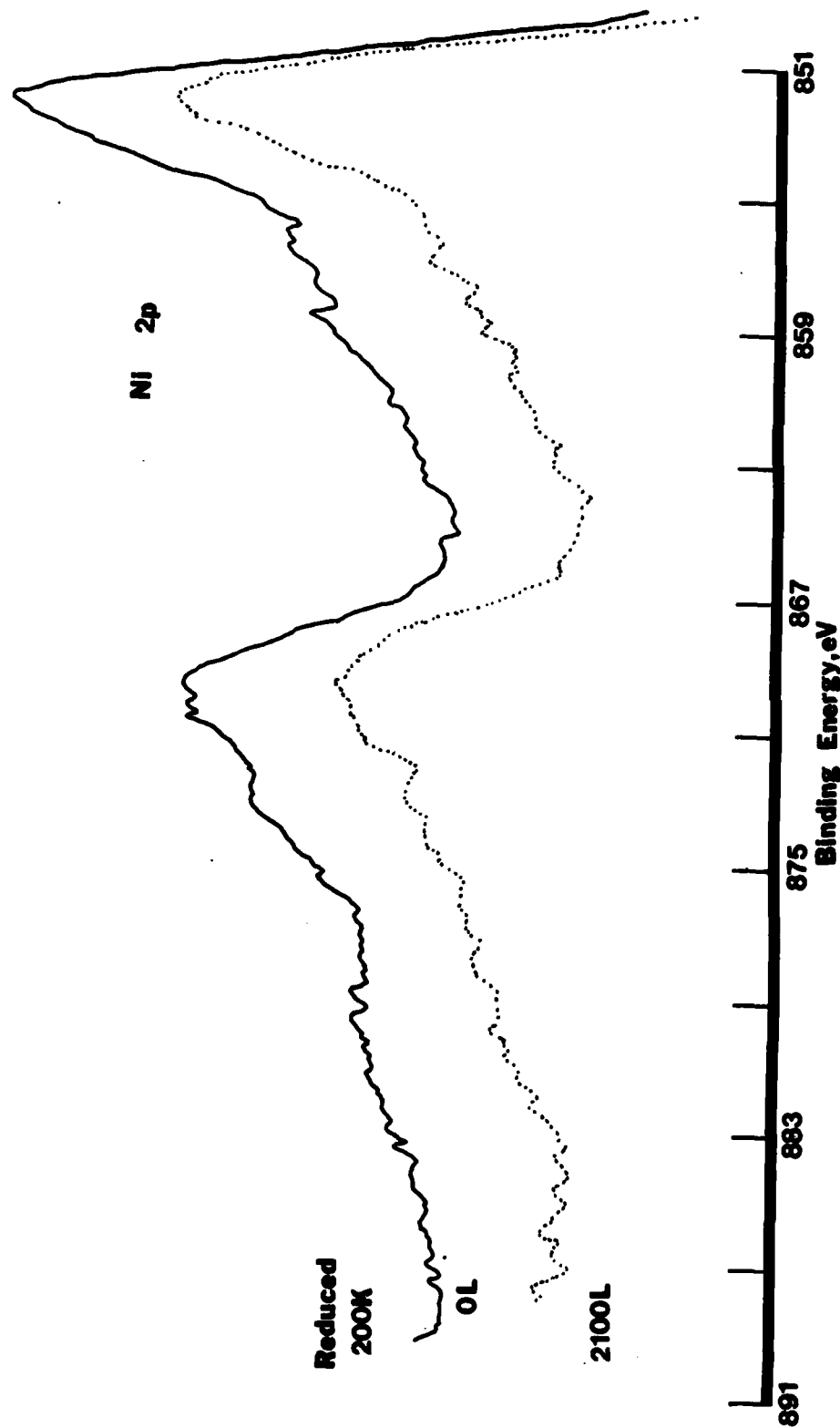
FIGURE 49. Ni 2p XPS spectral region for reduced NiO (100) at 200K before and after 2100 L ethylene, Al anode

temperatures and only if ethylene has already been adsorbed. The constant nature of the O 1s and Ni 2p spectra indicates no changes in the chemical environment of the oxygen and nickel present in the reduced NiO. The increase in carbon coverage (see Figure 46) for the reduced sample at 200K does indicate that the presence of more nickel on the surface relative to the oxygen enhances the ability of the surface to adsorb the ethylene.

Adsorption of ethylene on reduced NiO at 300K. On the reduced sample at 300K, the carbon coverage reaches near-saturation after 300 L exposure (see Figure 50). Only a single stage of adsorption is observed, with coverage saturating at 0.10 ML. Also in Figure 50, the relative C_O is increasing with exposure while the relative C_{Ni} is decreasing with exposure. Both level out at increasing exposures. This leads to the C_{Ni}/C_O ratio curve shown in Figure 51. The steepest portion of the curve in Figure 51 is during the first 300 L of exposure, which corresponds to the most rapid increase in carbon coverage in Figure 50. The decrease in C_{Ni} relative to the increase in C_O indicates that the ethylene prefers nickel adsorption sites to oxygen adsorption sites. The data also imply that no further reduction is taking place during ethylene exposure at this temperature. The Auger carbon peak after 2100 L exposure retains the carbide characteristics also seen at 200K (see Figure 41).

Figure 52a shows no significant change in the O 1s spectrum upon exposure. The symmetric O 1s is still like that for NiO. Again, the C 1s peak shown in Figure 52b is small and broad, with the peak maximum occurring at 283.5 eV. There are no apparent changes

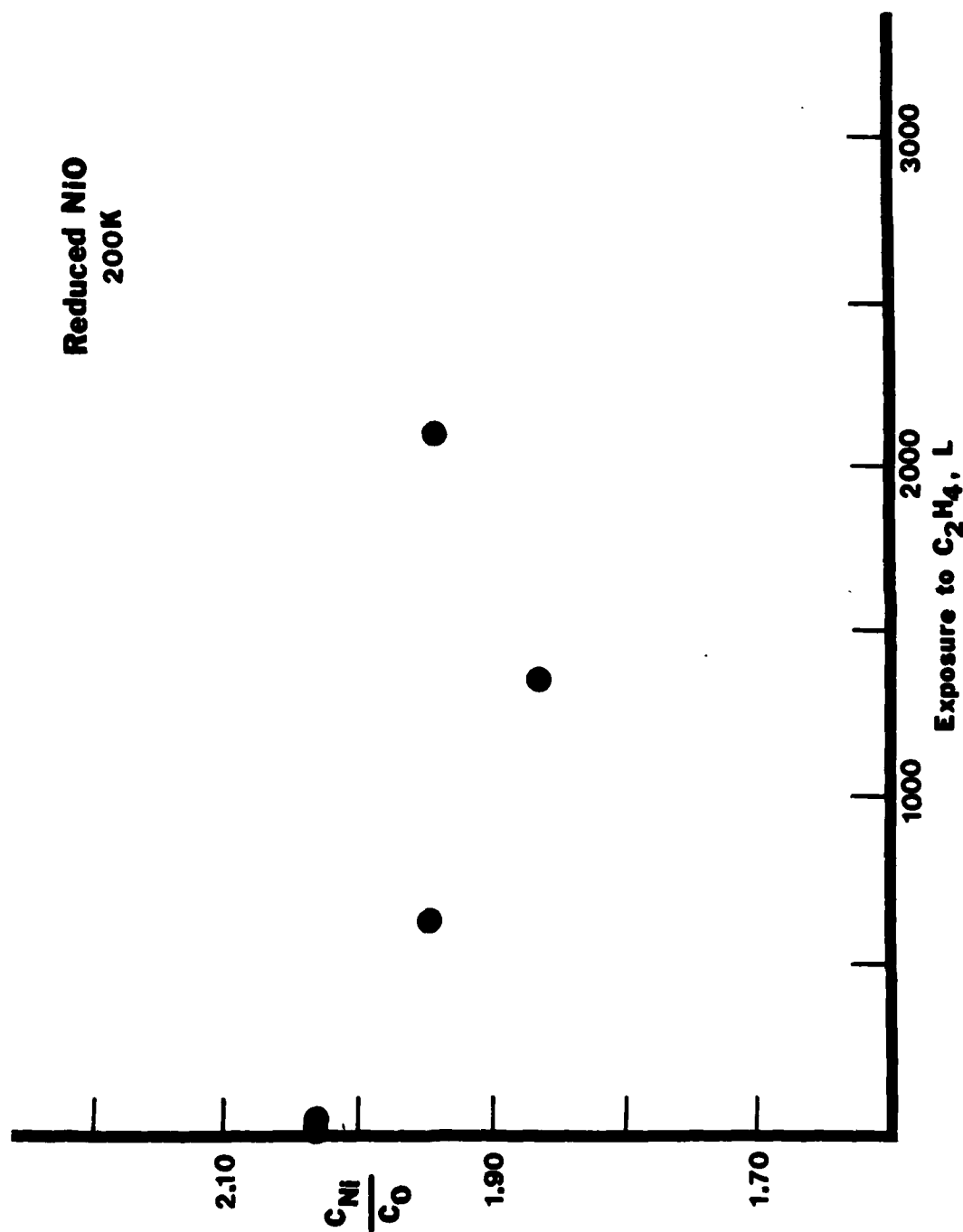FIGURE 50. Ethylene c emisorption on reduced NiO (100) at 300K

FIGURE 51. C_{Ni}/C_0 as a function of ethylene exposure for reduced NiO (100) at 300K

FIGURE 52. O 1s and C 1s XPS spectral regions for reduced NiO (100) at 300K before and after 2100 L ethylene, Al anode

in the Ni 2p peaks in Figure 53. The XPS peak locations are summarized in Table III. It was again the case with the LEED data that there were no differences in the diffraction pattern, indicating that the surface lattice structure is staying the same.

The data show that a somewhat different adsorption process is occurring on the reduced surface at 300K than at 200K. This difference is deduced from the trends of the Auger concentration and coverage data. However, the XPS data indicate that there is no change in the chemical environment of the Ni and O as a result of the ethylene adsorption. It cannot be concluded by XPS that the carbon species present at 300K are any different from those at 200K due to the poor resolution of the C 1s peak. However, a physisorbed layer does not form. The sticking coefficient and equilibrium concentration could be different at 300K than at 200K. The ethylene could be chemisorbing differently.

Adsorption of ethylene on reduced NiO at 500K. Quite different trends are seen in the data when the temperature of the reduced NiO is increased to 500K. From Figure 54, the rate of carbon coverage increases rapidly during the first 500 L of exposure to ethylene. After 500 L, the increase is slower, but saturation is not reached, even after 2100 L exposure. The relative C_{Ni} increases through 1350 L exposure then levels off, while the relative C_O decreases through 1350 L then levels off. The resultant C_{Ni}/C_O trend is shown in Figure 55 where a rapid increase in C_{Ni}/C_O is observed through 1350 L, then a leveling off. This increase in C_{Ni}/C_O ratio is similar to that observed in the hydrogen reduction study.

FIGURE 53. Ni 2p XPS spectral region for reduced NiO (100)
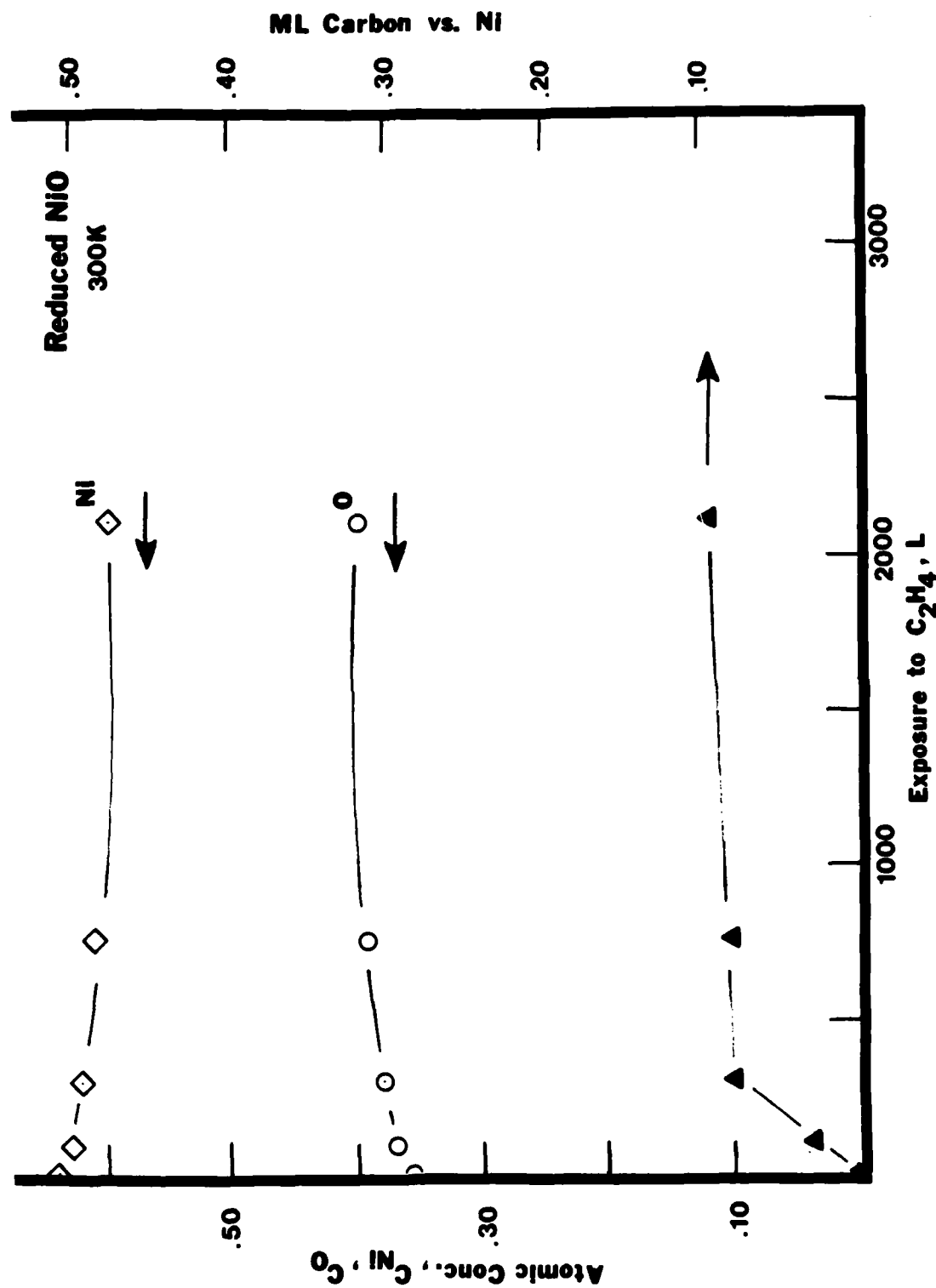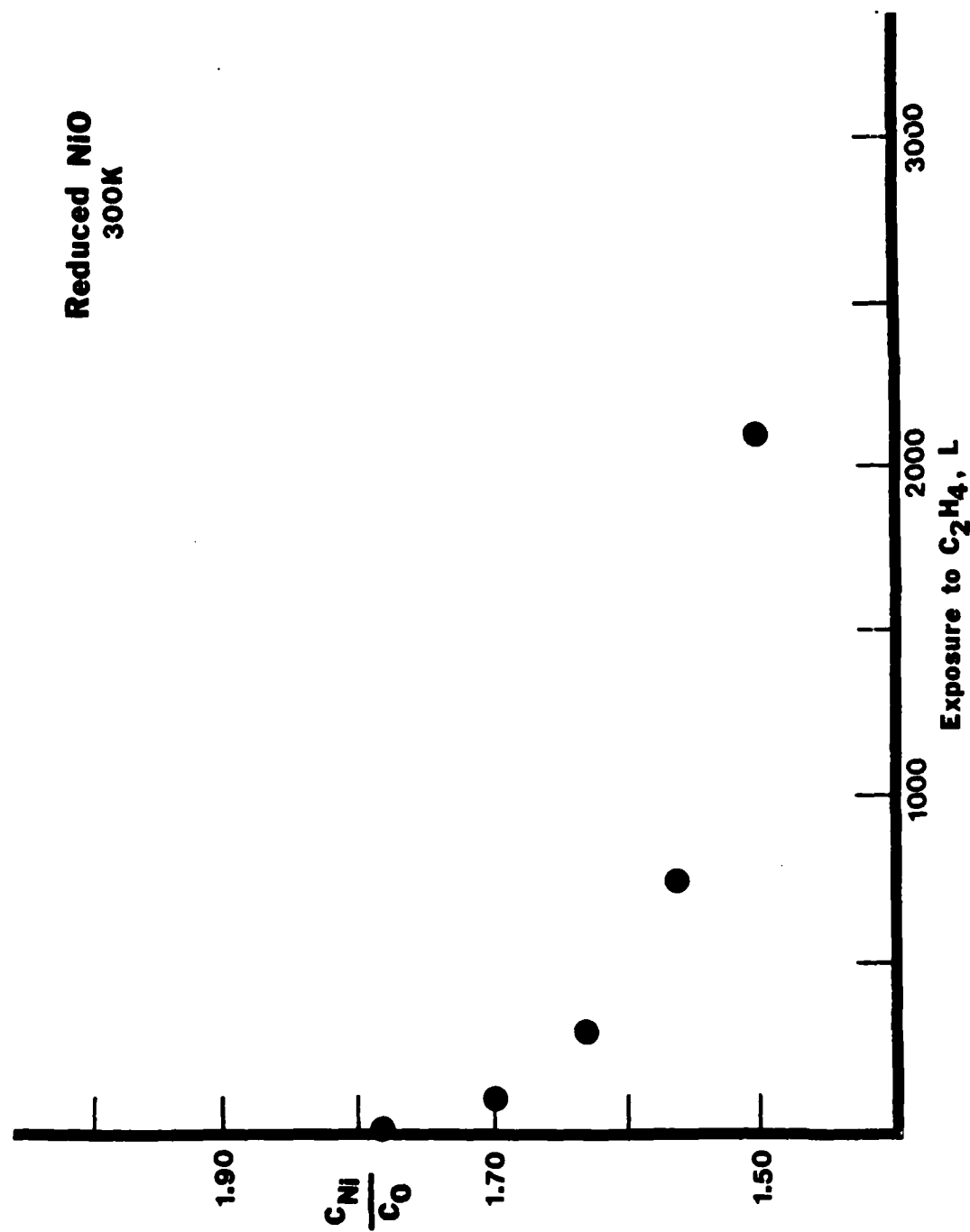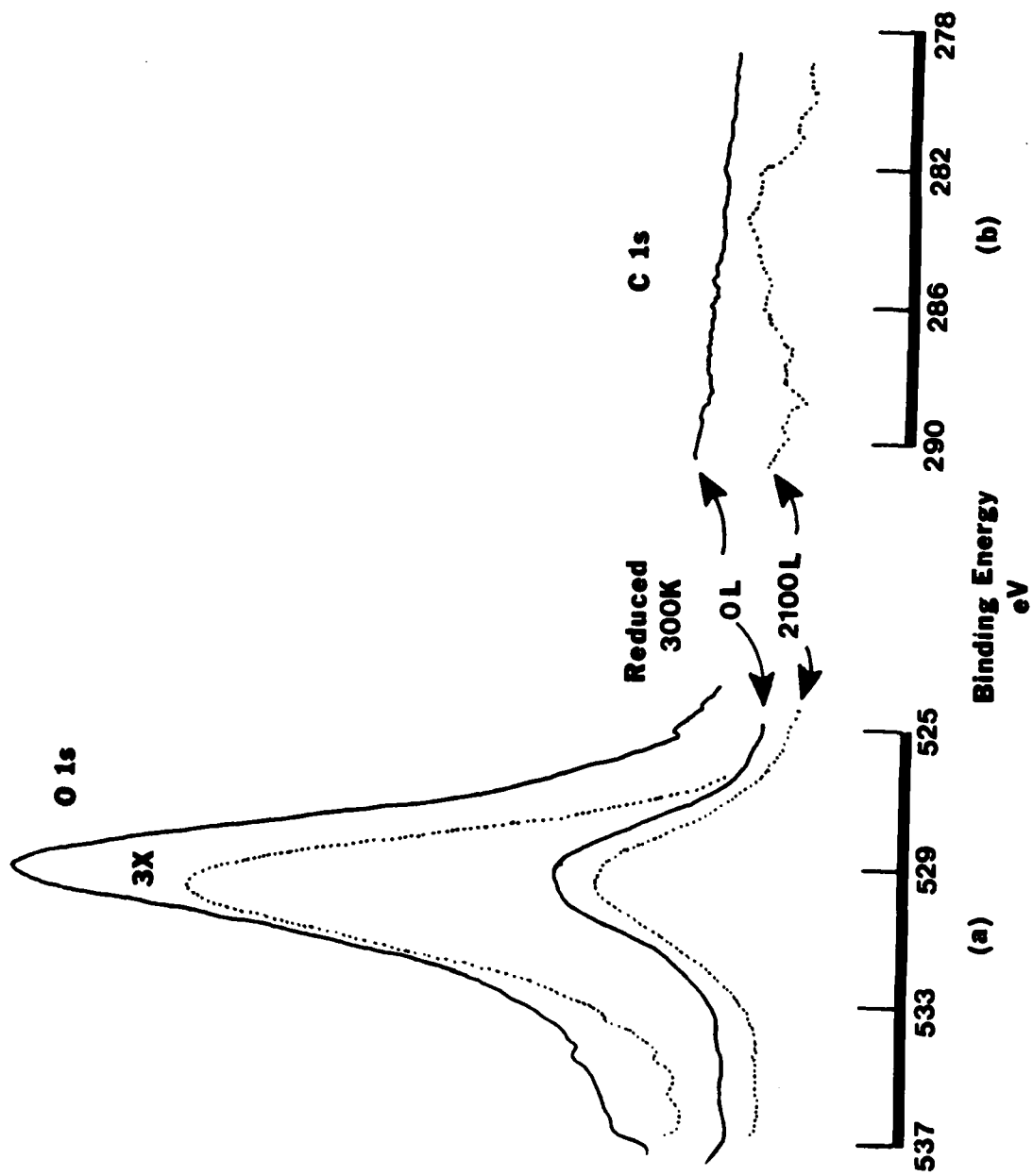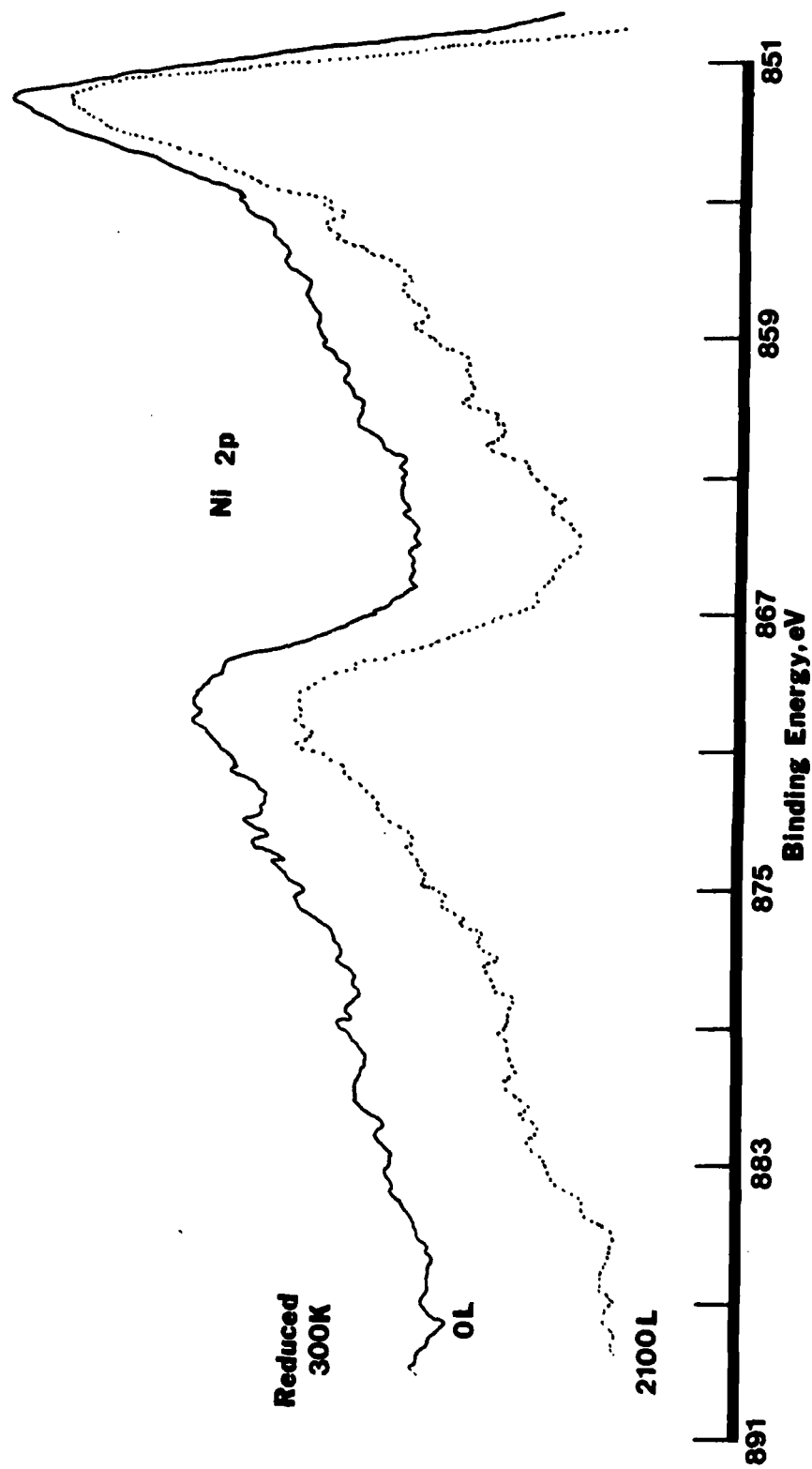at 300K before and after 2100 L ethylene, Al anode
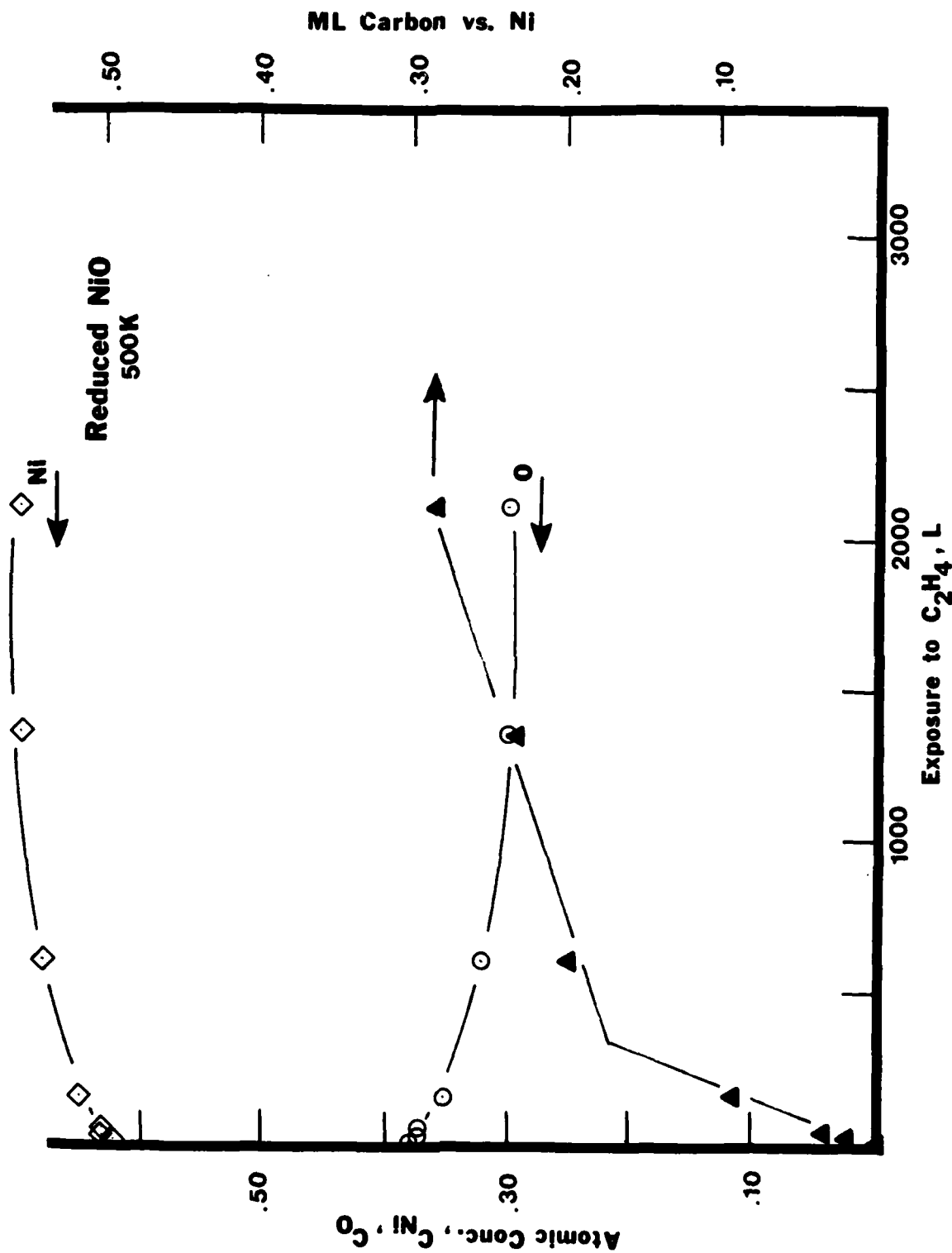
FIGURE 54. Ethylene chemisorption on reduced NiO (100) at 500K
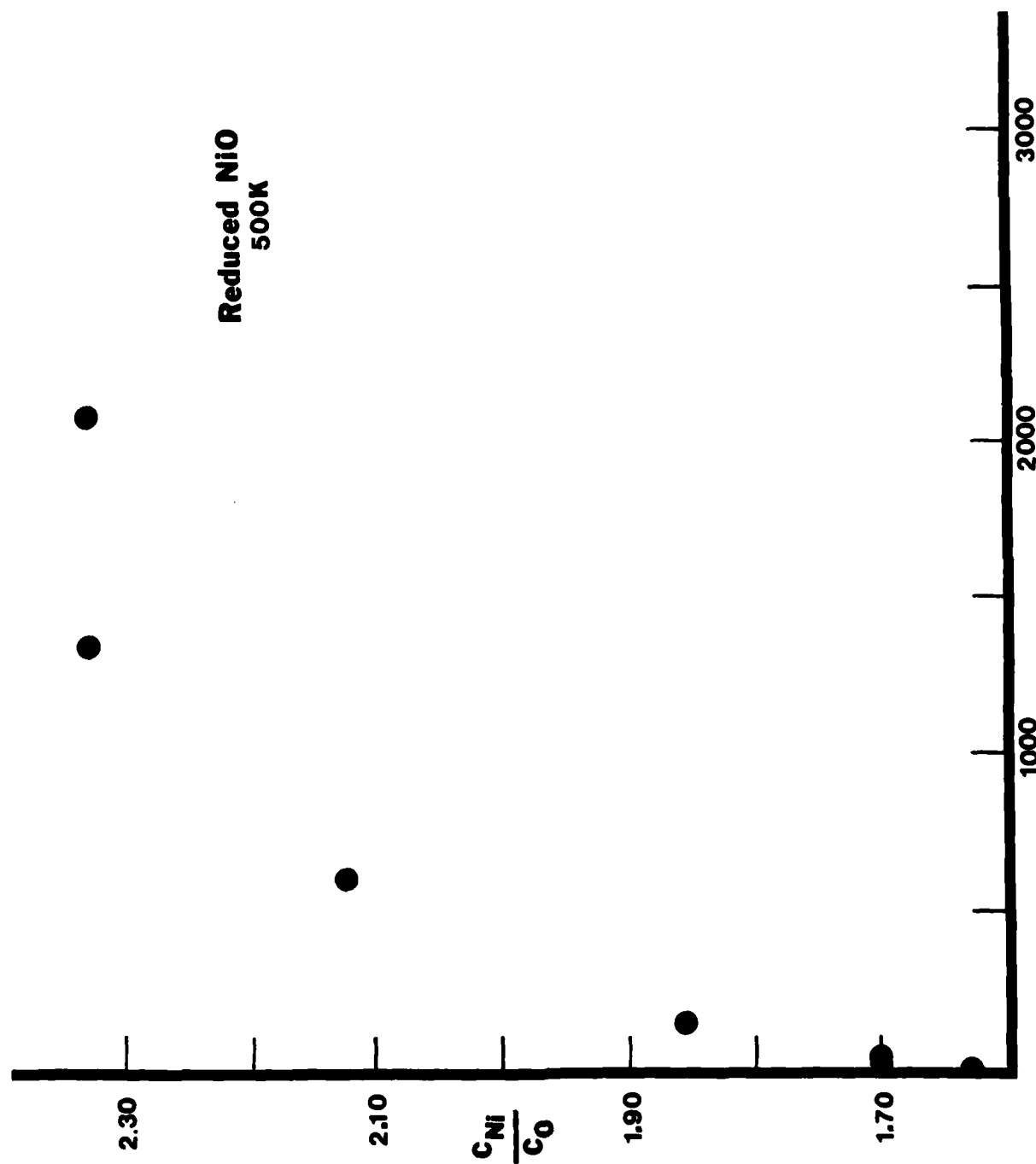
FIGURE 55. C_{Ni}/C_0 as a function of ethylene exposure for reduced NiO (100) at 500K

It was shown earlier in this thesis that reduction of NiO will take place at this temperature in the presence of hydrogen. The further reduction of NiO creates fewer oxygen atoms relative to nickel atoms on the surface which would explain the increase in C_{Ni}/C_O. Since H_2 and CO are both known reducing agents of metal oxides, the following reactions are proposed which could promote the reduction of NiO as a result of the dissociation of ethylene into carbon and hydrogen atoms:

$$2H_{ads} + O_{ads} \longrightarrow H_2O \text{ (gas)}$$
$$C_{ads} + O_{ads} \longrightarrow CO \text{ (gas)}$$
$$C_{ads} + 2O_{ads} \longrightarrow CO_2 \text{ (gas)}$$
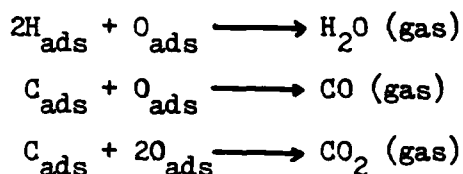
The hydrogen-oxygen reaction seems more likely to occur than the two carbon reactions. This is because the carbon coverage on the surface continues to increase at a fairly high rate throughout exposure. A leveling off and/or eventual decrease in carbon coverage might be expected if the above two carbon reactions were occurring.

The XPS data also yield some interesting results. The intensity of the O 1s peak decreases somewhat with ethylene coverage at 500K, as expected since oxygen is being removed (see Figure 56a). The C 1s peak at 282.6 eV in Figure 56b is much more evident than in previous spectra, though still small and broad, in agreement with the higher carbon coverage. The C 1s maximum is at a lower binding energy than for the reduced sample at 200K or 300K (see Table III).
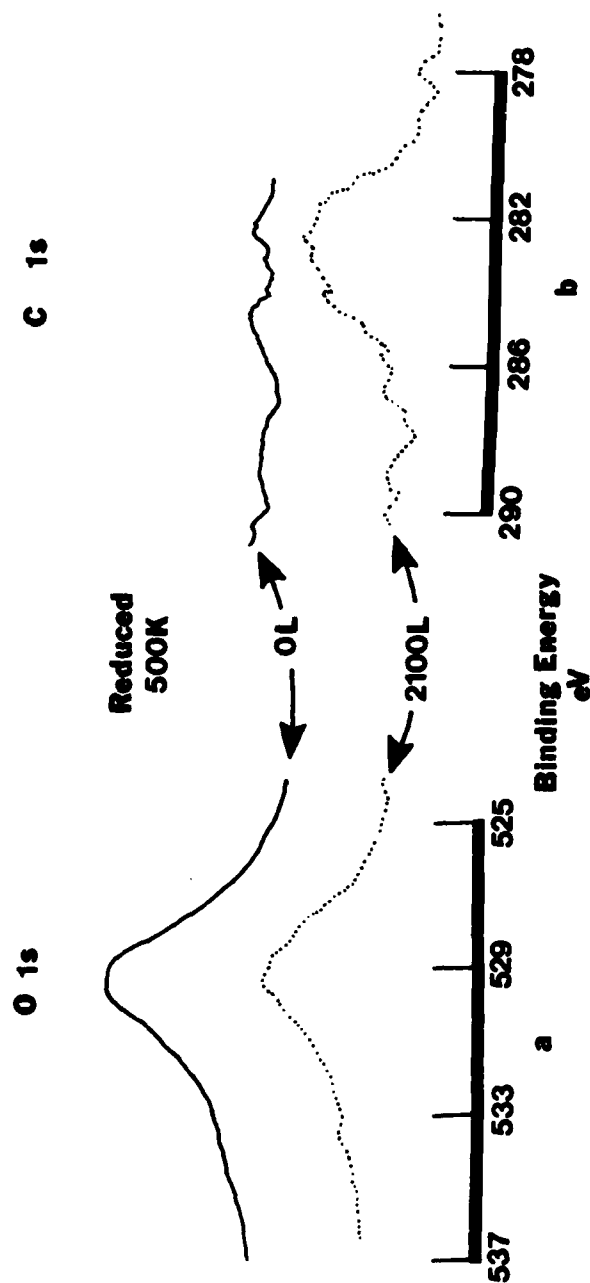
FIGURE 56.   O 1s and C 1s XPS spectral regions for reduced
NiO (100) at 500K before and after 2100 L ethylene,
Al anode

The carbon shift is more likely to occur from Ni-C than from Ni-C$_2$H$_4$. The carbon Auger peak (see Figure 41) is more intense than at the other temperatures, and is even more characteristic of a carbide. The Ni 2p peaks in Figure 57 have shifted to a slightly lower binding energy (see Table III) while the energy difference between the peaks has also decreased. The same behavior was observed when NiO was reduced in H$_2$. Note also the decrease in the intensity of the satellite regions. Thus, the XPS data supports the suggestion that further reduction is taking place at this temperature and the surface is becoming more nickel-like. Although no diffraction pattern changes were visible, the background intensity of the LEED did increase slightly after ethylene exposure to the reduced sample at 500K, indicative of random carbon deposition.

The Auger, XPS, and LEED data show that a different adsorption process is occurring on the reduced sample at 500K than under any of the previous conditions. Since reduction is taking place, the ethylene must be dissociating on the surface; that is, the ethylene is at least losing hydrogen atoms. The mechanism for the dissociation is unclear. If the further reduction is occurring by hydrogen reduction, the following dissociations are proposed:

$$C_2H_4 \text{ (ads)} + * \longrightarrow C_2H_3 \text{ (ads)} + H \text{ (ads)}$$
$$C_2H_3 \text{ (ads)} + * \longrightarrow C_2H_2 \text{ (ads)} + H \text{ (ads)} \quad ,$$
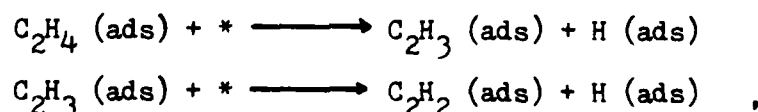
where the astericks (*) are empty adsorption sites. This is analogous to ethylene self-hydrogenation reactions which are observed for ethylene. If the CO reduction is occurring, the adsorbed
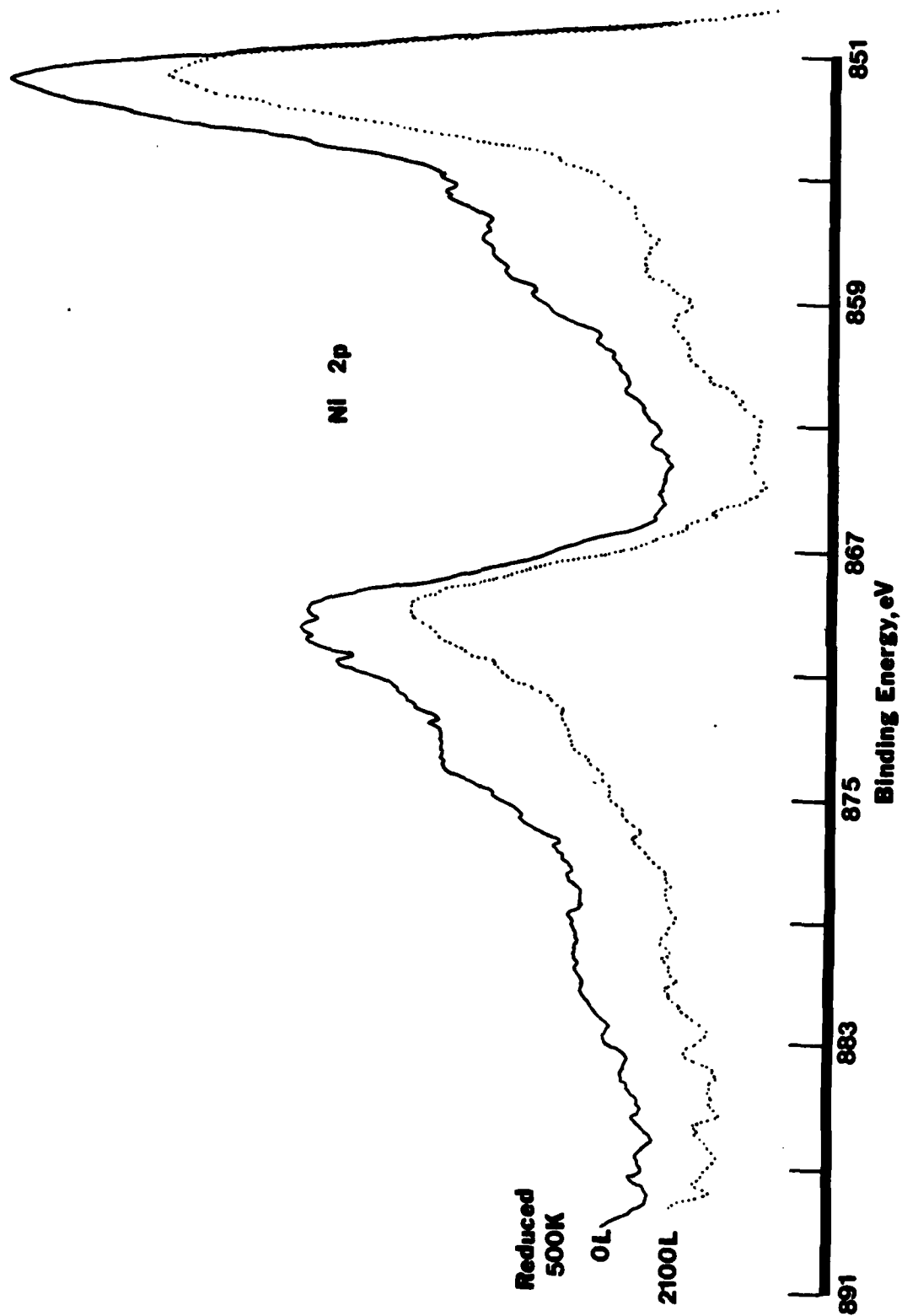
FIGURE 57. Ni 2p XPS spectral region for reduced NiO (100) at 500K before and after 2100 L ethylene, Al anode

hydrocarbon species must dissociate to carbon atoms for the reduction to occur. Because of the ambiguity in the C 1s peaks, no specific carbon species can be identified. However, because of the location of the peak maximum, no carbonates are formed.

Proposed model for ethylene adsorption sites on reduced NiO (100). From the data, the following describes the surface layer of the reduced NiO and the requirements for ethylene adsorption. For all layers of the reduced NiO (100), 50% of the lattice sites are nickel. As shown in Figure 36, there is a constant concentration of oxygen in the first few layers, then an increase in oxygen concentration as more layers are removed. Each layer of reduced NiO contains nickel sites, oxygen sites, and atomically vacant sites due to the loss of oxygen during the reduction process. For each layer, the relative concentrations of nickel, oxygen, and vacancies must equal one. Since the nickel concentration must be 0.50 to agree with the LEED data, the sum of the oxygen sites and vacant sites must equal 0.50. By applying the equation from the THEORY section for layer contributions to the Auger signal with the data of Figure 36 to this model, the top layer of reduced NiO for the adsorption experiment will have C_{Ni} + 0.50, C_O + 0.33, and $C_{vacancies}$ = 0.17 to have the observed Auger Ni/O peak ratio of 0.96.

Assuming that lattice vacancies occur randomly during the reduction process, as must be the case to agree with the LEED, the oxygen sites were randomly populated with oxygen. Since the stoichiometric nickel oxide was shown not to adsorb ethylene at 300K while nickel metal does (39), it was decided to examine the

reduced surface lattice structure for sites that resembled nickel metal. The reduced surface model was studied for possible locations in the oxide top layer (a bare nickel-metal-like site) which would accommodate ethylene molecules. Two adjacent nickel atoms with no oxygen on top of them would provide a potential adsorption site. Upon analyzing the surface, it was discovered that 9% of the surface sites met this criteria. If each of these sites adsorbs one molecule at saturation, the carbon coverage would be 0.09 ML. As observed in Figure 50, the saturation coverage for ethylene is approximately 0.10 ML, which is in good agreement with the data. Other models for potential adsorption sites were studied based on the number of oxygens bonded to nickel sites. In terms of the fraction of nickel sites with a given number of surrounding oxygens (equivalent to monolayers if occupied by carbon), the breakdown is as follows: one oxygen, 0.05; two oxygens, 0.14; three oxygens, 0.32; four oxygens, 0.31; five oxygens, 0.14; six oxygens 0.04. None of these criteria on their own nor reasonable combinations explains the data as well as the previously described model.

The model explains why the LEED pattern remains the same. Although much of the oxygen is gone, nearly all of the nickels still bond to some oxygens, and thus the surface retains the basic NiO lattice. The XPS data indicate, however, that there is definitely an overall change in the electronic structure of the nickel atoms. The large decrease in the intensity of the satellite peaks and the shift toward lower binding energies for the Ni $2p_{3/2}$ peak upon reduction show that the surface Ni atoms are tending

toward nickel metal. This should be expected since the NiO loses many of the oxygen atoms upon reduction. In addition, very few of the nickel atoms have six neighboring oxygens as they did in the stoichiometric form (approximately 4% of the surface Ni's still have six oxygens). However, the adsorption data show that very few of the nickel atoms in the lattice actually acquire the adsorption characteristics of nickel metal. Thus, a combination of the Auger, XPS, and LEED data shows that the reduction process reduces the paramagnetic characteristics of the surface NiO, yet retains the basic lattice structure of NiO with adsorption only possible at isolated nickel sites. The data show that a surface layer consisting of nickel, oxygen, and vacant sites with an increase of oxygen into the bulk can account for the observed adsorption properties of the reduced NiO (100). An important feature of the data is that although the sample is reduced by a good amount (approximately 40%), the surface is relatively inert (as compared to Ni (100) which it is approaching). The gas adsorption character of the surface is not commensurate with the amount of reduction and thus the gas adsorption is very different than for nickel metal.

COMPARISONS WITH OTHER DATA

REDUCTION OF NiO (100)

Very little data could be found in the literature regarding the kinetics of the NiO reduction process (31). However, there is a considerable amount of XPS data available on stoichiometric NiO. In addition, several groups have studied the reduction of NiO using transmission electron spectroscopy, LEED, and reflection high energy electron diffraction (RHEED). These data will be discussed below in relation to the work of this thesis.

Table IV summarizes the XPS data on Ni-O from the literature. The "Comments" column of Table IV describes how the sample was prepared or the physical state of the sample, when available. Note that very little data is available on NiO single crystals. No data were found on the Ni-O (i.e. multiple compounds) from a single crystal NiO sample. The data in Table IV do show that chemical shifts of up to 4.4 eV are apparent in the O 1s region for various Ni-O compounds, with smaller shifts seen in the Ni 2p region.

Kim and Winograd (32) and Kim and Davis (15) conducted extensive studies on nickel-oxygen systems using XPS. Their nickel-oxygen compounds were formed several ways: by oxidation of Ni by exposure to a 400 eV O_2^+ ion beam, by exposure of nickel to O_2 at 100 Torr at various temperatures, by sputtering an oxidized nickel surface with Ar^+ ions, and by heating $Ni(OH)_2$ powder. Kim et.al. were able to assign binding energies to the various nickel-oxygen compounds in the O 1s and Ni $2p_{3/2}$ regions, as shown in Table IV. Although the form

TABLE IV . Compiled XPS Data for the Ni-O System
(Binding Energies in eV)

Compound	Ni $2p_{1/2}$	Ni $2p_{3/2}$	O 1s	Reference	Comments
Ni	869.7	852.3	-----	2	
Ni		852.9	-----	32	
NiO	871.7	853.3		2	
NiO$_{ads}$		853.5	533.5	32	Nickel exposed to oxygen
NiO	872.0	854.0		14	Single crystal
NiO		854.6	529.7	33	Powdered
NiO		854.5	529.9	32	Nickel exposed to oxygen
NiO		854.0	529.1	15	"Stoichiometric"
Ni$_2$O$_3$		855.8	531.7	32	Ni exposed to oxygen
Ni$_2$O$_3$		855.9	530.9	15	
Ni(OH)$_2$		856.6	531.7	32	Powdered

of the NiO used for this thesis work is considerably different from
the NiO prepared by Kim et.al., their data are useful for helping
identify oxygen species which may be pressent on the single crystal.
It is also noted that the Ni $2p_{3/2}$ and O 1s values (854.0, 529.1 eV)
for the "stoichiometric" NiO prepared by Kim and Davis compare
favorably with those obtained in this study (854.5, 529.4 eV),
though shifted by a few tenths of an eV. As with the single crystal
in this thesis work, Kim and Davis only observed a single, symmetric
O 1s peak for their "stoichiometric" NiO.

From Table IV, both Ni_2O_3 and $Ni(OH)_2$ have higher O 1s binding
energies than NiO. One would not expect Ni_2O_3 to be formed upon
reduction. In addition, the Ni_2O_3 is not stable and has only
been observed on the surface of NiO at low temperatures. If $Ni(OH)_2$
were formed, a shift would be visible in the XPS spectra. Such
shifts are not observed, leaving the lattice NiO species the
only ones on the surface.

Little et.al. (34) reduced a single crystal of NiO (100) at $200^\circ C$
for 15 minutes or longer, but at very high H_2 pressures (greater than
one atm). The samples were then brought to room temperature and
studied ex situ using transmission electron spectroscopy for
bulk reduced samples. Depending upon how long the sample was
reduced, they observed different growth patterns for the nickel
nuclei. Early in the reduction process (15 minutes), they observed
discrete nuclei ranging in size from 100 to 2000 Å. Due to the vast
H_2 pressure differential and ex situ examination, however, it is
difficult to relate the results of Little to the data of this

study. Their study focused on bulk reduction, while this thesis work examined surface reduction.

Floquet and Dufour (28), Rickard et.al. (29), and Floquet et.al. (30) performed hydrogen reduction experiments on single crystal NiO (100) at temperatures between 20°C and 350°C under hydrogen pressures of 1×10^{-7} to 1×10^{-5} Torr. These groups, using RHEED, report different packing structures of the nickel nuclei growth at different temperatures. Floquet et.al. state that the Ni nuclei grown under these reduction conditions consist of 30-150 Å crystallites, as observed by high resolution transmission spectroscopy. Floquet and Dufour propose the possibility of both two-dimensional and three-dimensional nucleation. Again, however, these groups emphasized bulk, rather than surface, reduction and studied reduction after the breakdown of the basic NiO lattice had occurred.

No data could be found in the literature which points to an exact mechanism for the reduction of nickel oxide by hydrogen. Information was available, however, on the adsorption of H_2 on nickel surfaces. Lichtman et.al. (42) propose that H_2 strikes a metallic nickel adsorption site, is weakly bound, then dissociates. The dissociated atoms are then more strongly bound to the nickel atoms. May and Germer (21) observed that on a nickel crystal at room temperature, 1.6 to 2.2 monolayers of H_2 were adsorbed at saturation after an incidence of 6.40×10^{16} molecules H_2/cm^2. This converts to a sticking coefficient, S, of 0.05; that is, 5% of the incident molecules were adsorbed. Horgan and Dalins (43) also report low sticking coefficients for smooth nickel surfaces,

$S \leq 10^{-2}$ for Ni (111) and Ni (100). Though low, the sticking coefficient of H_2 on nickel is considerably higher than that computed earlier in this thesis for reduced NiO ($S = 0.0001$). This indicates that the reduced NiO has many fewer adsorption sites for H_2 than does nickel metal, or that, thermodynamically, the NiO surface has a lower equilibrium concentration of hydrogen. Both seem to be true.

THE ADSORPTION OF ETHYLENE ON NiO AND REDUCED NiO

As stated earlier, there have been very few studies on the adsorption properties of nickel oxide. Roberts and Smart (33) conducted a study on the adsorption of CO and NO on powdered NiO samples. In their study, both CO and NO were adsorbed at much higher pressures than were used for ethylene in this study. The NiO samples were exposed to CO and NO at 5 Torr and room temperature for 15-30 minutes. Even under these conditions, very little CO could be detected using XPS. They estimate that the CO adsorption is less than 0.05 ML, which compares favorably with the amount of ethylene the stoichiometric NiO (100) single crystal adsorbed at 200K. They found it difficult to assign any specific binding energy corresponding to the adsorbed CO due to poor resolution. They also report that no reduction of the surface takes place at room temperature with CO at 5 Torr. As shown in this study, ethylene does not reduce the sample at room temperature. Roberts and Smart also report that the CO was easily removed from the surface by heating to 500°C (723K) under UHV.

While no work had been performed on ethylene adsorption on nickel oxide, several investigators have studied ethylene chemisorption on pure nickel using many surface sensitive techniques (35-39). Such data on nickel can be compared to what occurs on the reduced NiO sample to give a measure of how metallic the Ni surface species are on reduced NiO.

Results by Wedler and Brenk (35) and Krasser et.al. (36) indicate that at temperatures less than 200K, ethylene is chemisorbed

molecularly without decomposition. This also is the conclusion that can be drawn from the data on the reduced NiO at 200K. The C_2H_4 does not interact strongly with either surface, with all of the data at 200K supporting this statement.

As the nickel substrate temperature increases to 273-300K, decomposition of the ethylene is observed, with molecular hydrogen, methane, and ethane desorbing, leaving behind acetylenic species on the surface (35,36). At a temperature of 230K, Demuth (40) found that the process of thermally dehydrogenating a monolayer of chemisorbed ethylene to acetylene on Ni (111) was directly observed and was accompanied by the formation of chemisorbed hydrogen on the surface as well as the desorption of some ethylene. For the dehydrogenation process, Demuth and Eastman (37) propose that an exothermic surface reaction is occurring which is thermodynamically unfavorable for a gas phase reaction. It is clear from the data in Figure 50 by the decreasing C_{Ni}/C_0 ratio with a steady C_0 that the reduced NiO is not being further reduced at 300K. The decreasing C_{Ni}/C_0 (with a steady C_0) with increasing carbon coverage indicates that the carbon has a preference to adsorb on the nickel atoms. However, it cannot be deduced from these data that ethylene is being dissociated on the reduced NiO. Although the NiO is reduced considerably, the Ni does not adopt a very metallic character.

At a temperature of 523 K, Zuhr and Hudson (39) report a complete dehydrogenation of the chemisorbed ethylene on Ni (110), with eventual saturation coverage of 0.5 ML of ethylene, or one C per Ni. At even higher temperatures (623K), Wedler and Brenk (35) observe the formation

of a graphite overlayer. Ertl (41), in an extensive LEED study, also reports a graphite layer at 623K. At lower temperatures, the lattice parameter in the LEED was in registry with the nickel upon ethylene adsorption. The data in this study at 500K for reduced NiO, however, gives information which cannot be related to the pure nickel studies. The decreasing C_O relative to C_{Ni} at 500K indicates that the sample is being further reduced. The further reduction also promotes the adsorption of ethylene, which would be expected if the surface is becoming more nickel-like. Again, it is impossible to state whether or not the ethylene is dissociating on the reduced surface at 500K. However, to induce the hydrogen reduction mechanism, the ethylene must at least be losing some of its hydrogens.

Bertolini and Rousseau (44) also studied the adsorption of ethylene on Ni (111) using high resolution electron energy loss spectroscopy, LEED, and thermal desorption spectroscopy. They propose the following reaction:

$$C_2H_4 \text{ (g)} \longrightarrow C_2H_4 \text{ (ads)} + 2H \text{ (ads)}$$
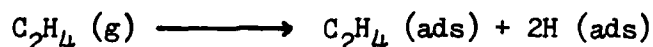
They also propose that the C_2H_2 residue lies flat on the triangular site of three nickel atoms, with a bent H-C-C-H arrangement. The C_2H_2 forms two sigma and one pi bonds to three nickel atoms. From the data of this thesis work and the proposed model for adsorption sites, it is difficult to propose any ethylene arrangement on the reduced NiO surface. There is no direct evidence whether the ethylene bonds with both carbons or with one carbon on the surface.

38. J.E. Demuth, Surface Sci., 84 (1979) 315.

39. R.A. Zuhr and J.B. Hudson, Surface Sci., 66 (1977) 405.

40. J.E. Demuth, Surface Sci., 76 (1978) L603.

41. G. Ertl in: "Molecular Processes on Solid Surfaces,"
    McGraw=Hill, New York (1969).

42. D. Lichtman, F.N. Simon, and T.R. Kirst, Surface Sci., 9
    (1968) 325.

43. A.M. Horgan and I. Dalins, Surface Sci., 41 (1974) 624.

44. J.C. Bertolini and J. Rousseau, Surface Sci., 83 (1979) 531.

45. C.G. Kinniburgh and J.A. Walker, Surface Sci., 63 (1977) 274.

END

FILMED

6-84

DTIC